

May 2017

Investigation of a Novel Turbulence Model and Using Leading-Edge Slots for Improving the Aerodynamic Performance of Airfoils and Wind Turbines

Saman Beyhaghi
University of Wisconsin-Milwaukee

Follow this and additional works at: <https://dc.uwm.edu/etd>



Part of the [Aerospace Engineering Commons](#), and the [Mechanical Engineering Commons](#)

Recommended Citation

Beyhaghi, Saman, "Investigation of a Novel Turbulence Model and Using Leading-Edge Slots for Improving the Aerodynamic Performance of Airfoils and Wind Turbines" (2017). *Theses and Dissertations*. 1447.
<https://dc.uwm.edu/etd/1447>

This Dissertation is brought to you for free and open access by UWM Digital Commons. It has been accepted for inclusion in Theses and Dissertations by an authorized administrator of UWM Digital Commons. For more information, please contact open-access@uwm.edu.

INVESTIGATION OF A NOVEL TURBULENCE MODEL AND USING
LEADING-EDGE SLOTS FOR IMPROVING THE AERODYNAMIC
PERFORMANCE OF AIRFOILS AND WIND TURBINES

by

Saman Beyhaghi

A Dissertation Submitted in
Partial Fulfillment of the
Requirements for the Degree of

Doctor of Philosophy
in Engineering

at

The University of Wisconsin- Milwaukee

May 2017

INVESTIGATION OF A NOVEL TURBULENCE MODEL AND USING LEADING-EDGE SLOTS FOR IMPROVING THE AERODYNAMIC PERFORMANCE OF AIRFOILS AND WIND TURBINES

by

Saman Beyhaghi

The University of Wisconsin- Milwaukee, 2017
Under the Supervision of Professor Ryoichi S. Amano

Because of the problems associated with increase of greenhouse gases, as well as the limited supplies of fossil fuels, the transition to alternate, clean, renewable sources of energy is inevitable. Renewable sources of energy can be used to decrease our need for fossil fuels, thus reducing impact to humans, other species and their habitats. The wind is one of the cleanest forms of energy, and it can be an excellent candidate for producing electrical energy in a more sustainable manner. Vertical- and Horizontal-Axis Wind Turbines (VAWT and HAWT) are two common devices used for harvesting electrical energy from the wind.

Due to the development of a thin boundary layer over the ground surface, the modern commercial wind turbines have to be relatively large to be cost-effective. Because of the high manufacturing and transportation costs of the wind turbine components, it is necessary to evaluate the design and predict the performance of the turbine prior to shipping it to the site, where it is to be installed. Computational Fluid Dynamics (CFD) has proven to be a simple, cheap and yet relatively accurate tool for prediction of wind turbine performance, where the suitability of different designs can be evaluated at a low cost. High accuracy simulation methods such as Large Eddy Simulation (LES) and Detached Eddy Simulation (DES) are developed and

utilized in the past decades. Despite their superior importance in large fluid domains, they fail to make very accurate predictions near the solid surfaces. Therefore, in the present effort, the possibility of improving near-wall predictions of CFD simulations in the near-wall region by using a modified turbulence model is also thoroughly investigated. Algebraic Stress Model (ASM) is employed in conjunction with Detached Eddy Simulation (DES) to improve Reynolds stresses components, and consequently predictions of the near-wall velocities and surface pressure distributions. The proposed model shows a slightly better performance as compared to the baseline DES.

In the second part of this study, the focus is on improving the aerodynamic performance of airfoils and wind turbines in terms of lift and drag coefficients and power generation. One special type of add-on feature for wind turbines and airfoils, i.e., leading-edge slots are investigated through numerical simulation and laboratory experiments. Although similar slots are designed and employed for aircrafts, a special slot with a reversed flow direction is drilled in the leading edge of a sample wind turbine airfoil to study its influence on the aerodynamic performance.

The objective is to vary the five main geometrical parameters of slot and characterize the performance improvement of the new design under different operating conditions. A number of Design of Experiment and optimization studies are conducted to determine the most suitable slot configuration to maximize the lift or lift-over-drag ratio. Results indicate that proper sizing and placement of slot can improve the lift coefficient, while it has negligible negative impact on the drag. Some recommendations for future investigation on slot are proposed at the end. The performance of a horizontal axis wind turbine blade equipped with leading-edge slot is also studied, and it is concluded that slotted blades can generate about 10% more power than solid

blades, for the two operating conditions investigated. The good agreement between the CFD predictions and experimental data confirms the validity of the model and results.

© Copyright by Saman Beyhaghi, 2017
All Rights Reserved

with love,

to my parents, Mina & Abolghasem
and
to my family, Melissa & Rosey

TABLE OF CONTENTS

TABLE OF CONTENTS.....	VII
LIST OF FIGURES.....	IX
LIST OF TABLES	XIV
LIST OF NOMENCLATURE	XV
CHAPTER 1 INTRODUCTION AND BACKGROUND.....	1
1.1 RENEWABLE ENERGY	1
1.2 WIND ENERGY	2
1.3 COMPUTATIONAL VS. EXPERIMENTAL RESEARCH	4
1.4 OVERVIEW OF THE PROBLEMS INVESTIGATED.....	7
CHAPTER 2 THEORY	12
2.1 HAWT AERODYNAMICS.....	12
2.2 WIND TURBINE EFFECTIVE ANGLE OF ATTACK.....	15
CHAPTER 3 ALGEBRAIC STRESS MODEL.....	17
3.1 INTRODUCTION AND LITERATURE REVIEW	17
3.2 THEORY	22
3.3 PROBLEM DESCRIPTION	26
3.4 NUMERICAL SIMULATION	28
3.5 RESULTS AND DISCUSSIONS.....	33
3.6 CONCLUSION	46
CHAPTER 4 HYBRID DES-ASM MODEL	48
4.1 INTRODUCTION	48
4.2 THEORY	48
4.3 COMPUTATIONAL SETUP.....	51
4.4 NUMERICAL PROCEDURE.....	53
4.5 RESULTS AND DISCUSSIONS.....	54
4.6 SUMMARY AND CONCLUSIONS	60
CHAPTER 5 SLOTTED AIRFOIL PARAMETRIC STUDY	63
5.1 INTRODUCTION	63
5.2 THEORY	68
5.3 COMPUTATIONAL SETUP.....	69
5.4 INITIAL VALIDATION	71
5.5 PRELIMINARY RESULTS	77
5.6 RESULTS AND DISCUSSIONS.....	82
5.7 CONCLUSION	92

CHAPTER 6	SLOTTED AIRFOIL MULTI-VARIABLE ANALYSIS	95
6.1	INTRODUCTION	95
6.2	METHODOLOGY	95
6.3	DOE PROBLEM DESCRIPTION.....	100
6.4	RESULTS AND DISCUSSIONS.....	102
6.5	CONCLUSION	110
CHAPTER 7	SLOTTED WIND TURBINE BLADE ANALYSIS	112
7.1	INTRODUCTION	112
7.2	PROBLEM DESCRIPTION	112
7.3	MODEL AND MESH SETUP.....	114
7.4	RESULTS AND DISCUSSIONS.....	116
7.5	CONCLUSION	119
CHAPTER 8	OVERALL CONCLUSIONS AND RECOMMENDATIONS.....	120
REFERENCES.....		124
CURRICULUM VITAE.....		132

LIST OF FIGURES

Figure 1 (a) sketch of an ancient Persian windmill (Sistan; southeast of Iran). Ref.: http://www.mksenergy.com/images/MKS/pic/wi1.jpg , (b) Danish wind turbine by la Cour. Ref.: https://s-media-cache-ak0.pinimg.com/736x/c8/dd/d8/c8ddd8ffb2417252452b59a8cf22aedf.jpg	2
Figure 2 a modern 10MW offshore wind turbine. Ref.: www.Google.com/img hp.....	3
Figure 3 A brief flowchart for typical CFD procedures (Xie, 2012)	7
Figure 4 Force vectors on an airfoil (AvStop, 2015)	13
Figure 5 The efficiency of an optimum rotating wind turbine (Hansen, 2008)	15
Figure 6 Aerodynamics of a HAWT blade: (a) 3D representation of the blade and the velocity vectors near blade, and (b) velocity and force vectors for an infinitesimal spanwise segment of the blade (Burton et al., 2011)	16
Figure 7 Schematic diagram of the domain	27
Figure 8 Computational domain for wind turbine blade study, (a) 3D representation of the gridded volume, (b) side view with the dimensions shown relative to the blade height, L (not to the proper scale)	28
Figure 9 (a) NACA 4412 wind turbine blade with one third of the hub shown, (b) computational domain with the BCs shown	28
Figure 10 Results of the mesh independence study for flat plate problem	31
Figure 11 (a) Grid chosen for the flat plate problem in the entire computational domain; and (b) Grid used in the near blade region at a distance $z=10m$ ($z/L=0.5$) from the hub	32
Figure 12 Distribution of the velocity component along the plate at two different regions along the plate, along with comparison with available data from the literature, (a) laminar region, $Re_x=8e4$, and (b) turbulent region, $Re_x=3.2e6$	35
Figure 13 Distribution of the normalized Reynolds stress components versus the normalized distance from the plate in the near-wall region, for $Re_x=3.2e6$	36
Figure 14 Contours of the axial velocity in the vertical mid plane (units are in m/s)	37
Figure 15 Indices of grid points of interest around the blade at $z/L=0.5$, and $h/L=5e-5$	38
Figure 16 Distribution of the normalized Reynolds stresses around the blade at $z/L=0.5$, and $h/L=5e-6$ (RSM, full implicit ASM, and explicit ASM)	39

Figure 17 Distribution of the normalized Reynolds stresses around the blade at $z/L=0.5$, and $h/L=5e-6$ (Compact $\Phi_{ij,2}$ form)	40
Figure 18 Distribution of normalized Reynolds stresses around the blade at $z/L=0.5$, and $h/L=5e-6$ (No wall effect)	40
Figure 19 Distribution of the normalized Reynolds stress component $\langle uu \rangle$ around the blade at $z/L=0.5$, and $h/L=5e-6$ from RSM, three implicit, and one explicit ASM models	41
Figure 20 Distribution of the normalized Reynolds stresses around the blade at $z/L=0.5$, and $h/L=5e-5$ (explicit; and full $\Phi_{ij,2}$ form with wall effects).....	42
Figure 21 Distribution of the normalized Reynolds stresses around the blade at $z/L=0.5$, and $h/L=2.5e-6$ (explicit; and full $\Phi_{ij,2}$ form with wall effects).....	43
Figure 22 (a) Indices of grid points of interest, and (b) Distribution of the normalized Reynolds stresses, around the blade at $z/L=0.25$, and $h/L=5e-6$ (full $\Phi_{ij,2}$ form)	45
Figure 23 (a) Indices of grid points of interest, and (b) Distribution of the normalized Reynolds stresses, around the blade at $z/L=0.75$, and $h/L=5e-6$ (full $\Phi_{ij,2}$ form)	45
Figure 24 The computational domain and the mesh generated around a NACA 4412 airfoil: (a) geometry, (b) mesh around the airfoil, (c) mesh magnified near the leading edge, (d) mesh magnified near the trailing edge	52
Figure 25 The airfoil considered for this study: (a) the geometry, (b) distribution of y^+ after a converged solution at $AoA=0^\circ$	53
Figure 26 (a) The four near-trailing-edge lines normal to the airfoil surface, located at normalized chord-wise lengths x/c of 0.79, 0.84, 0.89, and 0.95; (b) airfoil surface mid-span where the pressure coefficient data is gathered from.....	55
Figure 27 Distribution of (a) the normalized chord-wise velocity component, and (b) pressure coefficient in the mid-span plane, near the airfoil surface, for $AoA=0^\circ$, and $Re=1.6E+6$	56
Figure 28 Distribution of the pressure coefficient with negative sign at $AoA=0^\circ$ at the mid-span of the airfoil surface, determined from different turbulence models and the published experimental data: (a) the entire curve, (b) near the leading-edge, (c) in the mid-chord, and (d) near the trailing-edge	56
Figure 29 Distribution of (a) the normalized chord-wise velocity component, and (b) pressure coefficient in the mid-span plane, near the airfoil surface, for $AoA=14^\circ$, and $Re=1.6E+6$	57
Figure 30 Distribution of the pressure coefficient with negative sign at $AoA=14^\circ$ at the mid-span of the airfoil surface, determined from different turbulence models and the published experimental data: (a) the entire curve, (b) near the leading-edge, and (c) near the trailing-edge	58

Figure 31 Velocity profiles for $AoA=14^\circ$ case obtained from two different turbulence models and the experimental data, at four normalized chord-wise locations x/c : 0.79, 0.84, 0.89, and 0.95	59
Figure 32 Lift and drag coefficients obtained for the angle of attack of 14 degrees from DES and DES-ASM turbulence models and an experimental set of data from the literature.....	60
Figure 33 The slotted wind turbine blade fabricated and tested at UWM Wind tunnel	67
Figure 34 The computational domain and the mesh generated around a typical slotted airfoil: (a) geometry, (b) mesh around the airfoil, (c) mesh magnified near the leading edge and slot, (d) mesh near the trailing edge	71
Figure 35 (a) a typical picture of a slotted airfoil considered for this study, (b) cross-section of a slotted airfoil with five main geometric parameters shown.....	71
Figure 36 Results of the experimental validation study for flow over a solid airfoil: (a) lift and drag coefficients at various $AoAs$, and (b) pressure coefficient with a negative sign at $AoA=0$.	73
Figure 37 UWM Wind tunnel: (a) overall view, and (b) schematic diagram of different components (Alsultan, 2015)	74
Figure 38 (a) the slotted NACA 4412 airfoil used for the experimental analysis, (b) the support structure made for holding the airfoil in the wind tunnel, (c) schematic diagram of the F/T transducer with the direction of the force and torque components shown, and (d) different physical components of the transducer	75
Figure 39 (a) the new geometry developed in Star-CCM+ for analysis of the flow around a slotted airfoil inside a wind tunnel (the side walls are hidden for higher clarity), (b) cross section of the grid structure on the vertical mid-plane.....	76
Figure 40 Lift and drag coefficients obtained from wind tunnel experiments and CFD simulation with a matching geometry at different $AoAs$	77
Figure 41 Results of a parametric study on (a) lift, and (b) drag coefficient, as a function of slot first-leg length, slot width, and the exit angle.....	78
Figure 42 Performance of slotted airfoils (with $c=1$ m) with different slot widths in terms of (a) lift coefficient, and (b) drag coefficient	80
Figure 43 Performance of slotted airfoils with different first-leg lengths in terms of lift and drag coefficients	81
Figure 44 Velocity vectors near a slotted airfoil with $L_1/c=70\%$, $w/c=2\%$, $\beta_1=0^\circ$, $\beta_2=85^\circ$, and $h/c=4\%$ operating under (a) $AoA=0^\circ$, and (b) $AoA=8^\circ$	82
Figure 45 Lift and drag coefficients of slotted airfoils with different first-leg lengths, $w/c=1\%$, and $\beta_2=25^\circ$ at different $AoAs$	84

Figure 46 Lift and drag coefficients of slotted airfoils with different slot widths, $L_1/c=80\%$, and $\beta_2=25^\circ$ at different AoAs.	84
Figure 47 (a) Pressure contours near the leading edge, (b) normalized velocity contours near the leading edge, and (c) normalized velocity contours near the trailing edge, for a slotted airfoil with $L_1/c=80\%$, $w/c=1\%$, $\beta_1=0^\circ$, $\beta_2=80^\circ$, and $h/c=5.5\%$ at $AoA=0^\circ$	86
Figure 48 Performance of slotted airfoils with different relative exit angles β_2 , with $L_1/c=80\%$, and $w/c=0.5\%$ (a) lift coefficient, and (b) drag coefficient.....	87
Figure 49 (a) Lift and (b) drag coefficients of slotted airfoils with different inlet upward-tilt angles β_1 , with $L_1/c=80\%$, $w/c=0.5\%$, and $\beta_2=25^\circ$ at different AoAs	88
Figure 50 Lift-to-drag ratio versus slot inlet angle β_1 for different angles of attack, for slotted airfoils with $L_1/c=80\%$, $w/c=0.5\%$, $h/c=5.5\%$, and $\beta_2=25^\circ$	88
Figure 51 (a) Lift and drag coefficients, and (b) percentage of lift improvement with respect to the solid airfoil, for slotted airfoils with different inlet vertical positions h , and $L_1/c=80\%$, $w/c=0.5\%$, $\beta_1=2$, and $\beta_2=25^\circ$ at different AoAs	89
Figure 52 Lift-to-drag ratio for slotted airfoils with different inlet vertical positions h , and $L_1/c=80\%$, $w/c=0.5\%$, $\beta_1=2$, and $\beta_2=25^\circ$ at different AoAs	90
Figure 53 Pressure distribution on the top and bottom surfaces of a slot with $L_1/c=10\%$, $w/c=1\%$, $\beta_1=2^\circ$, $\beta_2=25^\circ$ and $h/c=5.5\%$ with $AoA=6^\circ$	91
Figure 54 (a) Lift coefficient, (b) drag coefficient, and (c) lift-to-drag ratio for slotted airfoils with different Reynolds numbers, and $L_1/c=80\%$, $w/c=0.5\%$, $h/c=6\%$, $\beta_1=2$, and $\beta_2=25^\circ$ at different AoAs.	92
Figure 55 Lift coefficient determined experimentally for the solid and the slotted airfoils tested in wind tunnel at three different AoAs.....	92
Figure 56 Schematic diagrams of central composite design for (a) $n=2$ and (b) $n=3$	97
Figure 57 An LHS design with 9 total points	99
Figure 58 Distribution of the data points in the current DoE study for (a) 10 evaluations considered for L_1 & w study, and (b) 12 evaluations considered for β_1 & β_2 study	102
Figure 59 Response surfaces fitted to (a) lift and (b) LoD data points for a DoE study on L_1/c and w/c	104
Figure 60 Response surfaces fitted to (a) lift and (b) LoD data points for a DoE study on β_1 and β_2	105
Figure 61 Response surfaces fitted to (a) lift and (b) LoD data points for a DoE study on L_1/c and h (labeled as InBelowCp in the figure)	106

Figure 62 The objective function LoD monitored in the optimization study with a maximum of 40 evaluations	108
Figure 63 Response surfaces fitted to LoD data points for a DoE study with $Re=1.6E6$ and $AoA=8^\circ$ on (a) L_1/c and w/c , (b) β_1 and β_2 , and (c) L_1/c and h/c	109
Figure 64 Response surfaces fitted to LoD data points for a DoE study with $Re=3.2E6$ and $AoA=6^\circ$ on (a) L_1/c and w/c , (b) β_1 and β_2 , and (c) L_1/c and h/c	110
Figure 65 Computational domain chosen for study of the slotted wind turbine blade: (left) the one-third cylindrical domain, and (right) the CAD model of the slotted HAWT blade.....	114
Figure 66 (a) Schematic diagram of the computational domain and the BCs, (b) near-blade grid structure at a cross-section covering the entire blade span, (c) near-blade grid structure at a cross section located at one-third of the blade height, and (d) near-blade grid structure at a cross-section located at two-third of the blade height	115
Figure 67 Distribution of y^+ on the surface of the blade and the hub	116
Figure 68 pressure distribution at a radial cross-section of the blade at about one half of the blade length after 3.0s of the operation	117
Figure 69 (a) distribution of velocity magnitude at a radial cross-section at about half of the blade height; view from the top of the blade, (b) same as part a, but view from the bottom of the blade, (c) same, showing the entire near-blade region, and (d) velocity contours at a vertical mid-plane of the domain	118

LIST OF TABLES

Table 1 Average differences between ASMs and RSM predictions.....	37
Table 2 Mesh independence study in terms of lift and drag coefficients for an airfoil with incoming air velocity of 12 m/s and AoA=0°	53
Table 3 Mesh independence study in terms of lift and drag coefficients for a slotted airfoil with $L_1/c=45\%$, $w/c=2\%$, $\beta_1=0^\circ$, and $\beta_2=80^\circ$ at AoA=0°	70
Table 4 Lift and drag coefficients for slotted airfoils with different first-leg angles	82
Table 5 An example of a two-level factorial design for a study with three variables	96
Table 6 Ranges of the values taken by five geometrical variables in the DoE study	101
Table 7 Range of the values taken by five geometrical variables in the SHERPA optimization study	108
Table 8 The converged calculated effective AoA and induction factors at three spanwise locations along a rotating blade (R=31 cm)	113
Table 9 Torque and the power generated from both CFD and wind tunnel experiment	119

LIST OF NOMENCLATURE

A	Planform area of the airfoil [m^2]
AoA	Angle of attack [$^\circ$]
\mathbf{a}	Face area vector used in Eq. (4.1) [m^2]
a (a')	Axial (tangential) flow induction factors
a_1	Constant used in Eq. (5.2), (default value: 0.31)
C_D	Drag coefficient
C_{des}	The constant used in Eq. (4.3) for the DES turbulence model
C_i	Coefficients used in EASM, Eqs. (4.11-4.13) ($i=1, 2, 3, 4$)
C_L	Lift coefficient
C_p	Pressure coefficient, defined as $2(P-P_\infty)/\rho U^2$ Also: power coefficient (in chapter 2)
c	Airfoil chord length [m]
D	Drag force [N]
D_{ij}	Summation of molecular and turbulent diffusion terms [m^2/s^3]
D_k	Dissipation term for turbulent kinetic energy [m^2/s^3]
D_ω	Dissipation term for specific dissipation rate [$1/\text{s}^2$]
F_1	Coefficient used in Eq. (5.4)
F_2	Coefficient used in Eq. (5.2)

f_{β^*}	Coefficient Used in Eq. (4.1) for determination of k
f_{β}	Coefficient used in Eq. (4.2) for determination of ω
G_k	Production of turbulent kinetic energy [m^2/s^3]
G_{ω}	Production of specific dissipation rate [$\text{kg}/\text{m}^2\text{-s}^3$]
h	Vertical distance between the slot inlet plane lower lip and a fixed point within the slot [m] Also: distance from the blade surface (Chapter 3) [m]
k	Turbulent kinetic energy [m^2/s^2]
L	Lift force [N] Also: blade length, as used in chapter 3 [m]
L_1	Length of the first leg of the slot [m]
LHS	Latin Hypercube Sampling
LoD	Lift-over-drag ratio
LRR	Launder-Reece-Rodi
l	Dissipation length defined as $k^{1.5}/\varepsilon$ [m]
l_t	Characteristic length of turbulence, used in DES formulation [m]
M	Moment [N.m]
N	Number of wind turbine blades
n	A parameter defined in Eq. (4.12) and used for EASM formulation
P	Pressure [Pa]
P_{ij}	Production of Reynolds stresses from the mean flow [m^2/s^3]

P_k	Production of turbulent kinetic energy [m^2/s^3]
Re	Reynolds number, defined as $U_\infty c/\nu$
RS	Reynolds Stress (chapter 3) Also: Response Surface (chapter 6)
S	Airfoil span length [m]
\tilde{S}_{ij}	Dimensionless strain rate tensor
S_k	Source term in Eq. (4.1) [$\text{kg}/\text{m}^3\text{-s}^3$]
S_ω	Source term in Eq. (4.2) [$\text{kg}/\text{m}^3\text{-s}^2$]
SST	Shear Stress Transport
T	Torque [N.m]
t	Time [s]
U	Velocity vector [m/s]
$\langle u_i u_j \rangle$ or $\overline{u_i u_j}$	A Reynolds stress component [m^2/s^2]
V	Volume [m^3]
\mathbf{v}	Velocity vector used in Eq. (4.1)
\tilde{W}_{ij}	Dimensionless rotation rate tensor
W	Vorticity magnitude [1/s]
w	Slot width [m]
x	Position vector [m]

y^+	Non-dimensional wall distance for a wall bounded flow
z	Local coordinate along the blade starting from the hub, as used in chapter 3 [m]

Greek Letters

α	Angle of attack [°]
β	Coefficient used in Eq. (5.4) Also: local twist angle of a wind turbine blade in chapter 2 [°]
β^*	Constant used in Eq. (5.3), (default value: 0.09)
β_1	Angle between the slot first leg and the horizontal line [°]
β_2	Angle between the first and second legs of the slot [°]
γ	Coefficient used in Eq. (5.4)
γ'	A constant used in Eq. (4.1)
γ_{eff}	Coefficient used in Eq. (4.1)
δ_{ij}	Kronecker delta
δ_{BL}	Boundary-layer thickness [m]
ε	Turbulence dissipation rate [m ² /s ³]
Φ_{ij}	Pressure strain term in Reynolds stress equation [m ² /s ³]
φ	A dimensionless variable in DES formulation used for switching between LES and RANS modes Also: the angle between the vectors of the relative velocity and the blade rotation velocity, as used in chapter 2 [°]
λ_1 - λ_3	Coefficients used in EASM as defined in Eq. (4.11)

μ	Dynamic viscosity [Pa.s]
ν	Kinematic viscosity [m ² /s]
ρ	Density [kg/m ³]
σ_k	Coefficient used in Eq. (5.3)
σ_r	blade solidity
σ_ω	Coefficient used in Eq. (5.4)
$\sigma_{\omega 2}$	Constant used in Eq. (5.4), (default value: 0.856)
τ	Shear stress [Pa]
ω	Specific dissipation rate [1/s] Also: angular velocity, a.k.a. Ω [rad/s]
<i>subscripts</i>	
0	Ambient values (as in k_0 and ω_0)
g	Grid
i,j,k	Tensor index notations
∞	Free-stream

ACKNOWLEDGMENTS

First, I would like to express my gratitude towards my advisor, Professor Ryoichi Amano for his continuous support, guidance, patience and advices throughout this journey. He has set an example of excellence as a researcher, mentor and instructor. Moreover, he has always encouraged me to actively participate in academic and professional events such as exhibitions and conferences to advance my scholarly research. I would like to sincerely thank my doctoral committee members, Prof. John Reisel, Prof. Adel Nasiri, Prof. Michael Nosonovsky, and Prof. Istvan Lauko, for the fruitful conversations and their amazing insights that helped significantly with the quality of my research.

I am very grateful to the Department of Mechanical Engineering at the University of Wisconsin-Milwaukee (UWM) for the financial support during my PhD studies. Moreover, I am thankful to UWM graduate school for awarding me with the Distinguished Dissertation Fellowship award for the academic year of 2015-2016.

Many thanks to all my friends, and former and current colleagues at UWM, including Bamdad Barari, Ping Dong, Tarek Elgammal, Mehdi Gilaki, Randy Jackson, Nazanin Maani, Mandana Saravani, Mohammad Reza Shaeri, and Yi-Hsin Yen. It has been a pleasure to work with all of them. I would also like to acknowledge my long-time friend and mentor, Dr. Miad Yazdani, for all his invaluable comments and brilliant suggestions for my research.

Finally, I have to thank my amazing family, including my parents Mina and Abolghasem, my wife Melissa, my sister Negin and her family (Saman, Bardya, Meloryn, and Lily), and all my in-laws (especially my mother-in-law, Patricia) for their endless love, support and encouragement throughout this journey.

Chapter 1 Introduction and Background

1.1 Renewable Energy

Because of the problems associated with an increase of greenhouse gases, as well as the limited supplies of fossil fuels, the transition to alternate, clean, renewable sources of energy seems inevitable. Renewable sources of energy can be used to decrease our need for fossil fuels, thus reducing impact to humans, other species and their habitats. The government of United Kingdom has set a target to produce 15% of the UK's energy from renewable energy sources by 2020 and cut the country's carbon emissions by 34% by 2020 (Uswitch, 2015). The United States government also has a national renewable energy target of 20% by 2020 (Wikipedia, 2017). The most common forms of renewable energy are wind, solar, hydroelectric, and geothermal, although utilization of biomass, e.g., chicken manure (Hussein et al., 2017), and tidal wave (Börner and Alam, 2015) for energy production has been investigated as well.

Solar energy development has been primarily limited to countries with suitable space, climate and financial resources such as Mediterranean countries, India, Spain and the United States. There are two common methods for electricity generation from the sun. One is through using solar panels equipped with photovoltaic (PV) cells, and the other is by employing solar thermal power plants. In the former approach, PV cells are used to convert directly sunlight to electricity. In the latter form, a large number of mirrors or lenses are utilized to concentrate a large area of sunlight, onto a small area. Electricity is generated when the concentrated rays of light are converted to heat, which can subsequently drive a steam turbine, connected to an electrical power generator or initiate a thermo-chemical reaction.

Overall, wind energy can be a great candidate for producing electrical energy in a more sustainable and renewable manner. Unlike the systems operating with fossil fuels, or even some

of the other forms of renewable energy, there is no need for extensive sources of water for system heat rejection when wind energy is utilized for power generation.

1.2 Wind Energy

Wind turbines are the oldest devices to capture wind energy on land. Traditionally, they have been used in irrigation systems, as well as in wind mills. One of the first wind mills built was in the province of *Sistan* (Persia) between the 7th and the 9th century A.D., where vertical axis wind turbines were used (Hanson, 2008); see Figure 1a. The use of windmills successively grew in Middle East, Asia, and Europe for grinding corn and other grains, and for water pumping systems. The first horizontal axis wind turbines were made in Europe in the 12th century (Schito, 2011). Wind turbines proved to be real alternatives for watermills that were on the rivers, and were typically properties of nobility.



(a)



(b)

Figure 1 (a) sketch of an ancient Persian windmill (Sistan; southeast of Iran). Ref.: <http://www.mksenergy.com/images/MKS/pic/wi1.jpg>, (b) Danish wind turbine by la Cour. Ref.: <https://s-media-cache-ak0.pinimg.com/736x/c8/dd/d8/c8ddd8ffb2417252452b59a8cf22aedf.jpg>

Using wind turbines to generate electricity was first realized in late 19th century. The first modern wind turbine was constructed in Scotland in 1887 by Prof. James Blyth and was used to provide the electrical illumination to his cottage. One year later, Charles F. Brush (Cleveland, OH) implemented a wind turbine with an approximate rotor diameter of 17m and with 144

blades producing 12kW (Leung and Yang, 2012). Around the same time, Poul la Cour (Denmark) built one of the first electricity generating wind turbine prototypes in Europe (Figure 1b). For much of the 20th century, there were only a few attempts on construction and use of wind turbines for power generation. Some of the notable developments were the 1250 kW Smith-Putnam turbine (USA, 1941), the 100 kW, 30m diameter Balaclava wind turbine (then USSR, 1931), and the Andrea Enfield 100 kW, 24m diameter pneumatic turbine designed in the early 1950s in the UK (Burton et al., 2011). A good summary of the history of the early wind turbine development is provided in the literature (Shepherd, 1994; Divone, 1994).

Small size wind turbines were widely produced for fuel saving and farm application until 1973, when the price of oil rose dramatically, and drew world's attention to pursuing alternative energy sources. The sudden increase of oil price gave rise to development of several government-funded research and development programs around the world, one of each led to design and construction of a 38m diameter 100 kW prototype in 1975 and a 97.5 m diameter 2.5 MW one in 1987. An interested reader is referred to the Wind Energy handbook (Burton et al., 2011), where a summary of the wind turbine development history in the last two decades of the 20th century is provided (Figure 2).



Figure 2 a modern 10MW offshore wind turbine. Ref.: www.Google.com/imghp

In early 21st century, the issues such as carbon footprint, climate change, shrinkage of fossil fuel resources, and finally energy market security have drawn attentions to renewable energies more than ever. The wind energy has been growing with an average rate of around 30% per year since 2003, and the offshore wind turbines and wind farms are being designed and deployed extensively as well (Nelson, 2000). It was announced by the European Union in 2007 that 20% of all energy should be from renewable sources by 2020. Due the difficulty of using renewable energy for transport and heat, this means that around 30-40% of the electrical energy should be provided by the renewable sources such as wind energy, as one of the cleanest forms of energy. The Fukushima nuclear power plant disaster in 2011 was another motivation for using wind energy. The research towards reduction of fossil-fuel energy and greenhouse gases continues to grow, and there are many countries with the objective of reducing carbon footprint by as much as 80% by 2050 (Burton et al., 2011).

1.3 Computational vs. Experimental Research

Because of the fluid mechanics principles, as large bodies of air flow over any terrain, a thin boundary layer is formed in the vicinity of the ground surface that leads to a significant drop of the air velocity. It is only outside this near-ground boundary layer, where the air speed is large enough to be suitable for power generation. Therefore, commercial wind turbines should operate at very high elevations, so that they are exposed to higher air speeds, and can generate more power. Modern commercial wind turbine blades are as large as 80 m in length. Because of the high manufacturing and transportation costs of the wind turbine components, it is necessary to evaluate the design and predict the performance of the turbine prior to shipping it to the site, where it is to be installed.

One of the common approaches for initial testing of wind turbines is to fabricate a small prototype of the blade, and conduct a set of experiments in a closed- or open-loop wind tunnel. The performance of wind turbines with different design features can be monitored and analyzed while running under different operating conditions, such as the angle of attack (from now on shown as AoA), incoming air speed, etc. The test section size of academic-level and industrial-level wind tunnels can be as small as few centimeters, or as large as 10's of meters. Many researchers are currently conducting wind tunnel experiments, including but not limited to National Aeronautics and Space Administration (NASA) (Broeren et al., 2011; etc.), Boeing (Lynch and Khodadoust, 2001; etc.) as well as several research centers and universities around the globe, such as Iowa State University (Hu and Zhang, 2008; Liu et al., 2015; etc.), Saint Anthony Falls Laboratory at the University of Minnesota (Chamorro et al., 2014; etc.), Delft University, etc. Despite all the benefits of wind tunnel studies, there are some limitations associated with any experimental study mimicking the real behavior of commercial wind turbines. First, evaluation of various design features could be very time consuming. If one is to study the impact of the geometrical parameters such as blade aspect ratio, trailing edge tubercle size, winglet angle, etc. on overall power generation, they would need to manufacture blades with so many different configurations, and test them individually. It may be very costly to cover the influence of a wide range of involving parameters for the purpose of finding the most optimum design.

The second drawback is regarding the presence of solid walls. A wind tunnel is generally an enclosure, where the walls and ceiling impact the flow physics around the blade. Therefore, this cannot be a perfect representation of the *external* flow condition observed for commercial wind

turbine applications. Moreover, it is typically hard to control the level of turbulence intensity of the incoming air flow.

Computer simulations, on the other hand, do not suffer from the aforementioned limitations, and therefore can be considered as good tools for performing any optimization or parametric study, where certain parameters are adjusted, and the impact on response variables is evaluated. One will have full control on the imposed incoming flow conditions, as well as the boundary conditions in all the surfaces. Note that the reliability of any numerical simulation is always contingent upon a successful experimental validation. That means for at least one baseline case, one needs to compare the results of the numerical simulation with those obtained from an accurate experiment conducted at a similar operating condition. If the agreement between the two sets of data is acceptable, then one can proceed with numerical simulation.

Computational Fluid Dynamics (CFD) is the primary framework of the present study. Two problems are investigated here, one is regarding the suitability of a novel turbulence model to be used for analysis of flow around wind turbines, and the other one is examination of a novel add-on design feature, i.e., leading-edge slot, for performance improvement of airfoils used in horizontal-axis wind turbine (HAWT) blades, as well as other applications. A typical CFD procedure for modeling and analysis of a thermo-fluid system is demonstrated in Figure 3. The same steps are followed in the present study.

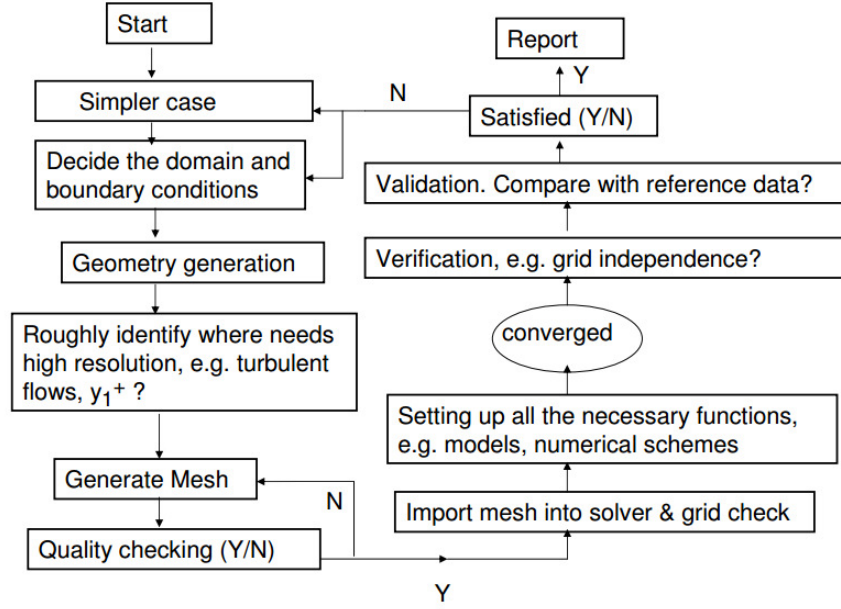


Figure 3 A brief flowchart for typical CFD procedures (Xie, 2012)

1.4 Overview of the Problems Investigated

1.4.1 CFD Using a Hybrid LES-RANS Technique

In order to conduct a CFD study for a turbulent flow system, we have to choose a proper turbulence model. Several turbulence models are proposed and available in the literature, which are different in terms of accuracy and computational demands. Here, suitability of a particular turbulence model is studied for a solid wind turbine blade and a limited-span airfoil.

The most accurate and computationally intensive method for turbulence treatment is Direct Numerical Simulation (DNS). In this approach, the Navier–Stokes equations are numerically solved without any additional turbulence model used. This means that the entire range of spatial and temporal scales of the turbulence must be resolved. All the spatial scales of the turbulence must be resolved in the computational domain, from the smallest dissipative scales, up to the integral scale (Pope, 2000). As an estimate, the number of operations required to complete the simulation is proportional to the number of mesh elements and the number of time steps, and it

has been shown that the number of operations grows as Re^3 . Therefore, the computational cost of DNS is very high, even at relatively low Reynolds (Re) numbers.

For the Reynolds numbers encountered in most industrial applications, the computational resources required by a DNS would exceed the capacity of the powerful computers currently available. However, direct numerical simulation is a useful tool in fundamental research in turbulence. Using DNS, it is possible to perform numerical experiments, and extract from them information difficult or impossible to obtain in the laboratory, allowing a better understanding of the physics of turbulence.

On the other end of the spectrum of the turbulence models are Reynolds-averaged Navier–Stokes (RANS) equations. The idea behind the equations is Reynolds decomposition, where an instantaneous quantity is decomposed into its time-averaged and fluctuating quantities (Pope, 2000). This idea was first proposed by Osborne Reynolds (Reynolds, 1985). In RANS equations, the turbulent flow is modeled using certain closure formula, instead of directly resolving them. Different RANS models exist and they use different techniques to calculate Reynolds stress (RS) components. One general drawback of RANS models is that they are typically very case dependent, which means the parameters of the models must be optimized and validated for specific configurations of turbulent flows, and should be used with caution in general-purpose applications. Another very important concern is that in turbulent flows, the behavior of larger eddies is significantly different than smaller eddies. But RANS models cannot distinguish between the size differences of eddies, and that can result in inaccuracies in flow predictions.

Understanding the limitations of both DNS and RANS models, researchers have proposed a somewhat middle-ground simulation technique, known as Large Eddy Simulation (LES). It was first proposed in 1963 (Smagorinsky, 1963) for simulation of atmospheric air currents. Since

then, LES has grown rapidly and it is currently used for a wide variety of engineering applications, including combustion (Pitsch, 2006), acoustics (Wagner et al., 2007), Wind energy (Sarlak Chivae, 2014), etc. LES operates based on the low-pass filtering principle and it is applied on the Navier–Stokes equations to reduce the range of length scales of the solution, and hence, reducing the computational cost. LES resolves large scales of the flow field solution allowing better fidelity than RANS, whereas it uses models to resolve smallest scales of turbulence. This makes LES an appealing method for practical engineering applications and those with complex geometry or flow configurations.

Despite its benefits, the predictions of LES in the near-solid-wall region (where the smallest eddies are present) can be only as good as the closure model employed in this region. Reynolds Stress Model (RSM) is one of the complex RANS-based approaches, in which the Reynolds stresses are obtained by solving partial differential equations, as opposed to other models that are based on Boussinesq approximation (Pope, 2000).

RSM, however, is more time-consuming than other RANS-based models, and therefore it is desired to find an alternate turbulence model to be used in conjunction with LES. A modified version of RSM, known as Algebraic Stress Model (ASM), is defined in order to be used in a hybrid LES-RANS formulation. Different variants of Implicit ASM (IASM) as well as explicit ASM (EASM) are considered. The ASM formulation is first demonstrated for a simple two-dimensional problem of flow over a flat plate (Amano and Beyhaghi, 2015), then some of the appropriate ASM schemes will be used for a problem of turbulent flow over a HAWT blade (Beyhaghi and Amano, 2015). After the framework is successfully developed and tested, this model is used in conjunction with DES (which is a well-known hybrid LES-RANS scheme), and

the resultant model is used for the analysis of flow around a limited-span airfoil at two distinct angles of attack.

1.4.2 Improving Aerodynamic Performance using Slots

Although HAWTs have proven to be very useful for generating electrical energy, they suffer from some limitations, such as the Betz limit, which confines the efficiency of turbines to around 59% (Burton et al., 2011). A great deal of research has been aimed at finding ways to increase the power generation from turbines. One common approach is to optimize the geometric shape of the airfoil used at each spanwise location. The focus has mainly been on adjusting airfoil type, shape, size, and twist angle. Both computational and experimental techniques have been extensively used for this purpose. Researchers have also considered using add-on features on the blades, to change the flow pattern around the blade, possibly decrease drag and increase lift, and ultimately increase the overall power generation. Some of the more common features are winglet at the tip of the blades (Johansen and Sorensen, 2006), small riblets in the form of sawtooth, etc. (Martin and Bhushan, 2014; Bixler and Bhushan, 2013), vortex generators (VGs) (Trolborg et al., 2015; Gao et al., 2015; Mueller-Vahl et al., 2012; Velte, 2009; Lin, 2002), etc. All of the methods above have shown to be contributing to some percentage of increase in power generation, and they can all be studied separately. Some of the important issues to consider are manufacturability, durability, ease of installation, and side effects, such as drag penalty and additional fatigue loads.

In the present work, the performance of a cambered airfoil equipped with leading-edge slots is investigated thoroughly. Different types of slots have been used on aircraft wings. Based on the recent encouraging results (Alsultan, 2015), the idea of using a modified form of spanwise slots for airfoils is investigated in more details. Such slots are drilled near the leading edge of the airfoil, in order to re-route some of the air flow passing from the bottom portion of the airfoil,

and generate higher upward force, known as lift. After an initial validation, a set of parametric studies on multiple design variables of slots is conducted, where the lift coefficient or lift-over-drag ratio is maximized. Slots are then drilled inside wind turbine blades, and simulations are conducted to study their effectiveness.

1.4.3 Summary of Objectives

Based on what described in the previous sub-sections, the two main objectives of this dissertation can be summarized as follows:

- (1) The first objective (chapters 3 and 4) is to investigate whether combination of DES (which is a readily-hybrid LES-RANS simulation method) with a modified version of RSM (known as ASM) could improve the detailed flow predictions in the vicinity of the solid surfaces of a streamlined body. Note that RSM is the most comprehensive RANS-based turbulence model, and ASM is a modified version of RSM that is customized for the near-wall region, and is not as computationally expensive.
- (2) The second objective (chapters 5, 6, and 7) is to study the feasibility of improving the aerodynamic performance (lift and lift-over-drag ratio) of a common cambered airfoil and power generation of a three-blade HAWT by designing and deploying a novel add-on device, known as leading-edge slots. The effectiveness of such slots and the extent of their offering improvement is to be characterized at different operating conditions, e.g., at several angles of attack (covering the entire range of operation), and few different Reynolds numbers. To do so, five main geometrical design parameters are identified and investigated in single-variable and multi-variable fashions.

Chapter 2 Theory

2.1 HAWT Aerodynamics

Wind turbines can be categorized as horizontal axis (HAWT) and vertical axis (VAWT). While each design has its advantages and disadvantages, the attention is limited to HAWTs in the present study. The main rotor shaft and electrical generator of HAWTs are located at the top of a tower, and must be pointed into the wind. Large commercial turbines use a wind sensor coupled with a servo motor. Most of them have a gearbox that can increase the rotation speed and, therefore, make it more suitable to drive an electrical generator.

As far as the operation is concerned, wind turbine blades are very similar to aircraft wings, as they both operate based on the same aerodynamic principles, and both have similar profile shapes, known as *airfoils*. As the air flow approaches the airfoil, it is separated into two main streams, one flowing from the bottom (known as the *pressure side*), and one flowing over the top surface of the airfoil (known as the *suction side*). The latter stream experiences an increase in main velocity due to the Bernoulli's principle, which in turn results in pressure reduction. Because of the pressure differential between the suction and pressure sides, there will be a net “upward” force exerted on the airfoil from the bottom. This force is referred to as *Lift*. Another significant force is generated as a result of the resistance of the airfoil against the air flow. This force is called *Drag*, and is more important in aircraft (due to its direct impact on fuel consumption) and less significant for wind turbine applications. Lift and drag are dependent on several parameters, such as the incoming airflow velocity, air properties, and, of course, AoA. A schematic diagram of an airfoil with lift and drag forces is shown in Figure 4. These forces are briefly described in the next sub-section.

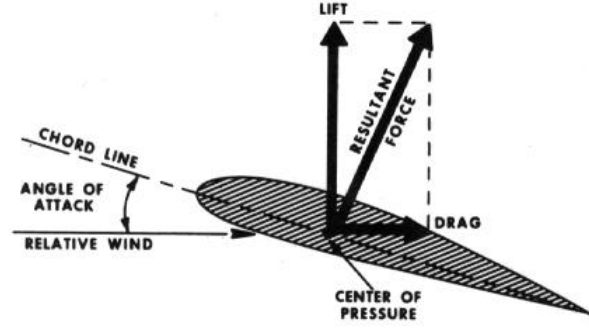


Figure 4 Force vectors on an airfoil (AvStop, 2015)

2.1.1 Coefficients of Lift, Drag, and Moment

Drag and lift are the main forces exerted on rotating wind turbine blades, whereas the pitching moment is normally present as well. Lift is the force used to overcome gravity on aircraft wings (Hansen, 2008) and is defined to be perpendicular to the direction of the oncoming airflow. It is formed as a result of the unequal pressure on the upper and lower airfoil surfaces. The drag force is defined as a force parallel to the direction of oncoming airflow. The drag force is due both to viscous friction forces at the surface of the airfoil, and to the unequal pressure on the airfoil surfaces facing toward and away from the oncoming flow. For an airfoil, Hansen (2008) stated that the lift to drag ratio should be maximized, in order to improve the efficiency when wind turbine generates electricity. Dimensionless lift and drag coefficients are defined as follows:

$$C_L = \frac{L}{1/2 \rho u_\infty^2 A} \quad (2.1)$$

$$C_D = \frac{D}{1/2 \rho u_\infty^2 A} \quad (2.2)$$

where ρ is the air density and A is the planform area of the airfoil. Unit for the lift (L) and drag (D) in equations above is force (in N). It is also necessary to know the pitching moment M . The pitching moment on an airfoil is the moment produced by the aerodynamic force on the airfoil if

that aerodynamic force is applied at the aerodynamic center of the airfoil. The pitching moment coefficient is defined as

$$C_M = \frac{M}{\frac{1}{2} \rho u_\infty^2 c^2} \quad (2.3)$$

2.1.2 Tip Speed Ratio

The tip speed ratio (TSR) is the ratio of the blade tip speed over the wind speed. It is a significant parameter for wind turbine design and is defined as

$$\lambda = \frac{\omega R}{u_\infty} \quad (2.4)$$

where ω is the angular velocity of the wind turbine rotor, R is the radius of the rotor (or: blade length) and u_∞ is the main component of the incoming wind velocity. A higher TSR indicates a higher efficiency but is also related to higher noise levels. Usually a low-speed wind turbine chooses value of TSR from 1 to 4 and a high-speed wind turbine chooses its value from 5 to 9. As a preliminary design consideration, the best range of tip speed ratios for a high speed turbine is around 6~7 (Burton et al., 2011), which ensures that the wind turbine can run at near maximum power coefficient.

2.1.3 Betz Limit

The wind turbine efficiency is defined as the ratio of coefficient of performance C_p and the Betz limit, which is shown to be 16/27 or around 0.593. This value was concluded by the German physicist, Albert Betz in 1919 (Burton et al., 2011). This value is the maximum power efficiency of a wind turbine that converts the kinetic energy to mechanical energy (Figure 5).

Note that C_p is defined as follows:

$$C_p = \frac{P}{\frac{1}{2} \rho A u_\infty^3} \quad (2.5)$$

where A here is the capture area of the rotor, and found as πR^2 .

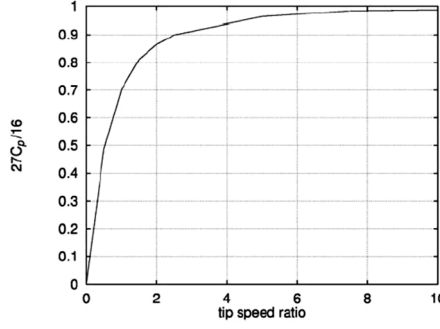


Figure 5 The efficiency of an optimum rotating wind turbine (Hansen, 2008)

2.2 Wind Turbine Effective Angle of Attack

The effective angle of attack with which air streams approach the airfoil profile at any span-wise cross section of a wind turbine blade is determined based on several parameters, including the incoming wind velocity, the rotation rate of the blade, and the twist angle. Figure 6 shows a three-blade HAWT, for which the velocity and force vectors are shown for a small radial segment of the blade. In part b of the figure, r is the radial distance of the blade segment from the centerline of the hub, a and a' are the axial- and tangential-flow induction factors, α is the angle of attack, ϕ is the angle between the vectors of the relative velocity W and the blade rotation velocity, and finally, ω is the blade angular velocity. The effective AoA can be determined after subtracting the local twist angle β from ϕ . Typically, the twist angle distribution along the blade span is such that under the normal (design) operating condition, the effective AoA is more or less constant throughout the blade. Since the values of a and a' are not known *a priori*, determination of the AoA involves an iterative procedure, which is outlined here:

- Start with initial guesses for a and a' (typically both can be set to zero)
- Calculate the relative velocity W , ϕ , and finally AoA from the three equations below

$$W = \sqrt{u_{\infty}^2 (1-a)^2 + \omega^2 r^2 (1+a')^2} \quad (2.6)$$

$$\phi = \text{Arcsin} \left[\frac{u_{\infty} (1-a)}{W} \right] \quad (2.7)$$

$$\alpha = \phi - \beta \quad (2.8)$$

- Based on the calculated AoA, calculate C_L and C_D from the aerodynamic performance curves that are available for different families of standard airfoils

- Calculate the blade solidity σ_r

$$\sigma_r = \frac{N}{2\pi} \frac{c}{r} \quad (2.9)$$

- Calculate the force coefficients known as C_x and C_y

$$C_x = C_L \cos \phi + C_D \sin \phi \quad (2.10)$$

$$C_y = C_L \sin \phi - C_D \cos \phi \quad (2.11)$$

- Based on all the known quantities, determine a and a' again as follows:

$$\frac{a}{1-a} = \frac{\sigma_r}{4 \sin^2 \phi} \left[C_x - \frac{\sigma_r}{4 \sin^2 \phi} C_y^2 \right] \quad (2.12)$$

$$\frac{a'}{1+a'} = \frac{\sigma_r C_y}{4 \sin \phi \cos \phi} \quad (2.13)$$

- If the new values of a and a' are sufficiently close to their previous guesses, STOP, and record the most recent AoA. Otherwise, go back to the second step and repeat

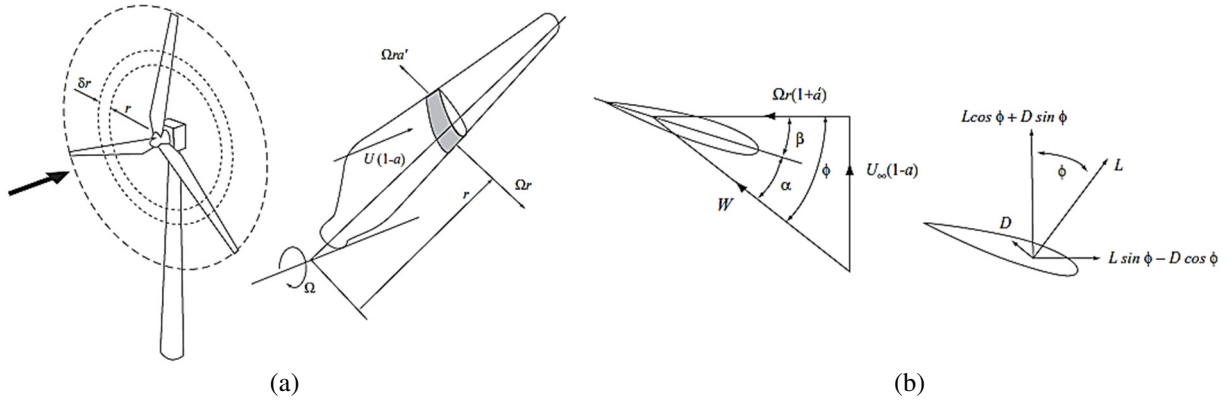


Figure 6 Aerodynamics of a HAWT blade: (a) 3D representation of the blade and the velocity vectors near blade, and (b) velocity and force vectors for an infinitesimal spanwise segment of the blade (Burton et al., 2011)

Using this technique, the effective angle of attack at various spanwise locations of a rotating wind turbine blade is determined. More details on the results of the CFD and experimental study conducted on two wind turbines with solid and slotted blades are presented in Chapter 7.

Chapter 3 Algebraic Stress Model

3.1 Introduction and Literature Review

Because of the fluid mechanics principles such as the development of a thin boundary layer over the ground surface, the modern commercial wind turbines have to be relatively large to be cost-effective. Currently, wind turbine blades as large as 80 m in length are manufactured and installed for commercial applications (WindPower Monthly, 2015). Some examples are Vestas V164 8MW turbine (80 m), and Siemens SWT 3:6 120 model (75 m). Because of the high manufacturing and transportation costs of the wind turbine components, it is necessary to evaluate the design and predict the performance of the turbine prior to shipping it to the site, where it is to be installed. Computational Fluid Dynamics (CFD) has proven to be a simple, and yet relatively accurate tool for prediction of wind turbine performance, where the suitability of different designs can be evaluated at a low cost. Total lift and drag forces can be calculated, from which one can estimate the torque and thrust forces, which are necessary for the determination of turbine power output, and dynamic (fatigue) loads.

Large Eddy Simulation (LES) is one of the most suitable turbulence treatment techniques. However, despite its superior behavior in the bulk fluid region, LES typically cannot make accurate predictions near the solid surfaces, unless the grid resolution is extremely fine. The hybrid schemes were introduced in order to overcome one of the main disadvantages of LES for wall-bounded turbulent flows. For a wall-bounded turbulent flow, the demand of fine grid resolution is great, especially in the vicinity of the walls for a high Re flow. Therefore, the hybrid LES-RANS strategies reduce the demand for fine grid resolution at the wall region. This can be achieved by using a RANS model at the wall region, while for the outer region, an LES approach

is adopted. Thus, the near wall turbulence is *modeled* instead of being fully resolved, and therefore, a relatively coarser grid may be used.

To form a hybrid LES-RANS model, there are at least two methods considered in the literature. In the first category, known as two-layer methods, LES is applied in a core region, while another set of equations is separately solved on a finer grid embedded between the edge of the core region and the wall surface. In the second category, known as Detached Eddy Simulation (DES), a single grid system is used to calculate the flow field, where the turbulence model changes from RANS in the near-wall region to LES in the core region (Abe, 2005). While there are several publications devoted to studying each methodology, there are not many studies handling the near-wall anisotropy of turbulence in a hybrid LES-RANS model. In fact, it is more common to adopt a linear eddy-viscosity model (LEVM), which is incapable of predicting the near-wall anisotropy correctly. This can be a serious concern when modeling complex flow conditions.

To address this problem, LES is combined with a customized form of RSM near the solid surfaces, in the present effort. RSM is a well-known RANS turbulence model, which is more accurate than eddy viscosity models. However, because of the presence of the additional governing equations to solve, this method requires a much higher computational cost. Therefore, in the present work, to improve LES predictions in the near-wall region, a modified version of RSM, known as the Algebraic Stress Model (ASM) is utilized for estimation of the RS component in the near-wall regions. Thus found Reynolds stresses will then be used to improve the predictions for flow quantities. Away from the blade wall, LES methodology is employed.

ASM is considered as a simplified version of RSM, which is obtained by eliminating the transport terms, and using a set of the algebraic energy equation. Explicit ASM (EASM) is

typically easy to implement for boundary layer flows. EASM are characterized by less computational demands and higher accuracy compared to linear eddy-viscosity models. First attempt for the derivation of EASM was done for two-dimensional flows (Pope, 1975), and it was later extended and modified for 3-D configurations (Gatski and Speziale, 1993; Jongen and Gatski, 1998). The mathematical equations of EASM are briefly reviewed in several other publications (Hellsten and Wallin, 2009; Alfonsi, 2009; etc.). A summary of the published work on ASM and hybrid models is presented here.

The ASM formulation has been used for aerodynamic applications only in a few publications. In one effort (Franke et al., 2005), two different explicit ASM techniques are used for assessment of flow in a variety of configurations in subsonic and transonic steady-state flows, including 2D airfoils and 3D aircraft wings. The first model is that of Wallin and Johansson (Wallin and Johansson, 2000), which is based on a recalibrated version of the so-called LRR model (Launder et al., 1975), and a fully explicit and self-consistent algebraic formulation is derived. The second model considered employs a less complex approach and is first suggested in 1999 (Rung et al., 1999). This model is based on the original EASM and uses linear truncation to define the relationship between the generation and dissipation terms (Gatski and Speziale, 1993). The validation studies carried out demonstrate the capabilities of the EASM models investigated. It is shown that the ERSM gives better results than some other RANS-based turbulence models such as the $k-\omega$ SST approach.

The anisotropy of turbulence in wind turbine wakes is also investigated numerically (Gomez-Elvira et al., 2005). A simplified explicit ASM, based on the formulation proposed in 1992 (Taulbee, 1992) is employed only in the wake region of the wind turbine (and not near the blades) and the results have shown to be in good agreement with experimental observations. The

turbulence nature becomes more isotropic as the center of the wake is approached. As a future work, it is suggested to perform LES to improve predictions.

Most of other investigations on ASM or hybrid LES-RANS are focused on flow around non-airfoil geometries. For instance, a family of EASMs is proposed for both Reynolds stresses and passive scalar fluxes (Ferrand and Violeau, 2012). For a steady closed channel flow, results are compared against DNS, and it is shown that the EASM can predict the anisotropy tensor when considering the near-wall effects. Results of the proposed model are then compared against the observations from an experiment on a heated cylinder with temperature variations. It is finally claimed that the proposed model can be applied to other simple 2D geometries in the presence of passive scalars.

Along with several other turbulence models, ASM is briefly reviewed in a recent study (Argyropoulos and Markatos, 2015). The more recent forms of the pressure strain terms proposed in the literature are addressed. It is indicated that *Main disadvantages of DSM (Differential Second-Moment) are the difficulty in the modeling of more terms in the turbulence equations and the increased demand on computer resources. The new generation of DSM closure models have solved most of the above-mentioned difficulties, but the computational demands are roughly twice as large as those for the two-equation models, for high-Re number flows using wall functions.*

To the best of the author's knowledge, a hybrid LES-ASM turbulence model has only been investigated a few times in the past. A hybrid LES-RANS approach using an algebraic turbulence model is investigated (Abe, 2005). An advanced nonlinear eddy-viscosity model is utilized in order to resolve better the near-wall stress anisotropy for a fully-developed plane channel flow problem. It is shown that the accuracy of the Reynolds stresses predicted in the

near-wall region is improved using the proposed model. In the meantime, it is suggested that some improvements are needed for the predictive performance of the model for complex high Re turbulent flows involving separation, which is typical for wind turbine applications. The same methodology is used in another effort by the same author (Abe, 2014), where the switching point between RANS and LES schemes is identified. This model is exemplified using problems of fully developed channel flow as well as a periodic hill flow, with various grid resolutions and at various Reynolds numbers.

A hybrid turbulence model of Explicit ASM with LES approach is suggested and tested (Jaffrézic, Breuer, 2008). It is concluded that *EARSM accounts for the strong anisotropy of the Reynolds stresses found in the vicinity of the wall and thus involves a better physical background. Especially the plane channel flow test case but also the hill flow case have proven that the prediction of the Reynolds stresses is significantly improved by the EARSM used in the near-wall RANS zone.*

Even though ASM has been employed in several publications to investigate a wide variety of applications (Gomez and Girimaji, 2014; Weinmann et al., 2014; etc.), it has never been combined with LES or DES for a wind turbine application. The comparison of implicit and explicit ASMs with RSM has also rarely been considered. In the present effort, we start with employing ASM formulation to a two-dimensional problem, where the incompressible air flow passes over a flat plate, and the zero-pressure-gradient boundary layer is formed. Different variations of implicit ASM and one explicit ASM are examined, and results are compared in terms of accuracy and the computational cost. The results of this initial study help us to get an idea of the appropriate ASM models. After conducting that first study, the same methodology is used to analyze flow over wind turbine blades using ASM technique.

The objective of this study is two-fold. Primarily, it is desired to see if it is possible to replicate the near-wall Reynolds stresses by employing a relatively less computationally intensive approach, such as different versions of ASM. The second, more important objective is to find out the effects of thus obtained Reynolds stresses on the flow predictions near the solid surface. To do so, the results of baseline DES model is augmented with the flow quantities obtained by ASM.

The numerical simulation procedure for both 2D flat plate (*plate*) and wind turbine blade (*blade*) problems is described in more details in section 3.4, and the details of the hybrid DES-ASM model is left to the next chapter of this dissertation.

3.2 Theory

3.2.1 ASM Formulation Development

The governing equation for turbulent flow can be described in terms of the mean quantities and fluctuating velocities. The continuity and momentum equations can be written as

$$\nabla \bar{U}_i = 0 \quad (3.1)$$

$$\frac{\partial \bar{U}_i}{\partial t} + \frac{\partial \bar{U}_i \bar{U}_j}{\partial x_j} = -\frac{1}{\rho} \frac{\partial \bar{P}}{\partial x_i} + \frac{\partial}{\partial x_i} \left[\nu \left(\frac{\partial \bar{U}_i}{\partial x_j} + \frac{\partial \bar{U}_j}{\partial x_i} \right) - \overline{u_i u_j} \right] \quad (3.2)$$

The governing differential equation for the Reynolds stresses can be expressed in the following compact form (Chen and Jaw, 1998):

$$\frac{D \overline{u_i u_j}}{Dt} = D_{ij} + P_{ij} - \frac{2}{3} \delta_{ij} \varepsilon + \Phi_{ij} \quad (3.3)$$

The pressure strain term, Φ_{ij} , is the tendency to return to the isotropicity by redistribution of different Reynolds stress components. Each of the terms above is explained here:

$$P_{ij} = - \left(\overline{u_i u_k} \frac{\partial U_j}{\partial x_k} + \overline{u_j u_k} \frac{\partial U_i}{\partial x_k} \right) \quad (3.4)$$

$$D_{ij} = - \left(\overline{u_i u_k} \frac{\partial U_k}{\partial x_j} + \overline{u_j u_k} \frac{\partial U_k}{\partial x_i} \right) \quad (3.5)$$

$$\varepsilon = \nu \overline{\frac{\partial U_i}{\partial x_j} \frac{\partial U_i}{\partial x_j}} \quad (3.6)$$

The pressure strain term is composed of three main terms, i.e., $\Phi_{ij,1}$ involving only the fluctuating quantities, $\Phi_{ij,2}$ arising from the presence of the mean rate of strain, and $\Phi_{ij,w}$ due to the near-wall proximity effect. These three terms can be shown to be estimated as

$$\Phi_{ij,1} = -c_1 \frac{\varepsilon}{k} \left(\overline{u_i u_j} - \frac{2}{3} \delta_{ij} k \right) \quad (3.7)$$

$$\Phi_{ij,2} = -\frac{c_2 + 8}{11} \left(P_{ij} - \frac{2}{3} \delta_{ij} P_k \right) - \frac{30c_2 - 2}{55} k \left(\frac{\partial U_i}{\partial x_j} + \frac{\partial U_j}{\partial x_i} \right) - \frac{8c_2 - 2}{11} \left(D_{ij} - \frac{2}{3} \delta_{ij} P_k \right) \quad (3.8)$$

$$\Phi_{ij,w} = \left\{ 0.125 \frac{\varepsilon}{k} \left(\overline{u_i u_j} - \frac{2}{3} \delta_{ij} k \right) + 0.015 (P_{ij} - D_{ij}) \right\} \frac{k^{1.5}}{\varepsilon h} \quad (3.9)$$

The total pressure strain will be then defined as

$$\Phi_{ij} = \Phi_{ij,1} + \Phi_{ij,2} + \Phi_{ij,w} \quad (3.10)$$

In the equations above, k represents the turbulent kinetic energy (defined as $k = \overline{u_i u_i} / 2$), h is the distance from the solid wall, and c_1 (~ 1.5) and c_2 (~ 0.4) are coefficients that are obtained experimentally in the literature. Moreover, in the equations above, P_k represents the production term for the kinetic energy, and is given as

$$P_k = -\overline{u_i u_j} \frac{\partial U_i}{\partial x_j} \quad (3.11)$$

Despite its accuracy, Eq. (3.3) is a differential equation in terms of the Reynolds stresses, and therefore, it requires solving multiple partial differential equations concurrently. However, it can be shown that in the vicinity of the solid wall, one can use the following approximation (Rodi, 1972):

$$\frac{D \overline{u_i u_j}}{Dt} - D_{ij} = \frac{\overline{u_i u_j}}{k} \left(\frac{Dk}{Dt} - D_k \right) = \frac{\overline{u_i u_j}}{k} (P_k - \varepsilon) \quad (3.12)$$

and therefore, rewrite Eq. (3.3) as

$$\frac{\overline{u_i u_j}}{k} (P_k - \varepsilon) = P_{ij} - \frac{2}{3} \delta_{ij} \varepsilon + \Phi_{ij} \quad (3.13)$$

which is an *algebraic* equation for the Reynolds stress components, and hence, this is called the governing equation for Algebraic Stress Model (ASM) due to its nature, which is free of the convection terms. Partial derivatives of $\overline{u_i u_i}$ terms are no longer involved. Since k , diffusion term, and production terms all include more than one Reynolds stress components, Eq. (3.13) cannot be solved explicitly for a given $\overline{u_i u_j}$, but the 3-D system of the algebraic equations for the six Reynolds stress components needs to be solved simultaneously. Note the mean velocity gradients should be readily available before proceeding with ASM. This requires the flow field to be solved beforehand with possibly a less complex turbulence model.

3.2.2 Different Versions of ASM

Equation (3.10) is one of the most comprehensive representations of the pressure-strain term. There are several other models reported in the literature for inclusion of the pressure strain effect in the Reynolds stress equation. In one of the common approximations, it is assumed that the first group in the right-hand side of Eq. (3.8) is the dominant term, and therefore, next two terms are dropped, and the coefficient group $-(c_2+8)/11$ is adjusted accordingly. This method is called compact $\Phi_{ij,2}$ and is expressed as (Launder et al., 1975):

Compact $\Phi_{ij,2}$:
$$\Phi_{ij,2} = -\gamma \left(P_{ij} - \frac{2}{3} \delta_{ij} P_k \right) \text{ with } \gamma=0.6 \quad (3.14)$$

The next approximation is made by completely ignoring the wall proximity effects. Since one of the main assumptions in the derivation of ASM formulation is specifically valid for the near wall region – see Eq. (3.12) – it is unlikely that the elimination of wall effects can result in accurate predictions. In this case, the pressure strain term will be used as the summation of the first two contributing terms:

No wall effect:
$$\Phi_{ij} = \Phi_{ij,1} + \Phi_{ij,2} \quad (3.15)$$

The next possible ASM formulation is regarding the treatment of the wall function. The term $k^{1.5}/(\epsilon h)$ on the right-hand side of Eq. (3.9) can be shown to be equivalent to l/h , where l can be interpreted as the dissipation length, $k^{1.5}/\epsilon$. According to the LRR model (Launder et al., 1975), this term is supposed to be an arbitrary function of l/h , i.e., $f(l/h)$, with the requirement of vanishing as l/h approaches zero. Only for simplicity, it is set as $f(l/h)=l/h$, and hence Eq. (3.9) is obtained. In general, this function can have any other form (e.g. a quasi-linear form), as long as it goes to zero when l/h approaches zero.

Explicit ASM:

All of the variations of ASM discussed so far belong to the family of implicit methods, as it is necessary to solve a system of equations concurrently to determine individual Reynolds stresses. To expedite the simulation, explicit algebraic stress model (EASM) was proposed first for two-dimensional flows (Pope, 1975), where the system of equations was transformed to an explicit form, and therefore it was made possible to obtain individual Reynolds stresses independently. Later, a more general form of this model was developed (Gatski and Rumsey, 2002). The final form of the resultant equation can be expressed as

$$\frac{\langle u_i u_j \rangle}{k} - \frac{2}{3} \delta_{ij} = -\lambda_1 \tilde{S}_{ij} - \lambda_2 (\tilde{S}_{ik} \tilde{W}_{kj} + \tilde{S}_{jk} \tilde{W}_{ki}) + \lambda_3 \left(\tilde{S}_{ik} \tilde{S}_{kj} - \delta_{ij} \frac{S^2}{3} \right) \quad (3.16)$$

where the dimensionless strain and rotation parameters (Hanjalic and Launder, 2011) are defined by

$$\tilde{S}_{ij} \equiv \frac{1}{2} \frac{k}{\epsilon} \left(\frac{\partial U_i}{\partial x_j} + \frac{\partial U_j}{\partial x_i} \right), \quad \tilde{W}_{kj} = \frac{1}{2} \frac{k}{\epsilon} \left(\frac{\partial U_i}{\partial x_j} - \frac{\partial U_j}{\partial x_i} \right), \quad S = \sqrt{\tilde{S}_{mn} \tilde{S}_{mn}} \quad (3.17)$$

Furthermore, the λ coefficients used in Eq. (3.16) can take the form of

$$\lambda_1 = n \left(\frac{4}{3} - c_2 \right), \quad \lambda_2 = \frac{1}{2} n^2 (2 - c_4) \left(\frac{4}{3} - c_2 \right), \quad \lambda_3 = n^2 (2 - c_3) \left(\frac{4}{3} - c_2 \right) \quad (3.18)$$

where the parameter n is defined as

$$n=(c_1/2+P_k/\varepsilon-1)^{-1} \quad (3.19)$$

and c_i coefficients take the following values:

$$c_1=3.6, \quad c_2=0.8, \quad c_3=1.2, \quad c_4=1.2 \quad (3.20)$$

Finally note that more complex forms of EASM are proposed in the literature (Antonello, and Masi, 2007; Argyropoulos, and Markatos, 2015; etc.), but the present investigation is restricted to the *simple* Explicit ASM approach (Hanjalic and Launder, 2011).

3.3 Problem Description

To establish the idea of the significance of the ASM formulation, two different problems are investigated. First, turbulent air flow over a 2D flat plate is investigated. While the ultimate goal is to study the flow around wind turbine blades, we believe that this 2D study will provide good insights into the benefits of employing ASM. After evaluating different ASM methods in terms of their accuracy and computational costs, in the next steps, flow around a three-blade horizontal axis wind turbine is analyzed.

3.3.1 Flat Plate

Figure 7 shows the domain of interest for the analysis of turbulent air flow over a 2D flat plate. Air with the uniform velocity of 15 m/s enters the domain from the left boundary; it passes over the plate, and then exits the domain from the right boundary. Total length of the plate and height of the computational domain are 4m and 0.5m, respectively. The height is chosen such that the dynamics of flow in the top boundary is not influenced by the wall boundary, and therefore, the external flow condition can be assumed safely. Note the plate length and air speed are chosen such that the flow condition resembles that considered in the experimental study carried out by Klebanoff (Klebanoff, 1955), where the four Reynolds stress components are determined at a certain distance from the leading edge, with the Reynolds number Re_x of $3.2e6$. The Reynolds number based on the local length of the plate is defined as

$$Re_x = \frac{\rho U_\infty x}{\mu} \quad (3.21)$$

It is desired to obtain the distribution of the Reynolds stress components on a vertical line normal to the plate using multiple ASM versions and compare the results with those found from the fully converged RSM. The results will also be compared with Klebanoff's data when applicable.

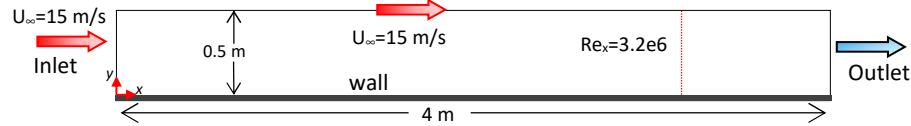


Figure 7 Schematic diagram of the domain

3.3.2 Wind Turbine Blade

Figure 8a shows the computational domain for the analysis of turbulent air flow around and over a horizontal axis wind turbine with three blades. To save computational time, only one blade inside a 120-degree sector of the cylindrical domain is studied. Uniform air flow enters the domain from the left boundary, it passes around the blade, and leaves the domain from the right surface. Figure 8b shows the position of the blade inside the domain, where the normalized distances between the blade and different sides of the computational domain are shown. The upstream and downstream lengths of the domain were $10L$ and $20L$, respectively, where L is the blade length from the hub center to the tip. The radius of the cylindrical domain is set to $7.5L$. It is shown in a different study (Malloy, 2009) that such distances are large enough to guarantee that the boundaries have negligible impact on the dynamics of flow around the blade, and therefore, computational results are independent of the domain size. It can be then assured that the domain is a realistic representation of an external flow. The velocity of entering air is set to 7 m/s, and the rotational speed of the blade is 2.4 rad/s. The blade airfoil profile chosen for this study is National Advisory Committee for Aeronautics (NACA) 4412 throughout, because of its high lift to drag ratio (~ 70) and its popularity in wind turbine applications.

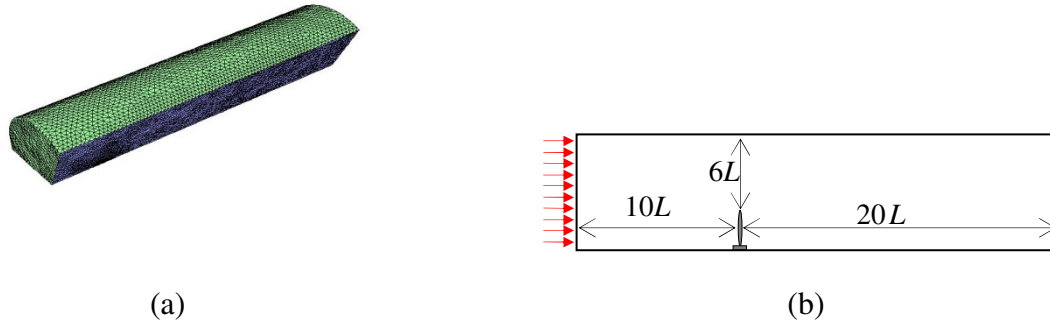


Figure 8 Computational domain for wind turbine blade study, (a) 3D representation of the gridded volume, (b) side view with the dimensions shown relative to the blade height, L (not to the proper scale)

Figure 9a shows the blade that is generated in Pro/Engineer. The total length of the blade L is 20 m, with the maximum chord length of 3.05 m near the hub, and with the maximum twist angle of 43.74 deg at the hub, and 0.56 deg at the tip.

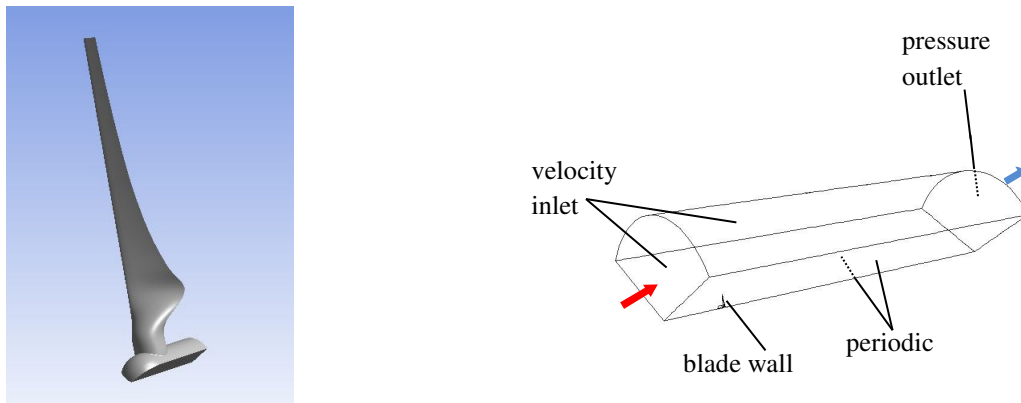


Figure 9 (a) NACA 4412 wind turbine blade with one third of the hub shown, (b) computational domain with the BCs shown

3.4 Numerical Simulation

The algorithm and procedure used for determination of the Reynolds stresses using ASM technique is used for both flat plate and blade problems, and is summarized as follows:

- Solve the flow field and turbulence everywhere in the domain using the RANS based $k-\epsilon$ turbulence model.
- Store all the mean velocity gradients, as well as k and ϵ distribution in the areas of interest (near the solid walls).

- c) Solve the flow field only for a few iterations to find somewhat reasonable estimates for the Reynolds stresses, to be used as initial guesses for ASM. Alternately, some arbitrary constant values can be used, perhaps average values from some previous simulations.
- d) Solve the system of algebraic equations, Eq. (3.13), for six unknown Reynolds stresses, $\overline{u_1 u_1}, \overline{u_1 u_2}, \overline{u_1 u_3}, \overline{u_2 u_2}, \overline{u_2 u_3}, \overline{u_3 u_3}$ (for the wind turbine blade problem), or four unknown Reynolds stresses, $\overline{u_1 u_1}, \overline{u_1 u_2}, \overline{u_2 u_2}, \overline{u_3 u_3}$ (for the 2D flat plate problem)
- e) Finally, to assess the accuracy of the ASM results, solve the flow field everywhere using the standard RSM turbulence model, and compare the results with those obtained via ASM in the near-wall region.

The study above is only carried out to give an idea of the feasibility of using ASM, and also the relative accuracy of the predictions with respect to either experimental or computational (fully-converged RSM) results. The next step would be to start with either dummy or fully-converged Reynolds stresses, and modify them using ASM formulation, and combine it with LES or DES.

Two software packages were utilized for different parts of the present numerical simulation. ANSYS Fluent was used for initial modeling of the flow both over the plate, and around the wind turbine blade for determination of mean velocity gradients and turbulent energy dissipation rate. The $k-\varepsilon$ model was used for this purpose. Additionally, flow and turbulence were determined using the more complex RSM model for comparison purposes. In both cases, a pressure-based steady-state solver with segregated pressure-velocity algorithm was chosen. Operating condition of the air was set to 25 °C and 101.3 kPa. A standard spatial discretization was considered for pressure, while the second order upwind method was used for k , ε , and Reynolds stresses. Convergence criteria of 1.0E-6 were chosen for continuity, three velocity

components, k and ε equations, and all four Reynolds stress components. Note that for the wind turbine blade problems, the Reynolds stresses were only converged down to the residuals of $1e-4$. A problem similar to the wind turbine blade analysis is investigated elsewhere (Amano et al., 2013). Note that $\langle uu \rangle$, $\langle uv \rangle$, $\langle uw \rangle$, $\langle vv \rangle$, $\langle vw \rangle$, $\langle ww \rangle$ are occasionally used in lieu of $\overline{u_1 u_1}$, $\overline{u_1 u_2}$, $\overline{u_1 u_3}$, $\overline{u_2 u_2}$, $\overline{u_2 u_3}$, $\overline{u_3 u_3}$, respectively. More details on specific settings of the two computational studies are provided in the next two sub-sections.

Once the flow field was obtained using the chosen mesh, the parameters needed to be used as input for the ASM formulations were stored. Those were mean velocity gradients and energy dissipation rate. A short code was developed in MATLABTM to implement the ASM formulation into the computational loop and solve the system of algebraic equations for the Reynolds stresses. This software was chosen mainly due to its significant capabilities in terms of handling large data and efficient matrix operations. Two methods considered for solving the system of equations were the built-in *fsolve* function from MATLAB Optimization toolboxTM, as well as a successive substitution routine. The computations were decided to be performed using *fsolve* function since it showed a better convergence and more robust performance.

3.4.1 Model Setup and Mesh Generation: Flat Plate

Referring to Figure 7, the velocity inlet condition was imposed at the inlet boundary as well as the top boundary, with the uniform velocity U_∞ of 15 m/s normal to the inlet boundary, turbulent intensity of 1%, and turbulent viscosity ratio of 10. Pressure-outlet condition was imposed on the outlet surface, and the outlet gauge pressure was set to zero.

Mesh generation was carried out in ANSYS design/meshing environment. The Match control feature was used to ensure the mesh details on the wall, and the top boundary were identical. Moreover, the inflation feature was used to locally refine the mesh near the solid wall. The

growth ratio of 1.1 was used for this purpose. The height of the first row of cells adjacent to the solid wall was chosen fine enough to ensure the y^+ of around one everywhere. After completion of all of the simulations, the y^+ parameter was verified to be always in the 0.1-0.9 range along the plate, with the average value of about 0.3. A grid independence study was carried out, where the drag coefficient was monitored for each grid configuration chosen. The results of this study are presented in Figure 10.

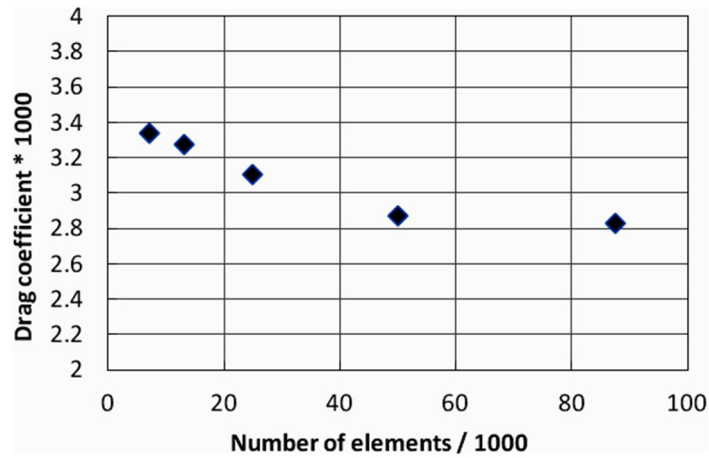
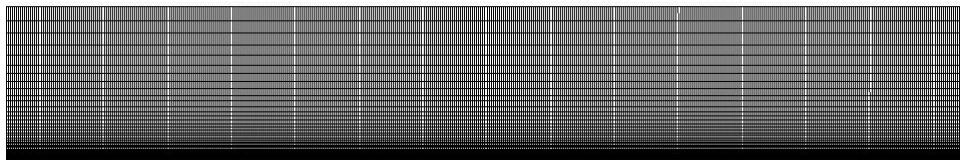


Figure 10 Results of the mesh independence study for flat plate problem

It can be seen in Figure 10 that the difference between the drag coefficient of the two cases with the highest number of mesh elements (i.e., 50,000 and 87,000) is only about 1.5%. Therefore, a fully structured mesh with about 50,000 quadrilateral elements was chosen for the present study. The computational domain is shown in Figure 11a.



(a)

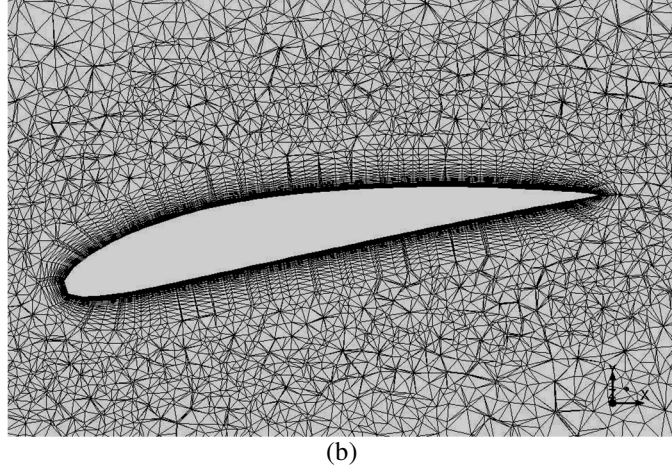


Figure 11 (a) Grid chosen for the flat plate problem in the entire computational domain; and (b) Grid used in the near blade region at a distance $z=10m$ ($z/L=0.5$) from the hub

3.4.2 Model Setup and Mesh Generation: Wind Turbine Blade

Referring to Figure 9b, the velocity inlet condition was imposed at the inlet boundary as well as the ‘top’ boundary, with the uniform velocity U_∞ of 7 m/s normal to the inlet boundary, turbulent intensity of 1%, and turbulent viscosity ratio of 10. Pressure-outlet condition was imposed at the outlet surface, where the gauge pressure was set to 0. The two side surfaces of the 120-degree domain were assigned a periodic boundary condition (Figure 9). Moreover, a moving reference frame function in ANSYS Fluent was considered in the calculations, in order to implement the rotation of the domain without having to use sliding or deformable mesh. In other words, the blade was considered stationary, and the fluid region was given a rotational velocity component (2.4 rad/s), and periodic condition was applied to the two side boundaries.

Grid generation was again performed in ANSYS. The patch conforming algorithm was utilized to properly couple the two periodic boundaries. Moreover, the *inflation* feature was used in order to refine locally the mesh near the blade walls. The number of inflation layers was chosen as 30, with the growth ratio of 1.2. The first cell height was chosen such that average y^+ near the blade surface was around 1~2. A mesh independence study was carried out, where the

generated power of a wind turbine with three blades was calculated each time the mesh was refined. The following equation was used to determine the power:

$$\text{Power} = nT\omega \quad (3.22)$$

The power generated for each case is as follows:

Number of elements = 4.8 M \rightarrow Power = 85.7 kW

Number of elements = 6.3 M \rightarrow Power = 81.9 kW

Number of elements = 8.8 M \rightarrow Power = 80.4 kW

Since the difference between the last two cases was less than 2%, the grid with 6.3 M elements was chosen for the computational analysis. The mesh generated near the blade at the distance of 10m from the hub ($z/L=0.5$) is depicted in Figure 11b.

3.5 Results and Discussions

3.5.1 Flat Plate

3.5.1.1 Velocity profiles

The first set of results investigated is the velocity profiles at two distinct distances from the leading edge, one in the laminar region ($Re_x \sim 8e4$) and the other one in the fully turbulent region ($Re_x \sim 3.2e6$). For the laminar region, velocity profiles are compared against two well-known correlations from the literature, i.e., the Blasius solution, and the Karman approximate relationship for laminar flow (White, 2011). In Blasius equation, the normalized velocity can be found after a coordinate transformation and solving a simple ordinary differential equation. The solution is well documented in the literature and has the form of

$$u/U_\infty = f' \left(y \sqrt{U_\infty / \nu x} \right) \quad (3.23)$$

Where f' values are listed in the same reference (White, 2011). In Karman solution, it is assumed that the velocity profile has a parabolic shape and is found as

$$u/U_{\infty} = 2y/\delta_{BL} + (y/\delta_{BL})^2 \quad \text{for } 0 \leq y \leq \delta_{BL}(x) \quad (3.24)$$

The boundary layer thickness can then be estimated as

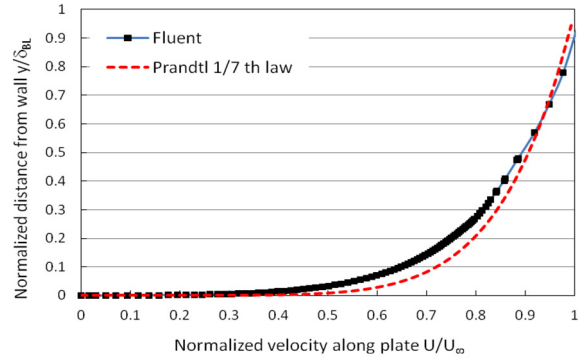
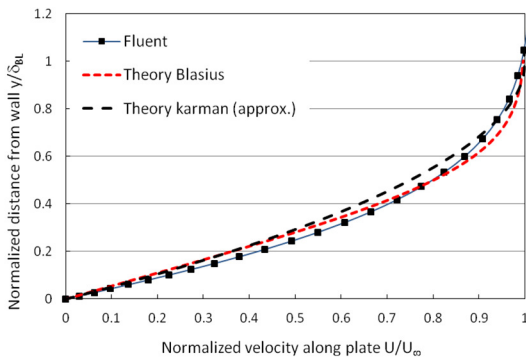
$$\frac{\delta_{BL}}{x} \approx \frac{5.0}{Re_x^{1/2}} \quad (3.25)$$

The distribution of the velocity profiles in the laminar region is shown in Figure 12a. There exists a good agreement between the velocity predictions and both of the theoretical relationships for the near wall region, from wall up to $y/\delta_{BL} < 0.3$. For $0.3 < y/\delta_{BL} < 0.8$, Fluent slightly underpredicts the velocities, and then above that point up to $y/\delta_{BL} = 1$, Fluent predictions lies between those of the two models. Since the main focus of this ASM study is on the near wall region ($y/\delta_{BL} < 0.4$), we can safely proceed with the simulations.

For the turbulent region, Prandtl's 1/7th law describes the relationship between the velocity component along the plate and the distance from the plate as follows (White, 2011):

$$\frac{u}{U_{\infty}} \approx \left(\frac{y}{\delta_{BL}} \right)^{1/7}, \quad \delta_{BL} = \frac{0.16x}{Re_x^{1/7}} \quad (3.26)$$

As shown in Figure 12b, there is an acceptable agreement between the model velocity predictions and those from Eq. (3.24) from wall up to $y/\delta_{BL} < 0.4$. Even though there are some discrepancies for $0.4 < y/\delta_{BL}$, we can proceed with the simulation as the ASM formulation is intended to be used only for the near wall region.



(a)

(b)

Figure 12 Distribution of the velocity component along the plate at two different regions along the plate, along with comparison with available data from the literature, (a) laminar region, $Re_x=8e4$, and (b) turbulent region, $Re_x=3.2e6$.

3.5.1.2 Reynolds stresses

It is now desired to find the distribution of the four Reynolds stress components at a certain distance from the leading edge and compare them with the available data. For the comparison purposes, the well-known experimental data (Klebanoff, 1955) is used, where the Reynolds stresses normalized by the inlet velocity are reported at a position with $Re_x \sim 3.2e6$. The ASM formulation described in the Theory section is used to obtain all Reynolds stress components. Results of the most comprehensive form of the implicit ASM model, as well as the explicit ASM, are depicted. Finally, the predictions of the fully converged RSM simulation are shown in order to assess the accuracy of each one of the ASM models.

As shown in Figure 13, the level of agreement between the predictions of RSM, four ASM versions, and the experimental data are different for different Reynolds stress components, and therefore it is necessary to analyze these components separately. For the largest Reynolds stress component $\langle uu \rangle$, the implicit formulation tends to make slightly better predictions as compared to the explicit model. For component $\langle ww \rangle$, the explicit ASM is significantly off, while the RSM and three implicit ASMs seem to be acceptable. Note that for the positions slightly further away from the wall ($0.25 < y/\delta_{BL}$), implicit ASM appears to be even better than RSM. Similar behavior is observed for the component $\langle uv \rangle$. While explicit ASM fails to predict the values everywhere, the results of the full implicit ASM model are very close to RSM and experimental data. Note that ‘implicit ASM No Wall’ model slightly overpredicts $\langle uv \rangle$ everywhere. Finally, for $\langle vv \rangle$ component, the three implicit ASM model show some discrepancies with the results of the other models. Among the three implicit ASM models, the results of the compact model are slightly closer to the experimental data. Note that even in this case, the maximum error of the

ASM models is only 25%. Overall, based on the results presented so far, it looks like predictions of the full implicit ASM model are almost as accurate as the fully converged RSM simulation from Fluent (except $\langle vv \rangle$), while there is a significantly less computational time required.

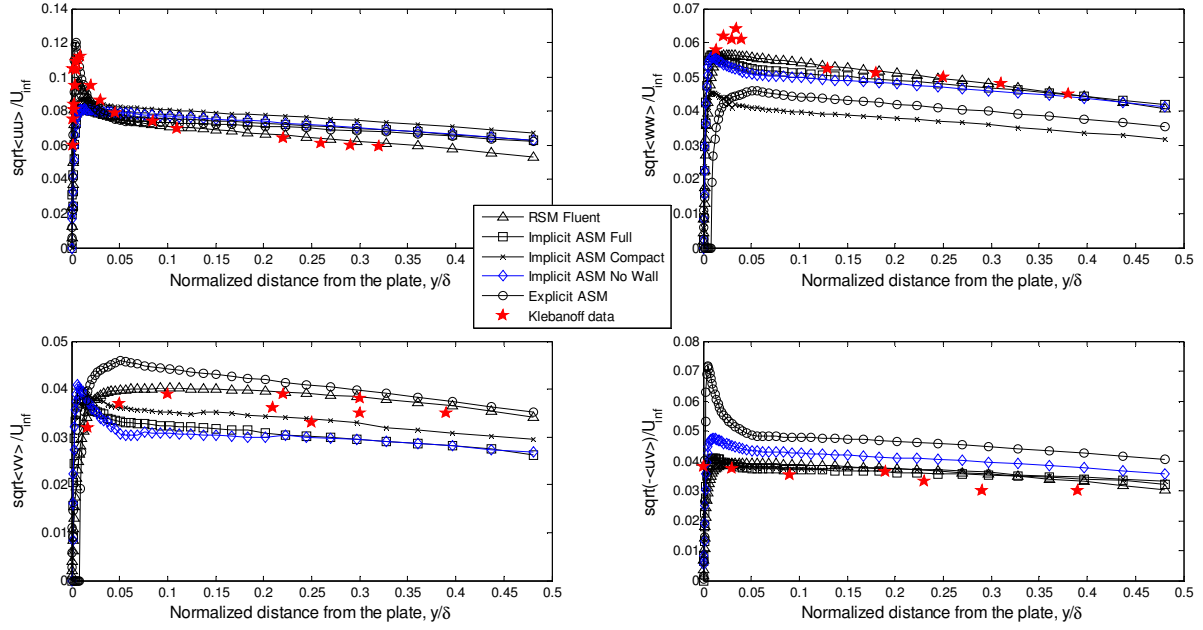


Figure 13 Distribution of the normalized Reynolds stress components versus the normalized distance from the plate in the near-wall region, for $Re_x=3.2e6$.

3.5.1.3 Accuracy and computational cost

In Table 1, some information about different ASM models is presented for the 2D flat plate problem. RSM is considered as the baseline model, and the root mean square of the error percentages of the four Reynolds components using four ASMs (with respect to RSM) is tabulated. Also listed is the computational time of all ASMs (which includes the time spent on the k- ϵ simulation), and RSM. It is evident that among all ASMs, the full implicit ASM model shows smallest average difference with RSM for $\langle vv \rangle$, $\langle ww \rangle$, and $\langle uv \rangle$, while the explicit ASM has the lowest average difference with RSM for $\langle uu \rangle$. However, this model gives poor results for other RS components. Also, the computational time of each one of the ASMs is about 6 times shorter than that of RSM, while the compact and No-Wall implicit ASMs are not much faster

than the full implicit model. Overall, it appears that using the full implicit ASM can be a good trade-off between accuracy and computational cost.

Model	Average $\langle uu \rangle$ difference %	Average $\langle ww \rangle$ difference %	Average $\langle vv \rangle$ difference %	Average $\langle uv \rangle$ difference %	Approx. sim. time (min)
RSM	---	---	---	---	180
Implicit ASM (Full)	12.5	12.6	36.0	11.3	35
Implicit ASM (Compact)	14.4	22.0	39.2	11.4	33
Implicit ASM (No Wall)	13.4	12.8	43.7	23.2	33
Explicit ASM	12.1	48.5	44.5	66.3	32

Table 1 Average differences between ASMs and RSM predictions

3.5.2 Wind Turbine Blade

In order to get a visual overview of the air flow over the wind turbine blade, the variation of the axial velocity on the vertical mid-plane of the computational domain and along the main flow direction is shown in Figure 14.

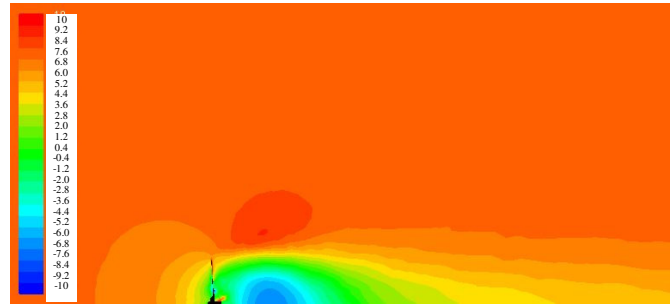


Figure 14 Contours of the axial velocity in the vertical mid plane (units are in m/s)

Next, the results of the Reynolds stresses updated by ASM formulation are presented. Note that the ASM analysis is carried out at only a few positions (heights) along the blade span, and only on few concentric layers around the blade surface. The normalized heights selected for analysis were $z/L=0.25$, 0.5 , and 0.75 . It will be more comprehensive to extend the analysis to everywhere in the flow domain up to a certain distance from the blade wall. Figure 15 is taken at

$z/L=0.5$, and demonstrates the x - and y -coordinates of every data point of interest around the blade with the approximate wall distance h of 1 mm, or $h/L=5e-5$. Indices assigned to the data points are shown as well, and will be referred to in Figure 16 through Figure 21.

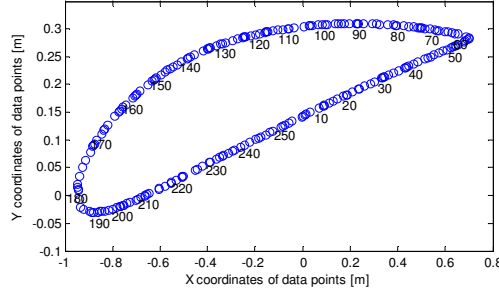


Figure 15 Indices of grid points of interest around the blade at $z/L=0.5$, and $h/L=5e-5$

The next set of figures shows the distribution of six RS components as calculated by the ASM formulation. They are all normalized by the square of the inlet velocity of the computational domain, U_∞^2 . For the sake of comparison, the same quantity is calculated by the fully-converged RSM (from Fluent) and is shown in the same figure. The RSM formulation uses the linear pressure strain term and includes the wall reflection effects. It seems to be very similar to the full $\Phi_{ij,2}$ model considered in the present study. Figure 16 is corresponding to $z/L=0.5$ and $h/L=5e-6$. The notation $\langle uu \rangle$, $\langle uv \rangle$, $\langle uw \rangle$, $\langle vv \rangle$, $\langle vw \rangle$, $\langle ww \rangle$ is used in lieu of $\overline{u_1 u_1}, \overline{u_1 u_2}, \overline{u_1 u_3}$, $\overline{u_2 u_2}, \overline{u_2 u_3}, \overline{u_3 u_3}$, respectively. Results of the full implicit model, explicit model, and RSM are plotted. There is a good agreement between implicit ASM and RSM results. While for the four of the Reynolds stress components, the agreement between implicit ASM and RSM is very good, for the other two components, the overall trend is acceptable. There is a small amount of scattering for $\langle vv \rangle$ which can be attributed to MATLAB solver converging to different solutions, based on the criteria chosen for convergence. While the explicit ASM also predicts the trends decently, it fails to make predictions as accurate as the implicit ASM. This could be due to the assumptions made during the derivation of the explicit formulation.

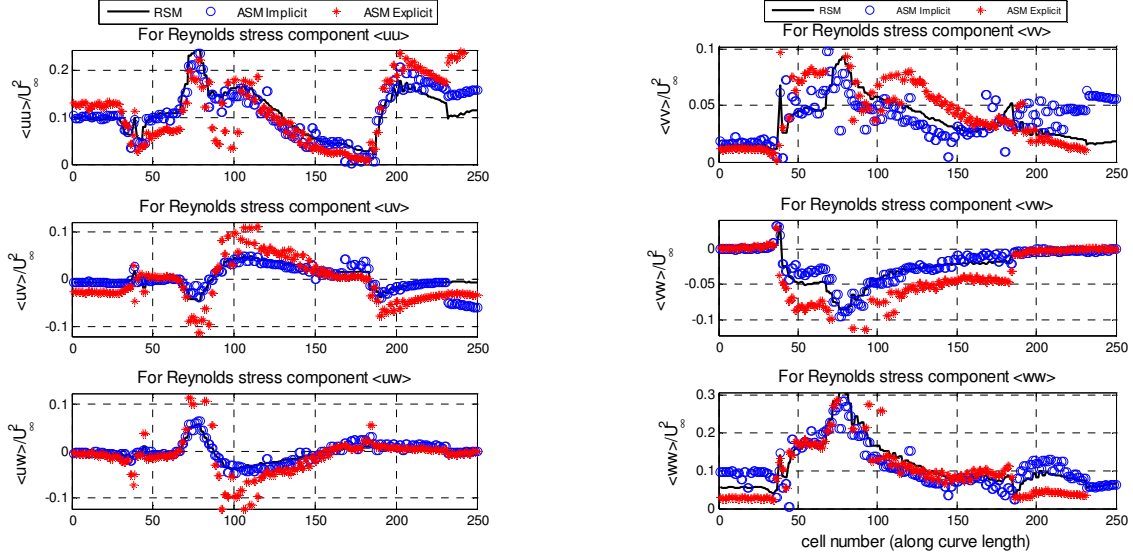


Figure 16 Distribution of the normalized Reynolds stresses around the blade at $z/L=0.5$, and $h/L=5e-6$ (RSM, full implicit ASM, and explicit ASM)

It is now desired to check the relative accuracy of the two other variations of the ASM formulations, i.e., the *compact* $\Phi_{ij,2}$ form, Eq. (3.14), and *no wall effect* form, Eq. (3.15), in comparison with the case where the complete form of $\Phi_{ij,2}$ and $\Phi_{ij,w}$ are used. Figure 17 and Figure 18 show the component-by-component distribution of the normalized Reynolds stresses near the blade wall. Remember the x - and y -coordinates of the data points for each cell number is shown in Figure 15. For better clarity, the explicit ASM results are not shown here, but a comparison between all implicit models and the one explicit model for $\langle uu \rangle$ is shown in Figure 19.

As shown in Figure 17, the trend of implicit ASM predictions is decent, although as expected, the overall agreement between RSM and this compact model is not very good. There are areas where the MATLAB solver did not converge, which could be due to the inaccuracies induced in the solution because of the simplifications made for the compact model. On the other hand, the No-wall effect form (Figure 18) seems to capture the overall behavior of the Reynolds

stresses better. There is less scatter of data observed, but still the agreement with RSM is not acceptable, most probably due to dropping the wall-effect term in the near-wall region.

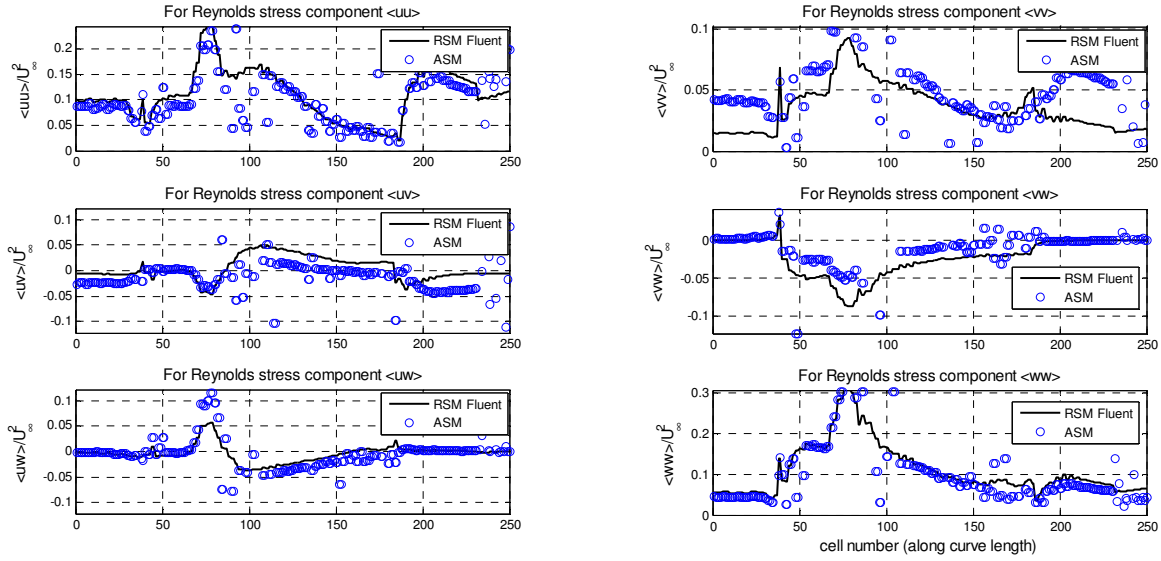


Figure 17 Distribution of the normalized Reynolds stresses around the blade at $z/L=0.5$, and $h/L=5e-6$ (Compact $\Phi_{ij,2}$ form)

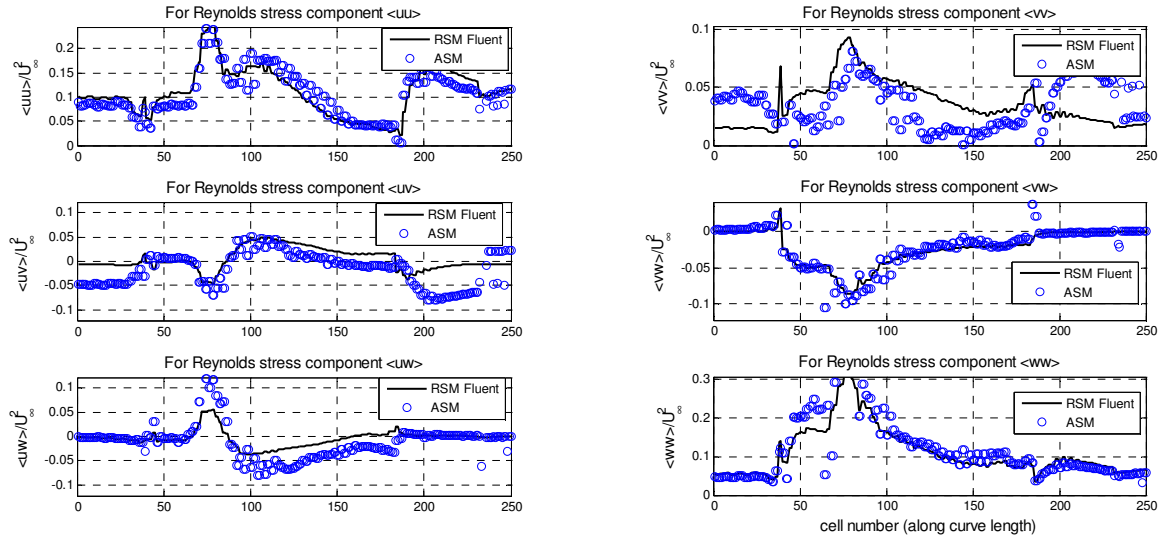


Figure 18 Distribution of normalized Reynolds stresses around the blade at $z/L=0.5$, and $h/L=5e-6$ (No wall effect)

It may also be useful to show the distribution of at least one Reynolds stress component along the blade curve for three different implicit and explicit ASM models all in one plot. As can be seen in Figure 19, even though the general trends of all models are good, none of the models can perfectly replicate the RSM results. However, the full implicit model shows better agreement

with the RSM data, and there are fewer outliers in this model. The explicit ASM seems to have the highest scatter of data, and is less accurate than the compact and no-wall implicit models. It is also interesting to note that the model ignoring wall effect results in slightly better predictions as compared to the ‘compact’ model. Note there is not much of a difference between the computational times of the three implicit models, although the explicit model is slightly faster. In order to be able to make a conclusion about the most suitable method, the simulation is repeated for different locations around the blade.

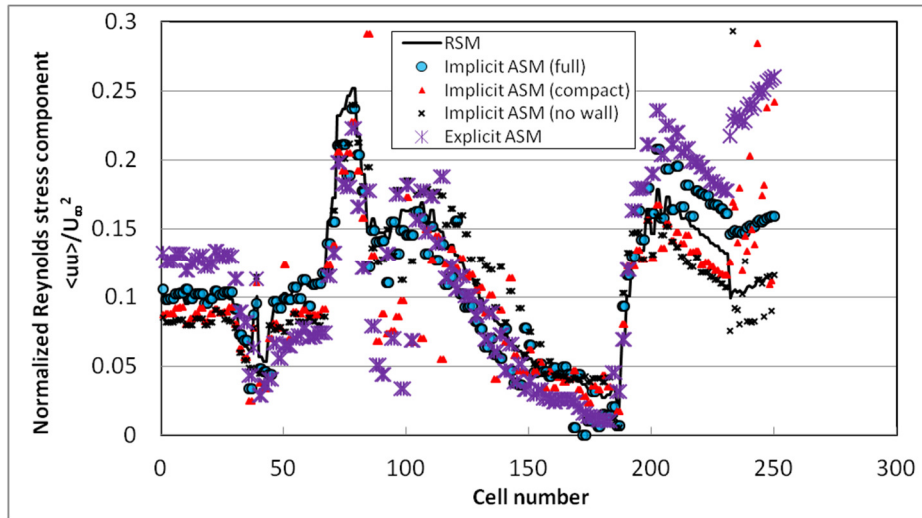


Figure 19 Distribution of the normalized Reynolds stress component $\langle uu \rangle$ around the blade at $z/L=0.5$, and $h/L=5e-6$ from RSM, three implicit, and one explicit ASM models

In the following figures, the ASM formulation is investigated at different locations of the computational domain, but still close to the blade wall. Figure 20 shows the same quantities at the same height along the blade, but further away from the solid wall, that is at $h \sim 1\text{mm}$ or $h/L \sim 5e-5$. For all of the Reynolds stress components, there exists an acceptable agreement between the RSM and full implicit ASM results in most of the data points considered. There exists small amount of data scatter for $\langle vv \rangle$ and $\langle vw \rangle$ components. On the other hand, the explicit model shows larger errors, although again the trends are fine, and data scatter is not significant, and all quantities show smooth behavior. These results are better than those depicted

in Figure 16, which could be caused by the less significant influence of the wall correction term on the positions further away from the blade wall.

Similarly, Figure 21 shows the distribution of all six Reynolds stress components at the same height but much closer to the blade wall, i.e., $h=5e-5$ m, or $h/L \sim 2.5e-6$. This test was run using the full implicit and explicit ASM models. It is evident that for four of the components, there is a very good agreement between RSM and implicit ASM results, while for $\langle vv \rangle$, ASM slightly overpredicts, and for $\langle vw \rangle$, ASM slightly underpredicts the RSM results. Unlike the implicit model, the explicit ASM formulation results in large deviation from RSM as well as some large data scatter. This means one has to be careful in the selection of the ASM models for the regions in the flow domain, extremely close to the solid wall. Besides the full implicit model used here, it might be worth examining different ASM formulations. That could be subject of a future study.

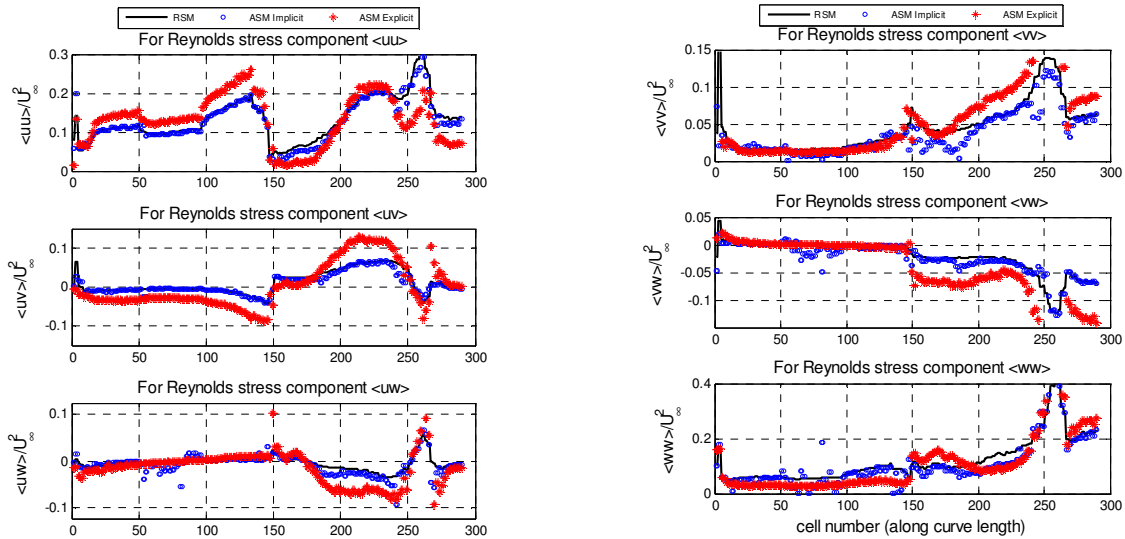


Figure 20 Distribution of the normalized Reynolds stresses around the blade at $z/L=0.5$, and $h/L=5e-5$ (explicit; and full $\Phi_{ij,2}$ form with wall effects)

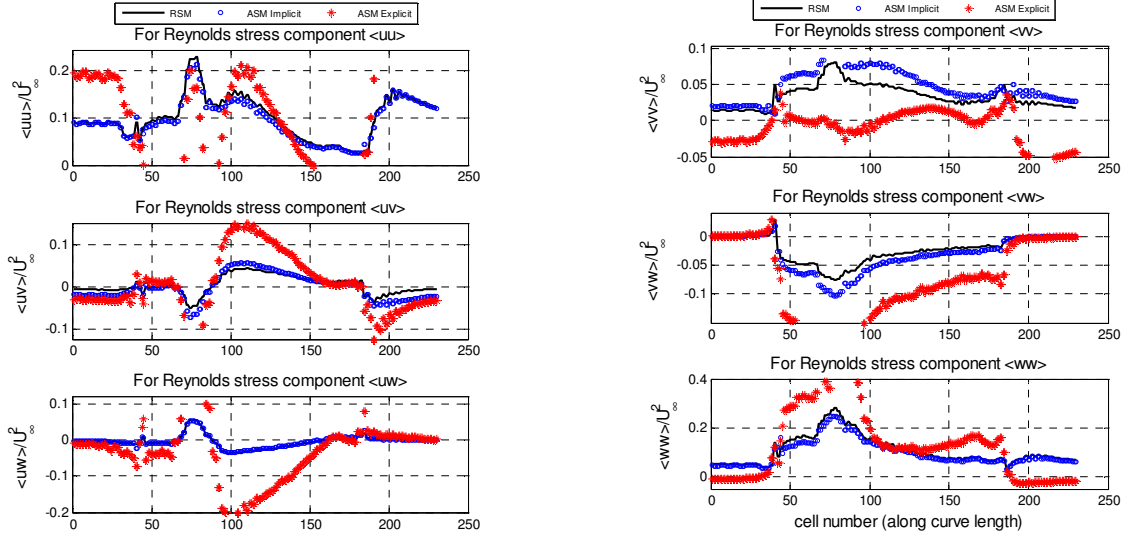


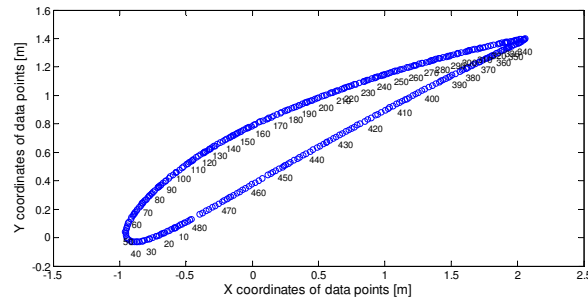
Figure 21 Distribution of the normalized Reynolds stresses around the blade at $z/L=0.5$, and $h/L=2.5e-6$ (explicit; and full $\Phi_{ij,2}$ form with wall effects)

In addition to the $z/L=0.5$ plane, the ASM formulation is examined at two other heights along the blade, i.e., at $z/L=0.25$, and $z/L=0.75$. The position of the elements in the computational domain chosen around the blade, as well as the results of the ASM analysis for those two cases (both with $h/L=5e-6$) are shown in Figure 22 and Figure 23. Notice the difference between the sizes of the two profiles in parts a of these two figures. Except for one Reynolds stress component, there is a decent agreement between RSM and ASM results in Figure 22. This could be because the flow domain considered in this figure is closer to the hub, and, therefore, the velocities and level of turbulence are lower, and the flow calculations are more reliable. The only region with significant discrepancies is near the trailing edge on the suction side, where the separation is likely to happen. On the other hand, Figure 23 shows the flow characteristics closer to the blade tip, where larger vortices and higher turbulence intensities exist, and the flow becomes less predictable. This may explain the discrepancy between the RSM and ASM results.

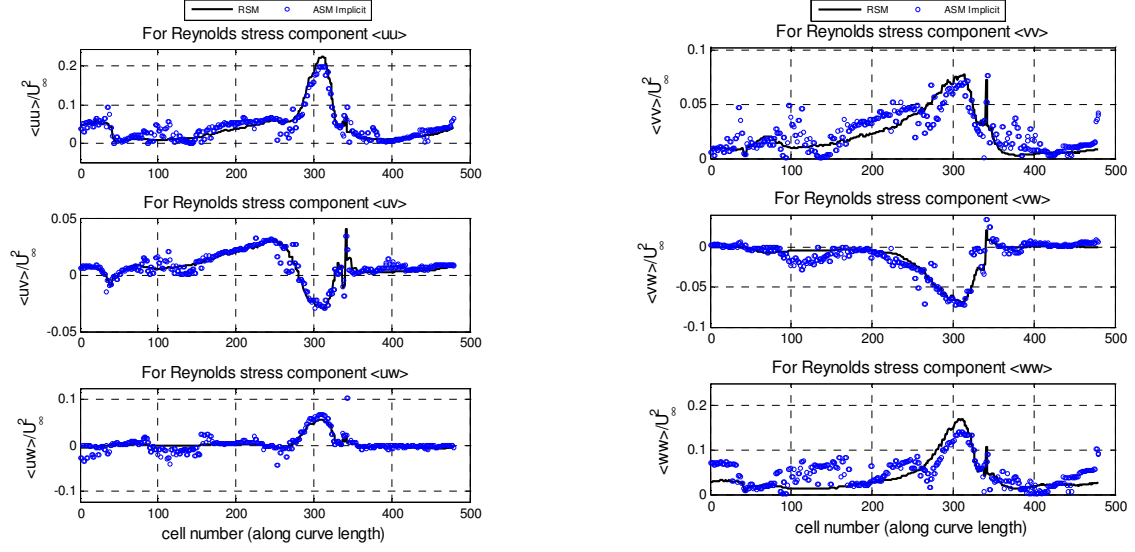
Finally, in addition to the $z/L=0.5$ plane, the ASM formulation is examined at two other heights along the blade, i.e., $z/L=0.25$, and $z/L=0.75$. The position of the elements in the

computational domain chosen around the blade, as well as the results of the ASM analysis for those two cases (both with $h/L=5e-6$), are shown in Figure 22 and Figure 23. Based on the fact that the explicit ASM did not show acceptable agreement with RSM, in the following figures, only the full implicit ASM model is investigated. Notice the difference between the size and shape of the two profiles in parts of those two figures.

Except for two of the Reynolds stress components, there is a good agreement between RSM and ASM results in Figure 22. This could be because the flow domain considered in Figure 22 is closer to the hub, and therefore, the velocities and level of turbulence are lower. In the central parts of the suction side, it is seen that $\langle vv \rangle$ and $\langle ww \rangle$ components fail to replicate RSMs that could be due to the separation effects. On the other hand, Figure 23 shows the flow characteristics closer to the blade tip, where larger vortices and higher turbulence intensities exist, and the flow becomes less predictable. This may explain the discrepancy between the RSM and ASM results. Even in this case, the only significant deviations are observed for $\langle vv \rangle$ and $\langle ww \rangle$ components, and the other components match well with RSM predictions.

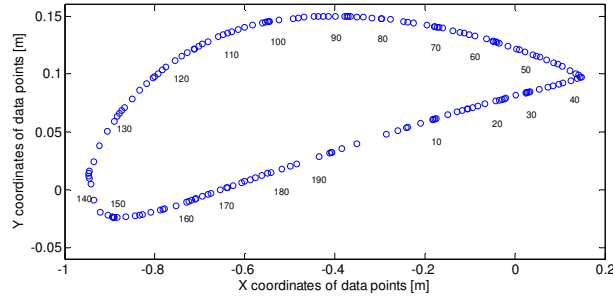


(a)

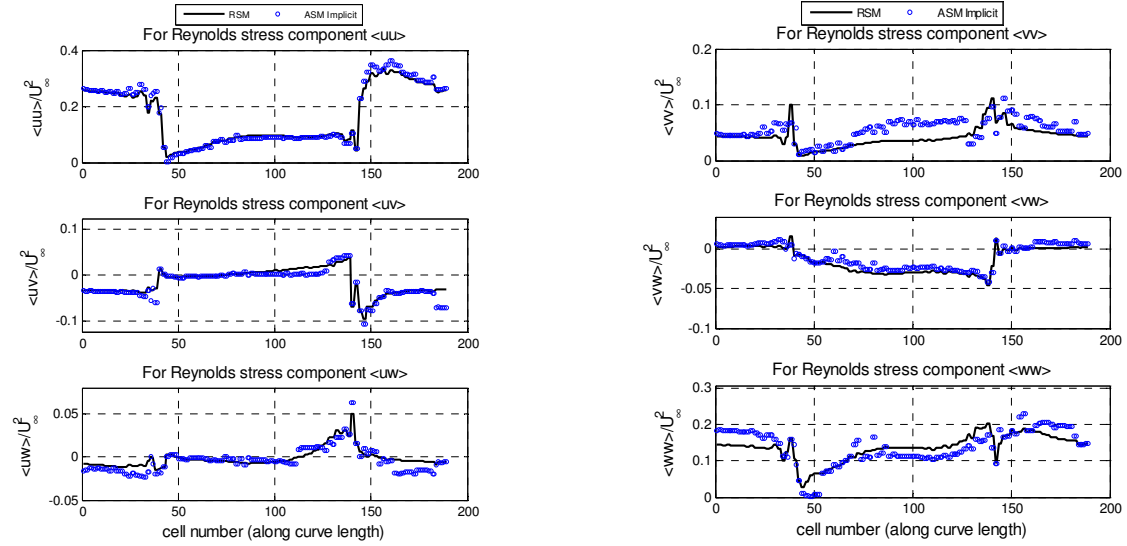


(b)

Figure 22 (a) Indices of grid points of interest, and (b) Distribution of the normalized Reynolds stresses, around the blade at $z/L=0.25$, and $h/L=5e-6$ (full $\Phi_{ij,2}$ form)



(a)



(b)

Figure 23 (a) Indices of grid points of interest, and (b) Distribution of the normalized Reynolds stresses, around the blade at $z/L=0.75$, and $h/L=5e-6$ (full $\Phi_{ij,2}$ form)

3.6 Conclusion

3.6.1 Flat Plate

The algebraic stress turbulence model is utilized in order to find the Reynolds stresses in the near-wall region for flow of air over a 2D flat plate. Three variations of implicit ASM, as well as one form of explicit ASM, are used to compare the models with fully-converged RSM from ANSYS Fluent. Reynolds stresses are obtained on a line normal to the plate, located in the turbulent region. The results are also compared against Klebanoff's experimental data. While Fluent RSM results are closer to the experimental values, it can be observed that for all four Reynolds stress components, the predictions of the full implicit ASM is acceptable. Except for the $\langle vv \rangle$ component, the full implicit ASM model gives relatively better results as compared to the compact ASM and the no-wall ASM models. This suggests that either the compact implicit ASM should not be used or the coefficient γ in Eq. (3.14) needs to be adjusted. Moreover, the No-wall implicit ASM model provides results that are very similar to those of the full implicit ASM model, except for $\langle uv \rangle$ term. The basic explicit ASM model used in this study seems to be less accurate than the full implicit model, except maybe for $\langle uu \rangle$ in the near-wall region. Based on the current results, and considering the significantly less computational time requirement of the ASM models compared to RSM, it seems that one can use full implicit ASM to improve the flow behavior within the boundary layer, without sacrificing the accuracy.

3.6.2 Wind Turbine Blade

Algebraic Stress Model was examined in the present work by investigating turbulent flow around a horizontal axis wind turbine blade. Three variations of the pressure-strain term (full $\Phi_{ij,2}$ with wall effects, compact $\Phi_{ij,2}$ with wall effects, and full $\Phi_{ij,2}$ without wall effects) were used along with an explicit ASM model, and the results were compared in terms of predictions of six Reynolds stress components at $z/L=0.5$ and at a region with the approximate wall distance h

of 0.1 mm, or $h/L=5e-6$. Overall, the full $\Phi_{ij,2}$ form with wall effects (full implicit model) showed better agreements with RSM data. The other three models considered showed more data scatter and larger discrepancies, among which the explicit ASM turned out to be the least accurate model.

Reynolds stresses were also plotted at $z/L=0.5$ and at two other concentric layers around the blade, i.e., further away from the wall ($h/L=5e-5$), and closer to the wall ($h/L=2.5e-6$). Moreover, they were investigated at two other heights along the blade, i.e., $z/L=0.25$ and $z/L=0.75$, both at $h/L=5e-6$. The full implicit model again showed much better agreement with RSM data and smoother behavior as compared to the explicit model. The full implicit model is recommended to be used in conjunction with LES or DES in future investigations for the improvement of flow predictions. The main conclusion of the present work is that without going through the RSM simulation, one can use simpler methods (such as ASM) to get reasonable values for Reynolds stresses, similar to those obtained from RSM. In the next step, the appropriate version of ASM will be utilized in a hybrid LES-RANS routine, to improve the prediction of the near-wall quantities.

Chapter 4 Hybrid DES-ASM Model

4.1 Introduction

In the previous chapter, feasibility of using ASM in lieu of the more complex turbulence model of RSM was studied. The idea is to develop a model that improves the near-wall predictions of LES by combining it with a RANS model. In the present chapter, DES is utilized as a readily coupled LES-RANS simulation method, and then some of the turbulence quantities such as the turbulent kinetic energy k and the specific dissipation rate ω are updated using an external ASM routine. The reliability of this method is investigated in the past for assessment of flow over a flat plate (Amano and Beyhaghi, 2015) and flow around a rotating wind turbine blade (Beyhaghi and Amano, 2015). It was concluded that the proposed ASM technique could replicate the results of an RSM simulation while using much less computational resources. Having confidence in the reliability of ASM, it is now desired to apply the same methodology to examine the improvements in predictions of near-wall flow behavior, such as pressure and velocity distribution, by using a coupled DES-ASM method for analysis of turbulent flow over an NACA 4412 airfoil. Airfoil geometry was selected so as to characterize the aerodynamic performance under different angles of attack (AoA). Moreover, the findings from the airfoil study can be later used on not only wind turbine blades, but also airfoils used for any other applications such as airplane wings or unmanned aerial vehicles (UAVs). Note the Reynolds number (Re) is kept constant at around $1.6\text{E}+6$ throughout this study, and AoAs 0 and 14 degrees are investigated. The computational results of different turbulence models are compared against published experimental data.

4.2 Theory

As mentioned earlier, DES is a hybrid modeling approach that combines certain features of RANS simulations with LES. DES turbulence models are set up so that boundary layers and irrotational flow regions are solved using a base RANS closure model. However, the turbulence model is intrinsically modified so that, if the grid is fine enough, it will emulate a basic LES subgrid-scale model in detached flow regions. In other words, the unsteady RANS models are employed in the near-wall regions, while the filtered versions of the same models are used in the regions away from the near-wall. In the current effort, Smagorinsky subgrid scale model is employed as the LES scheme. This method is described in much more details elsewhere (Smagorinsky, 1963; Deardorff, 1970). In the present work, the k- ω SST formulation is used as the underlying RANS model and is briefly discussed here. It is customized for operation along with DES.

The delay factor introduced in 2004 (Menter and Kuntz, 2004) has been adopted for the DES formulation of the k- ω SST model. This modification improves the capability of the model in terms of distinguishing between LES and RANS regions on computational meshes, where spatial refinement could give rise to ambiguous behavior. In addition, the improved delayed detached eddy simulation (IDDES) formulation (Shur et al., 2008) is utilized. This combines DDES with an improved LES-RANS hybrid model aimed at wall modeling in LES when the grid resolution supports it. In the next sub-sections, the baseline k- ω SST model is outlined, followed by the version of it that is customized for DES.

4.2.1 K-Omega SST Model

Turbulent Kinetic Energy

$$\frac{d}{dt} \int_V \rho k dV + \int_A \rho k (\mathbf{v} - \mathbf{v}_g) \cdot d\mathbf{a} = \int_A (\mu + \sigma_k \mu_t) \nabla k \cdot d\mathbf{a} + \int_V (\gamma_{eff} G_k - \gamma' \rho \beta^* f_{\beta^*} (\omega k - \omega_0 k_0) + S_k) dV \quad (4.1)$$

Specific Dissipation Rate

$$\frac{d}{dt} \int_V \rho \omega dV + \int_A \rho \omega (\mathbf{v} - \mathbf{v}_g) \cdot d\mathbf{a} = \int_A (\mu + \sigma_\omega \mu_t) \nabla \omega \cdot d\mathbf{a} + \int_V (G_\omega - \rho \beta f_\beta (\omega^2 - \omega_0^2) + D_\omega + S_\omega) dV \quad (4.2)$$

where k_0 and ω_0 are the ambient turbulence values in source terms (S_k and S_ω) that counteract turbulence decay, and γ_{eff} is the effective intermittency which is provided by the Gamma Re- θ transition model. For more information, refer to Star-CCM+ User Guide (CD-adapco, 2014).

4.2.2 DES Version of the K-Omega SST Model

the dissipation term in Eq. (4.1) is modified as (Menter and Kuntz, 2004):

$$D_k = \rho \beta^* f_{\beta^*} \omega k \phi \quad \phi = \begin{cases} 1 & \text{if } l_t < C_{des} \Delta \leftrightarrow \text{RANS mode} \\ > 1 & \text{if } l_t > C_{des} \Delta \leftrightarrow \text{LES mode} \end{cases} \quad (4.3)$$

where

$$\phi = \max \left[\frac{l_t}{C_{des} \Delta} F, 1 \right], \quad F = 1 - F_2, \quad l_t = \frac{\sqrt{k}}{\beta^* \omega} \quad (4.4)$$

In the equations above, Δ is the largest distance between the centers of the cell under consideration and the neighboring cells. Also, F_2 is the blending function as fully described elsewhere (CD-adapco, 2014). The model constant, C_{des} , blends the values obtained from independent calibration of the k - ϵ and k - ω branches of the k - ω SST model (Travin et al., 2002) and is evaluated as

$$C_{des} = C_{des,k-\omega} F_1 + C_{des,k-\epsilon} (1 - F_1) \quad (4.5)$$

where F_1 is defined in Star-CCM+ User Guide (CD-adapco, 2014). Finally note that the governing equations specific to ASM are presented in the previous chapter, and therefore are not repeated here.

4.3 Computational Setup

The computational modeling and analysis are carried out using the commercial computational fluid dynamics (CFD) package, Star-CCM+. The geometry is developed by importing a standard NACA 4412 airfoil profile in the software, extruding it to a proper span-wise length, creating the surrounding domain, and finally subtracting the airfoil from the surrounding domain. As for the computational grid, a fully structured body-fitted grid as recommended in previous efforts (Menter and Kuntz, 2004; Bose, 2012) was used.

Figure 24 depicts the geometry and the mesh configuration chosen for this study. A C-H-shape geometry is chosen as the computational domain. Air with the ambient pressure and temperature of 101.325 KPa and 300 K, respectively, is used as the working fluid. All the far-field boundaries are assigned free-stream boundary conditions, and all solid surfaces of the airfoil are given a no-slip wall condition. The free-stream velocity magnitude is set to 12 m/s, resulting in a chord-based Re of $1.6E+6$. The two side surfaces of the domain are assigned a periodic boundary condition. All simulations are run until a convergence criterion of $1E-6$ is achieved for all flow variables. For the unsteady DES simulations, the time step size of $13\ \mu s$ is chosen which results in a CFL (Courant–Friedrichs–Lewy) number of around 0.8. Also, only the implicit version of ASM is used as it has been shown elsewhere (Beyhaghi and Amano, 2015; Amano and Beyhaghi, 2015) that it has better agreement with RSM as far as the prediction of the Reynolds Stress components is concerned.

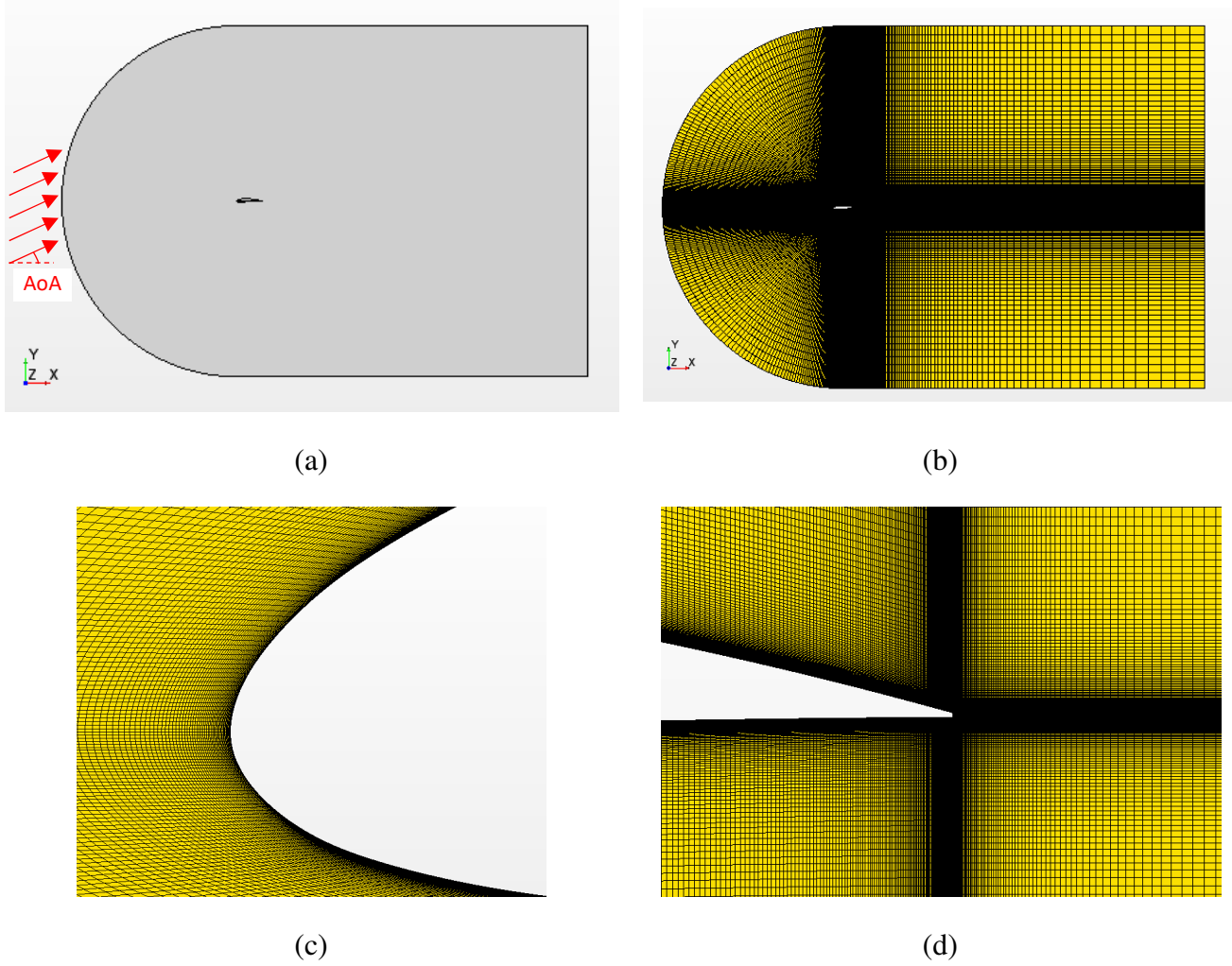
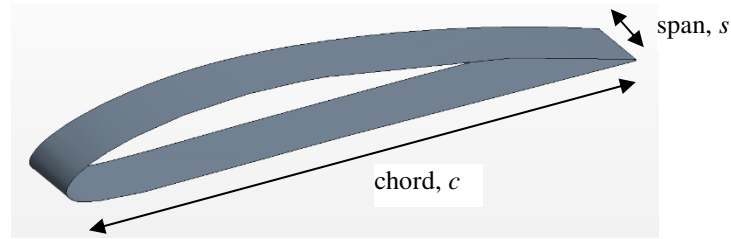


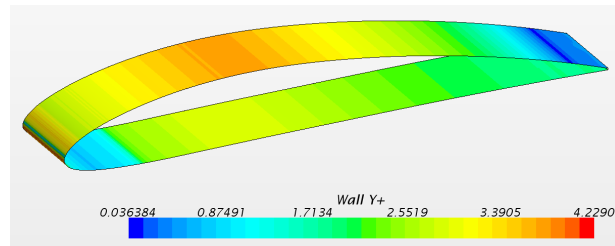
Figure 24 The computational domain and the mesh generated around a NACA 4412 airfoil: (a) geometry, (b) mesh around the airfoil, (c) mesh magnified near the leading edge, (d) mesh magnified near the trailing edge

In Figure 25, the NACA 4412 airfoil along with its main geometric parameters is shown. The chord and span lengths are set to 2 m and 0.2 m, respectively. Also shown is the distribution of the non-dimensional distance of the near-wall grid y^+ from the airfoil surface. The average y^+ is 2.41 after a converged DES solution. The final mesh count is 8.03M elements, which was determined after a mesh independence study. For an airfoil subjected to a free-stream velocity magnitude of 12 m/s and AoA of 0 degrees, three different meshes were generated, and simulations were run for each case until convergence. As displayed in Table 2, the lift and drag coefficients of the two finer cases (with the approximate element counts of 8M and 15M) are

very close, while those of the coarsest case show about 3-4% discrepancy. Therefore, it was decided to use the case with 8 million elements.



(a)



(b)

Figure 25 The airfoil considered for this study: (a) the geometry, (b) distribution of y^+ after a converged solution at $AoA=0^\circ$

Number of mesh elements	Lift Coefficient	Drag Coefficient
~ 3M	0.441	0.0111
~ 8M	0.423	0.0104
~ 15M	0.424	0.0105

Table 2 Mesh independence study in terms of lift and drag coefficients for an airfoil with incoming air velocity of 12 m/s and $AoA=0^\circ$

4.4 Numerical Procedure

The procedure for application of the hybrid DES-ASM model to flow over an airfoil is outlined below. The objective is to see whether the addition of the ASM treatment can improve the flow prediction as compared to what found from a baseline DES simulation.

(a) Solve the flow field and turbulence using the baseline DES.

- (b) Store the mean velocity gradients, k and ω only in the vicinity of the airfoil surface. To do so, first one needs to define a *derived plane* in Star-CCM+, to represent the locus of the grid points in the domain with the wall distance less than a certain small value. Then, create a *Table* (under *Tools*) that stores the quantities of interest at this derived plane, and then right-click on the Table, do *extract*, and finally *export* it to a spreadsheet-like file with .csv extension.
- (c) Import the aforementioned quantities in the external ASM routine developed in MATLAB and Octave.
- (d) Execute the ASM code to find the updated Reynolds stresses, and other quantities.
- (e) Import the updated quantities back in the main flow solver code and continue the DES simulation to reach another convergence point. To import, one needs to create a *File Table* (again, under *Tools*), and map the *Path* to the .csv file generated in step b.
- (f) After another converged simulation, calculate the quantities of interest and compare them against the results of the original DES and the published data from the literature.

4.5 Results and Discussions

In this section, contours of the pressure coefficient and chordwise velocity components are presented for the baseline DES model. Moreover, the DES and the proposed hybrid DES-ASM models are compared in terms of the pressure coefficient (for both low and high AoAs), and the near-trailing-edge velocity profiles (only for high AoA). Results of a well-known published experimental study (Wadcock, 1978) are used for validation of the pressure coefficients and trailing-edge velocity profiles obtained from CFD simulations of the airfoil. The reference above is used by many researchers for validation studies including NASA Langley Research Center for

validation of different turbulence models (Rumsey, 2014). The four near-trailing-edge locations and the mid-span airfoil surface are depicted in Figure 26.

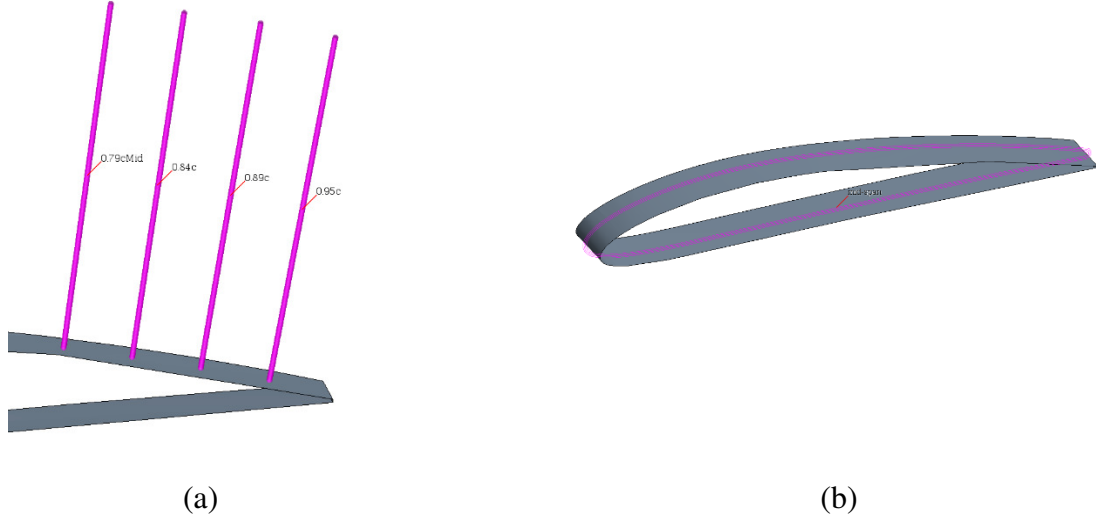


Figure 26 (a) The four near-trailing-edge lines normal to the airfoil surface, located at normalized chord-wise lengths x/c of 0.79, 0.84, 0.89, and 0.95; (b) airfoil surface mid-span where the pressure coefficient data is gathered from

4.5.1 Performance at $AoA=0^\circ$

Before presenting the results of different turbulence models on pressure coefficients, the distribution of the pressure coefficient and normalized velocity profile in the vicinity of the airfoil obtained from a baseline DES is presented here. As shown in Figure 27a, generation and decay of the eddy structures are apparent even at $AoA=0^\circ$.

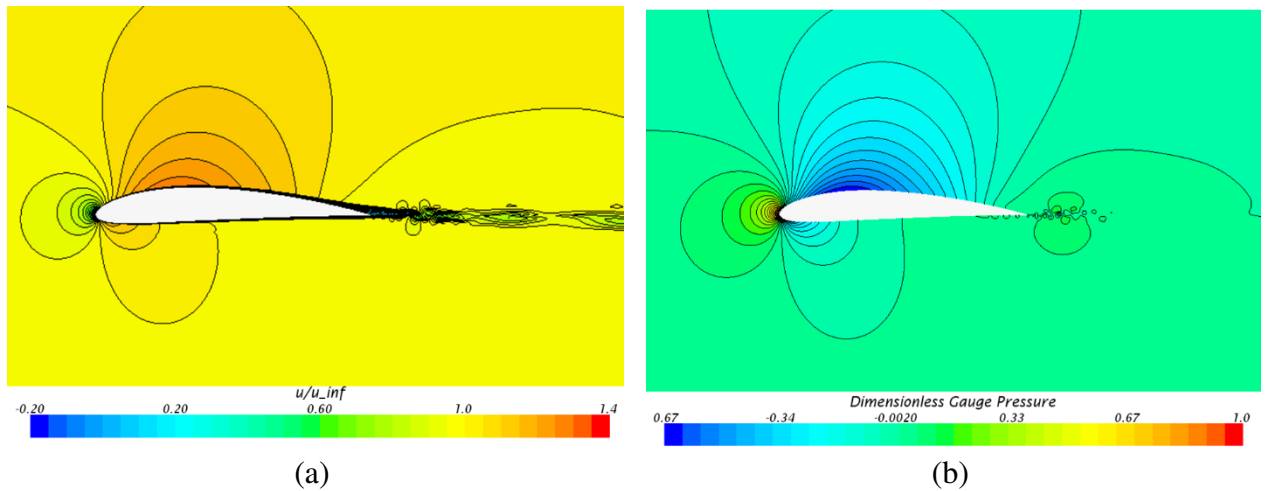


Figure 27 Distribution of (a) the normalized chord-wise velocity component, and (b) pressure coefficient in the mid-span plane, near the airfoil surface, for $AoA=0^\circ$, and $Re=1.6E+6$

Next, the pressure coefficient at the mid-span of the airfoil surface is calculated from different turbulence models, and the results are presented in Figure 28. It is observed that at $AoA=0^\circ$, DES and DES-ASM yield nearly identical results near the leading edge of the airfoil on both suction and pressure sides (part b). In the mid-chord region (part c), however, it seems that the hybrid model can improve DES predictions, especially in the pressure-side, where there is a good agreement between the hybrid model and the experimental data. As shown in part d, the hybrid model can improve DES prediction near the trailing edge, while both models show some discrepancy with the experimental predictions.

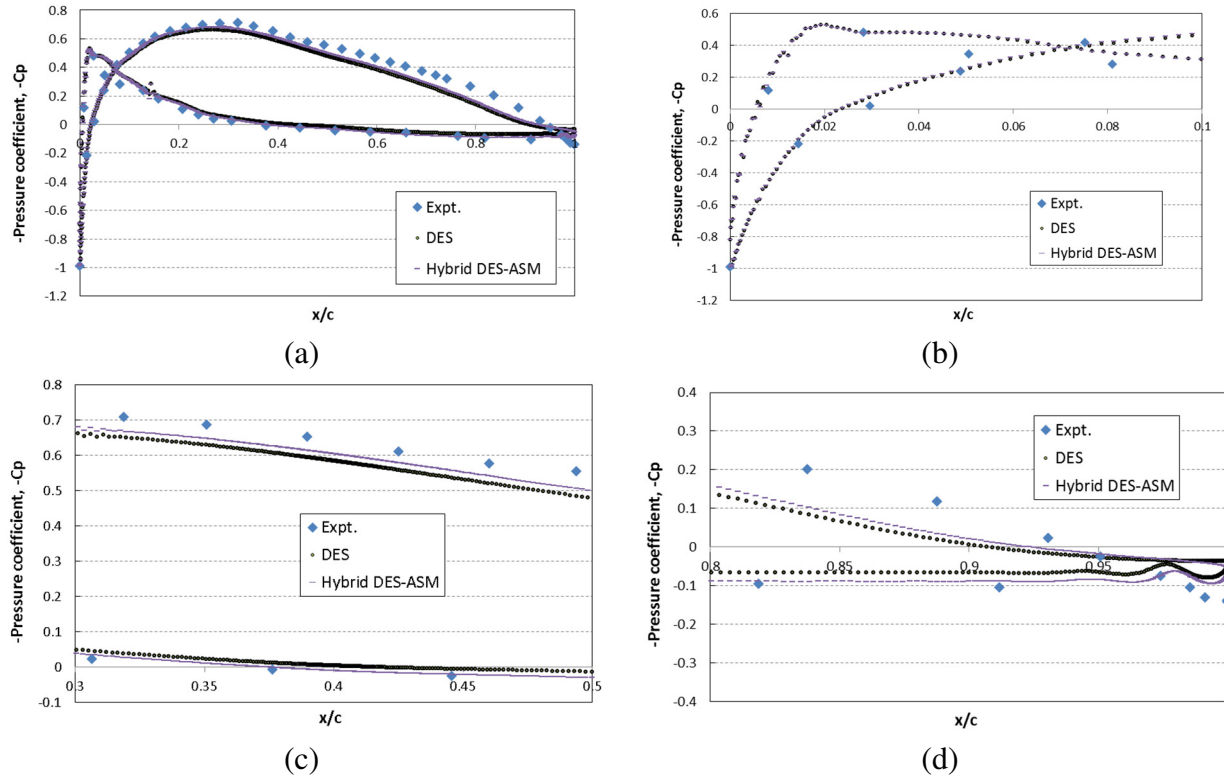


Figure 28 Distribution of the pressure coefficient with negative sign at $AoA=0^\circ$ at the mid-span of the airfoil surface, determined from different turbulence models and the published experimental data: (a) the entire curve, (b) near the leading-edge, (c) in the mid-chord, and (d) near the trailing-edge

4.5.2 Performance at $AoA=14^\circ$

The distribution of pressure coefficient and a normalized chordwise velocity component in the vicinity of the airfoil obtained from a baseline DES is presented in Figure 29. Vortical structures are present near and downstream of the trailing edge. Also, larger velocity values as compared to the $AoA=0^\circ$ case are observed.

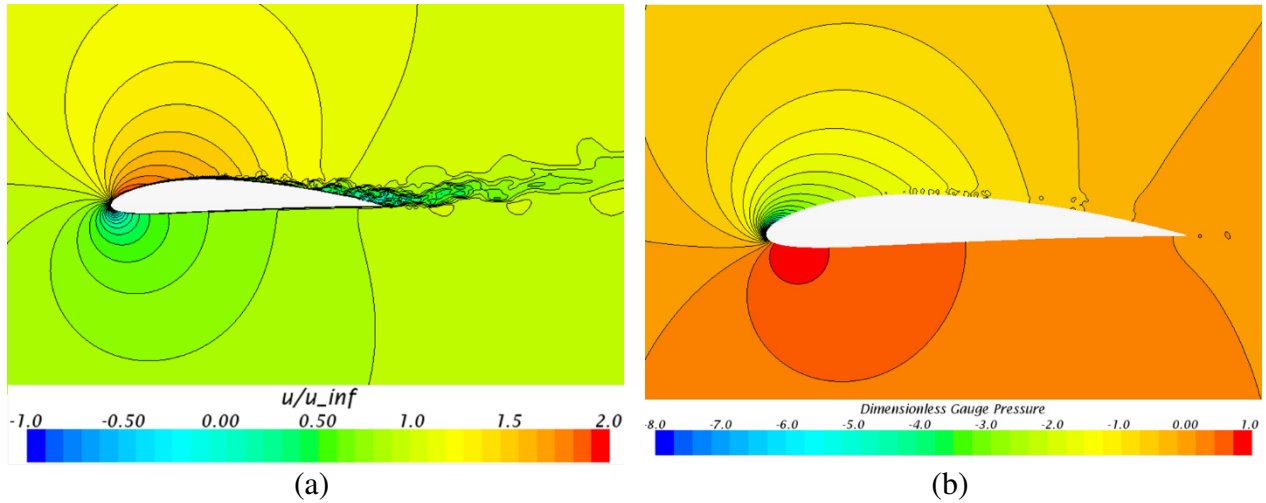


Figure 29 Distribution of (a) the normalized chord-wise velocity component, and (b) pressure coefficient in the mid-span plane, near the airfoil surface, for $AoA=14^\circ$, and $Re=1.6E+6$

The distribution of the pressure coefficient at the mid-span of the airfoil surface is depicted in Figure 30. The overall behavior of the hybrid DES-ASM model is similar to the DES model nearly everywhere, and this is true especially near the leading edge. However, in the mid-chord region and near the trailing edge, the hybrid model slightly overpredicts the baseline DES model. Even though both models show some discrepancy with respect to the experimental data, it seems that the hybrid model results in better predictions of pressure coefficients near the trailing edge. Note that the overall discrepancy could be in part due to the inaccuracies in the experimental data, including the wind-tunnel blockage effect, and uncertainties in the reading of the hot-wire sensors used in the cited experimental research.

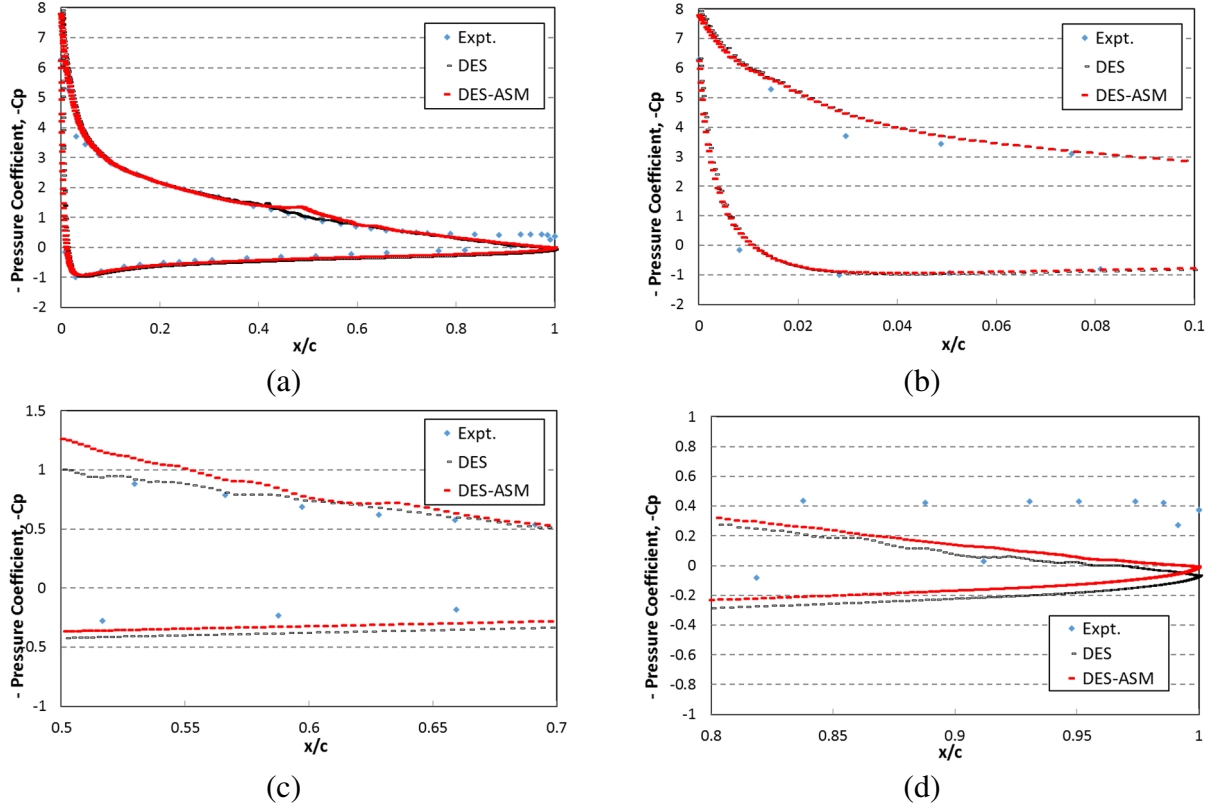
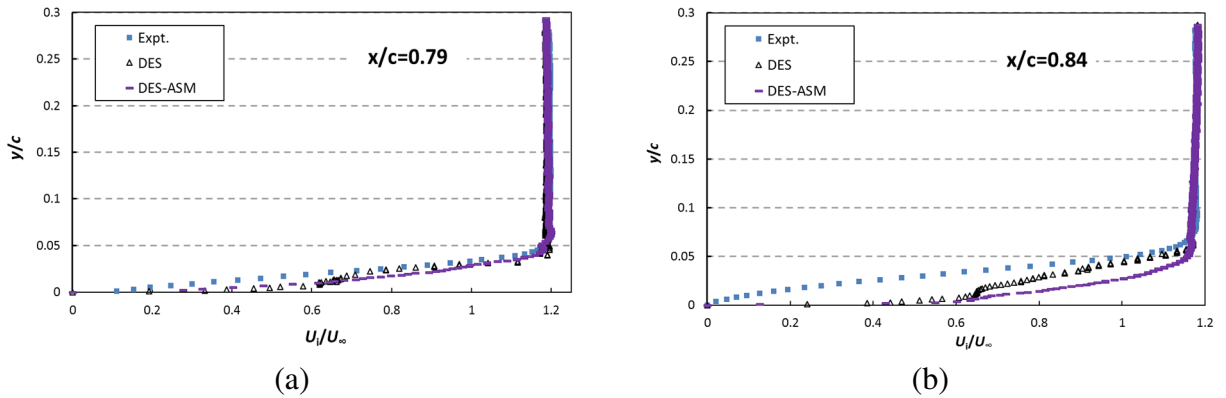


Figure 30 Distribution of the pressure coefficient with negative sign at $AoA=14^\circ$ at the mid-span of the airfoil surface, determined from different turbulence models and the published experimental data: (a) the entire curve, (b) near the leading-edge, and (c) near the trailing-edge

To better quantify the performance of the turbulence models in a separated flow regime, the distribution of the normalized chordwise velocity component near the trailing edge is demonstrated in Figure 31, where the velocity profiles are compared with those found from the literature (Wadcock, 1978).



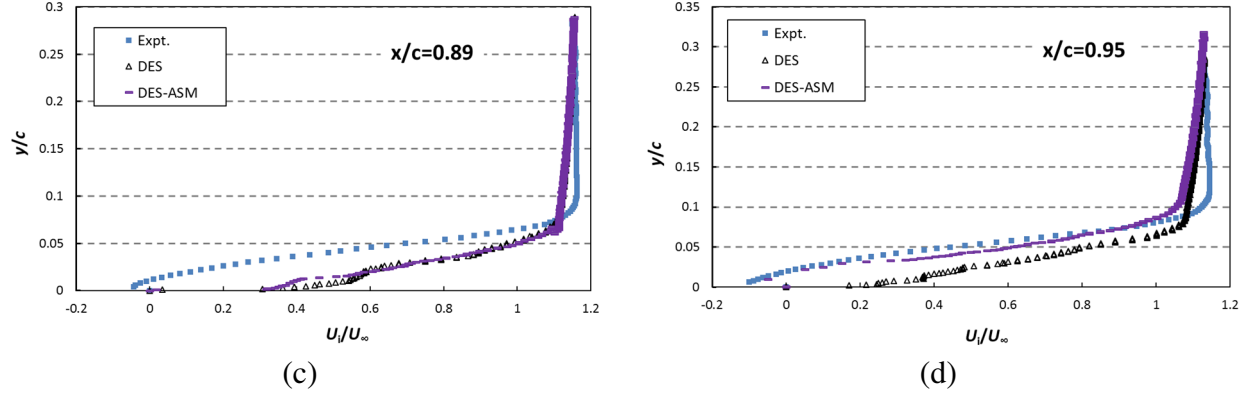


Figure 31 Velocity profiles for $AoA=14^\circ$ case obtained from two different turbulence models and the experimental data, at four normalized chord-wise locations x/c : 0.79, 0.84, 0.89, and 0.95

At $x/c=0.79$, the general agreement between the experimental results and the two turbulence models is acceptable in the near-wall region, although both DES and hybrid DES-ASM slightly underpredict the velocities in the lower half of the boundary layer. Also, very close to the airfoil surface, the hybrid DES-ASM results are better than those of DES, which justifies application of this new model. At $x/c=0.84$, the two models agree with experimental data reasonably well close to the edge and above the boundary layer. However, in the near-wall region, both DES and hybrid DES-ASM underpredict the velocities. The baseline DES predictions are better than those of the hybrid model.

At $x/c=0.89$, again both models underpredict the velocities, while their values are nearly identical, maybe except for the region very close to the airfoil surface. Within this region ($y/c < 0.025$), DES-ASM behaves better than DES. Finally, at a location very close to the airfoil trailing edge, $x/c=0.95$, one can see that the hybrid DES-ASM model shows better agreement with the experiment as compared to the baseline DES model, in almost the entire boundary layer. Only near the boundary layer edge and beyond that, DES slightly outperforms the hybrid model. These results again confirm that in certain locations in the vicinity of the solid surface, there is a potential for improving the flow predictions of a DES turbulence model by implementing an external ASM routine. In terms of the computational cost, the DES simulation took about 13

days on a cluster of 96 CPU cores. For the hybrid DES-ASM simulation, the process of exporting DES results from Star-CCM+ into the ASM code, solving the linear system of equations, substituting the results into the DES model, and rerunning the simulation led to an additional 10 hours.

4.5.3 Force Coefficients

The coefficients of lift and drag are two integral quantities that are typically used for evaluating the overall aerodynamic performance of airfoils. Pressure distribution over the airfoil surface and the velocity profiles are more detailed metrics for comparison of different turbulence models, and that is why they are chosen in the current study. However, to give some insight into the overall performance, the lift and drag coefficients of NACA 4412 at AoA of 14° are calculated from DES and DES-ASM turbulence models and presented in Figure 32. Same coefficients are determined experimentally (Wadcock, 1978), and are used for comparison. Note there is only a very small discrepancy between all the models, and the results of DES-ASM model are slightly closer to the experimental data compared to the DES model.

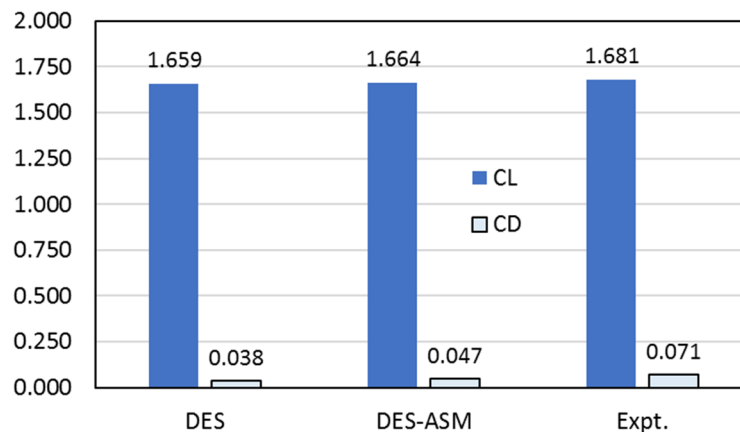


Figure 32 Lift and drag coefficients obtained for the angle of attack of 14 degrees from DES and DES-ASM turbulence models and an experimental set of data from the literature

4.6 Summary and Conclusions

The feasibility of improving the near-wall predictions of the DES turbulence model was studied in the present work. For this purpose, the subsonic flow of air over an NACA 4412 airfoil was investigated numerically using the commercial package, Star-CCM+. Two distinct values of the angle of attack (AoA) were chosen in order to examine the flow in both attached and separated regimes. The k - ω SST model was used as the underlying RANS model integrated with DES. Both k and ω quantities obtained from DES were updated by an ASM algorithm developed in an external Octave routine. The updated quantities were then imported back into the main solver code, where the simulation was allowed to run further and reach another convergence. The behavior of the original DES and the hybrid DES-ASM were compared against a set of experimental data in terms of the airfoil surface pressure coefficient and velocity profiles near the trailing edge.

At zero degree AoA, the pressure coefficients were obtained, and it was noticed that both turbulence models are capable of reproducing the experimental data. A closer look at the two edges of the airfoil revealed that the proposed hybrid model is either similar to or better than the baseline DES, although one can still detect some discrepancies with respect to the experimental data. No velocity data was available at this AoA for comparison purposes.

At a near-stall AoA ($\sim 14^\circ$), a similar pressure distribution was observed. In the mid-chord and near the trailing edge, both models showed some error, and the hybrid DES-ASM was slightly better than the baseline DES. Furthermore, the distribution of the chordwise velocity component near the trailing edge revealed that at certain locations near the trailing edge and within the boundary layer, it is possible to improve DES flow predictions by implementing an external ASM routine. Finally note that the disagreement with the experimental data could be in

part due to the uncertainties in the experimental measurements or wind tunnel blockage effect, among other possible reasons.

Chapter 5 Slotted Airfoil Parametric Study

5.1 Introduction

Although horizontal-axis wind turbines (HAWTs) have proven to be very useful for generating electrical energy, they suffer from some limitations, such as the Betz limit, which confines the efficiency of turbines to around 59% (Burton et al., 2011). A great deal of research has been aimed at finding ways to increase the power generation from turbines, by either modifying the airfoil shape or installing add-on features at certain span-wise and chord-wise locations of the blades. The objective of those alterations is to change the flow pattern around the airfoil so as to decrease drag and increase lift, and ultimately increase the overall power generation. Some of those devices commonly used are suction-side mini-tabs (Heathcote et al., 2016), riblets, vortex generators (VGs), serrated trailing edge (Arce et al., 2015), gurney flaps (van Dam et al., 1999), and slats (Schramm et al., 2016). Some of the important concerning issues for such additions are ease of manufacturing and installation, durability, drag penalty, and additional fatigue loads.

While active flow control using suction and injections streams are in use, the possibility of using slots for passive flow control is rarely investigated. One application of slots on airfoils is using leading-edge root extension (LERX) devices that are deployed in some modern fighter aircraft. LERX is a small fillet that runs forward from the leading edge of the wing. It can generate stream-wise vortices that adhere to the top wing surface, and therefore, prevent the boundary layer separation and maintain the lift force at high values at high angles of attack. This method can also be applied to wind turbines. In fact, some variations of it have been deployed by installing suction holes near leading or trailing edge of the airfoil, in order to remove the low-

momentum layers of the flow from the bottom of the boundary layer and therefore, delay the separation (Wang and Sun, 2000; Whitman et al., 2006; Johnson et al., 2008; Prince et al., 2017). Some of the other similar work on the application of *upward* slot (meaning the slot exit is located on the top surface of the airfoil) is briefly reviewed here.

Upward slot is investigated for flow separation control of S809 airfoil (Xie et al., 2013). The concept of split blade was used and flow behavior was studied both computationally and experimentally for AoAs of 0, 10, 15, and 20 degrees. Both analyses were conducted at $Re=1.0E5$. The inlet plane of the slot was located at 30% of the chord on the pressure side, and the exit plane was at 60% of the chord on the suction side. The CFD analysis was done under steady state with $k-\omega$ SST turbulence model. The results indicated that the separation area increases as AoA increases, and there exists a large separation area on the airfoil suction side at higher AoAs, which may not be favorable. The lift and drag coefficient did not change much at AoAs of 0 and 10 degrees, while they showed slight increase (in C_L) and decrease (in C_D) at AoAs of 15 and 20 deg.

A similar leading-edge slot with an upward direction was studied in another effort (Weber, 2012). A passively oscillating flap was devised towards the end of the slot, which could help with the flow behavior, by mixing the low-momentum fluid (flowing on the suction side) with a high momentum fluid (discharging from the slot), and thereby, energizing the near-blade flow. The chord-wise length of the slot was quite low (only about $0.11c$) and the width was kept constant at $0.02c$. In this fully-experimental study, the wind tunnel test-section flow velocity was maintained at 20 m/s, resulting in a chord-based Reynolds number of $3.0E5$. The airfoil used was NACA 0015 made of a polystyrene foam core with a fiberglass layup. For a condition where an additional airfoil was placed upstream (to create additional turbulence), the results showed that a

C_L increase of up to 10% could be achieved. No analysis was done on drag coefficient, but it was mentioned that “*generally the addition of a leading-edge slot contributes to increased airfoil drag*”.

In another effort, the near-stall behavior of a wind turbine airfoil equipped with an upward slot was investigated in a 2D computational study (Belamadi et al., 2016). The S809 profile was chosen as the airfoil, and the effects of slot’s location, width and slope were determined. C_L , C_D , and lift-over-drag ratio were compared for the different configurations. It was concluded that the implemented slot could improve the aerodynamic performance only over a very specific range of AoA. For some cases, especially at lower AoAs, a very large drag penalty was observed. At moderate and high AoAs ($\sim 14^\circ$ - 20°), the slot configuration outperformed the baseline configuration. Therefore, extra care should be taken before application of this slot on wind turbine blades. In particular, one needs to determine the effective AoA of the wind turbine blade to see if the slot could provide any benefit.

The new flow control method discussed in the present work is different than the conventional leading-edge blowing technique, in that the slot exit is located at the bottom surface of the airfoil in the presently investigated cases. Therefore, air flowing through the slot is forced to leave from the pressure side, meaning the flow direction is opposite of what is traditionally seen. The possibility of using leading-edge slots for horizontal axis wind turbines has been investigated very rarely. Turbulent flow over a slotted NREL (airfoil S883) blade was studied recently (Subash et al., 2014). They showed only qualitatively that employing slots could alter the pressure distribution above and below the airfoil. There were no quantitative results presented.

In another effort (Noorazyze, 2014), a 5 m wind turbine blade with NACA 4412 airfoil with and without slots was modeled. Slots in both horizontal (parallel to the blade axis) and vertical (perpendicular to blade axes; parallel to the main flow direction) configurations were tested. Unfortunately, the results were removed from that report and were not available. It was concluded that the aerodynamic results showed an increased value of lift coefficient at certain AoAs.

In a more recent study (Rong et al., 2015), the blade of G4-73No.8D centrifugal fan was equipped with a similar leading-edge slot. Aerodynamic performance of the blade was studied only computationally at a very large negative AoA, which would be the proper AoA for the operation of such centrifugal fan blades. The results indicated that having a slot could control the stall of centrifugal fan blade, and under appropriate operating conditions, lift improvement could be achieved. Steady-state analysis based on the SIMPLE algorithm and with $k-\omega$ turbulence model was carried out. Only one slot configuration was used, where the slot inlet and exit planes were located at 2% and 70% of the chord length on the pressure-side of the airfoil, respectively. Velocity contours and streamlines near the airfoils with and without the slot were displayed. It was shown that by using slots, the separation regions were reduced and airfoil surface flow field became more uniform. No data on the influence of such slots on the coefficients of lift and drag were presented.

In two recent studies at the University of Wisconsin-Milwaukee (UWM), wind turbine blades with leading-edge slots have been tested experimentally. The purpose of using slotted blades was to redirect some of the air flows through the blade, and later mix it with the air stream flowing along the bottom surface of the airfoil (Ibrahim et al., 2015; Alsultan, 2015). Figure 33 shows a small slotted wind turbine blade. NACA 4412 airfoil profile was used throughout the blade span

due to its high lift to drag ratio. This blade was designed using the CAD software package, Pro/Engineer, then 3D-printed and tested at the UWM Wind Tunnel Laboratory. More detail on the experimental facilities and procedure can be found elsewhere (Alsultan, 2015).



Figure 33 The slotted wind turbine blade fabricated and tested at UWM Wind tunnel

The performance of the slotted blade was examined experimentally in very limited operating conditions. This blade has shown to generate up to 26% more power than the standard blade for incoming air speed between 4.5 and 7.7 m/s, and the corresponding tip-speed ratio TSR (defined as $\Omega r/U_\infty$, where r is the blade length in m, and Ω shows the angular velocity in rad/s) increasing linearly from 4.8 to 6.2. No data was, however, reported beyond these ranges. Therefore, there is a need for further characterization of such slots under various operating conditions.

The objective of the present study is to build upon the previous results and carry out a rigorous parametric study on some of the design parameters. The focus is on airfoils, as opposed to blades, because it allows us to characterize the performance under different local angles of attack (AoA). Moreover, the findings can be used on not only wind turbine blades, but also airfoils utilized for any other applications such as airplane wings or unmanned aerial vehicles (UAVs). Note the chord-based Reynolds number (Re) is kept constant at $\sim 1.6E+6$ throughout this study, and AoAs between 0 and 16 degrees (slightly post-stall condition) with 2° increments

are selected for this investigation. The computational results of a standard solid airfoil are compared against the experimental data from the literature, while the results of a slotted airfoil are validated with those obtained from a series of wind-tunnel test at UWM. Aerodynamic performance at different Reynolds number is also studied.

5.2 Theory

To model the turbulent air flow around and through the slotted airfoil, the Reynolds Average Navier-Stokes (RANS) model of k - ω SST is used. This model is computationally more affordable than higher-end techniques such as Large Eddy Simulation (LES) and has gained a lot of attraction among the RANS models. This model is suitable for inner and outer parts of the boundary layer, as well as outside the boundary layer. The shear stress transport (SST) formulation switches to a k - ϵ behavior in the free-stream and therefore, it avoids the common problem often seen with the standard k - ω , which is being too sensitive to the inlet turbulence properties. The governing equations unique to this turbulence model are outlined in Eqs. (5.1 - 5.4). More details including the closure coefficients relevant to this model can be found in (Menter, 1994).

Reynolds Stresses

$$-\rho \langle u_i u_j \rangle = \mu_t \left(\frac{\partial U_i}{\partial x_j} + \frac{\partial U_j}{\partial x_i} - \frac{2}{3} \frac{\partial U_k}{\partial x_k} \delta_{ij} \right) - \frac{2}{3} \rho k \delta_{ij} \quad (5.1)$$

Turbulent Eddy Viscosity

$$\mu_t = \rho \nu_t = \frac{\rho a_1 k}{\max(a_1 \omega, W F_2)} \quad , \quad \text{where } W = \sqrt{2 W_{ij} W_{ji}} \quad , \quad W_{ij} = \frac{1}{2} \left(\frac{\partial U_i}{\partial x_j} - \frac{\partial U_j}{\partial x_i} \right) \quad (5.2)$$

Turbulent Kinetic Energy

$$\frac{\partial k}{\partial t} + U_j \frac{\partial k}{\partial x_j} = P_k - \beta^* k \omega + \frac{\partial}{\partial x_j} \left[(\nu + \sigma_k \nu_t) \frac{\partial k}{\partial x_j} \right] \quad (5.3)$$

Specific Dissipation Rate

$$\frac{\partial \omega}{\partial t} + U_j \frac{\partial \omega}{\partial x_j} = \frac{\gamma}{\mu_t} P_k - \beta \omega^2 + \frac{\partial}{\partial x_j} \left[\left(\nu + \sigma_\omega \nu_t \right) \frac{\partial \omega}{\partial x_j} \right] + 2(1 - F_1) \frac{\sigma_{\omega 2}}{\omega} \frac{\partial k}{\partial x_i} \frac{\partial \omega}{\partial x_i} \quad (5.4)$$

5.3 Computational Setup

The computational modeling and analysis are carried out using the commercial computational fluid dynamics (CFD) package, Star-CCM+. The geometry is developed by importing a standard NACA 4412 airfoil profile in the software, cutting the slot through the airfoil, extruding it to a proper span-wise length, and finally creating the surrounding domain and subtracting the slotted airfoil from it. As for the computational grid, several meshing schemes were examined, including a structured (*Trimmer*) grid, polyhedral mesh, and a fully-structured body-fitted mesh. After an extensive investigation, it was determined that the polyhedral mesh is a good trade-off between the accuracy and the computational cost. The polyhedral mesh was augmented with 16-18 prism (inflation) layers near the airfoil surface to deliver the proper grid resolution for wall y^+ requirements of the $k-\omega$ turbulence model.

For one of the slotted airfoils studied, a grid independence study was carried out to find the proper values of the mesh setting parameters. For that particular case, three different grids with 210K, 560K, and 950K polyhedral elements were generated, and the flow was solved for each case to find the lift and drag coefficients. As shown in Table 3, the case with 560K elements resulted in very similar force coefficients as the finest case, whereas both lift and drag of the coarsest case were roughly 3% different than the other two. Since the objective of the present work is to find an optimal design based on C_L and C_D values, even a few percent difference is considered significant, and can make a difference. Based on the observed values for lift and drag coefficients of the three cases considered, the mesh setting parameters of the case with 560K

elements is used for the remainder of this research. Note that the actual element count of the individual cases is highly dependent on the slot's parameters, mainly its width and length.

Number of mesh elements	Lift Coefficient	Drag Coefficient
210,000	0.4503	0.0233
560,000	0.4678	0.0242
950,000	0.4673	0.0242

Table 3 Mesh independence study in terms of lift and drag coefficients for a slotted airfoil with $L_l/c=45\%$, $w/c=2\%$, $\beta_1=0^\circ$, and $\beta_2=80^\circ$ at $AoA=0^\circ$

A coupled pressure-based flow solver with the second-order discretization and the CFL number of 5 was used for simulations, and the under-relaxation factor of 0.8 was assigned for k - ω turbulence. Air with constant properties at $T=300$ K and $P=101$ KPa was modeled in all simulations. Figure 34 depicts the geometry and the mesh configuration chosen for this study. A C-H-shape geometry of grids is selected as the computational domain. All the far-field boundaries are assigned free-stream boundary conditions, and all solid surfaces of the airfoil are given a no-slip wall condition. The free-stream velocity magnitude U is set to 24 m/s, resulting in a chord-based Re of $1.6E+6$. The two side surfaces of the domain are assigned a periodic boundary condition. All simulations are run until a convergence criterion of $1e-6$ is achieved for all flow quantities. More details on the setup can be found elsewhere (Beyhaghi and Amano, 2017a; Beyhaghi and Amano, 2017b). In Figure 35, a typical slotted airfoil along with the main geometric parameters of interest is shown. The widths of the first and second legs of the slot are set equal throughout this study. The chord and span lengths are set to 1 m and 0.2 m, respectively. The variable h indicates the vertical (normal to chord) distance between the “lower lip” of the slot (bottom-edge of slot's inlet plane) and a fixed point within the airfoil (shown as a yellow dot, which is $0.4c$ downstream and $0.04c$ above the leading edge).

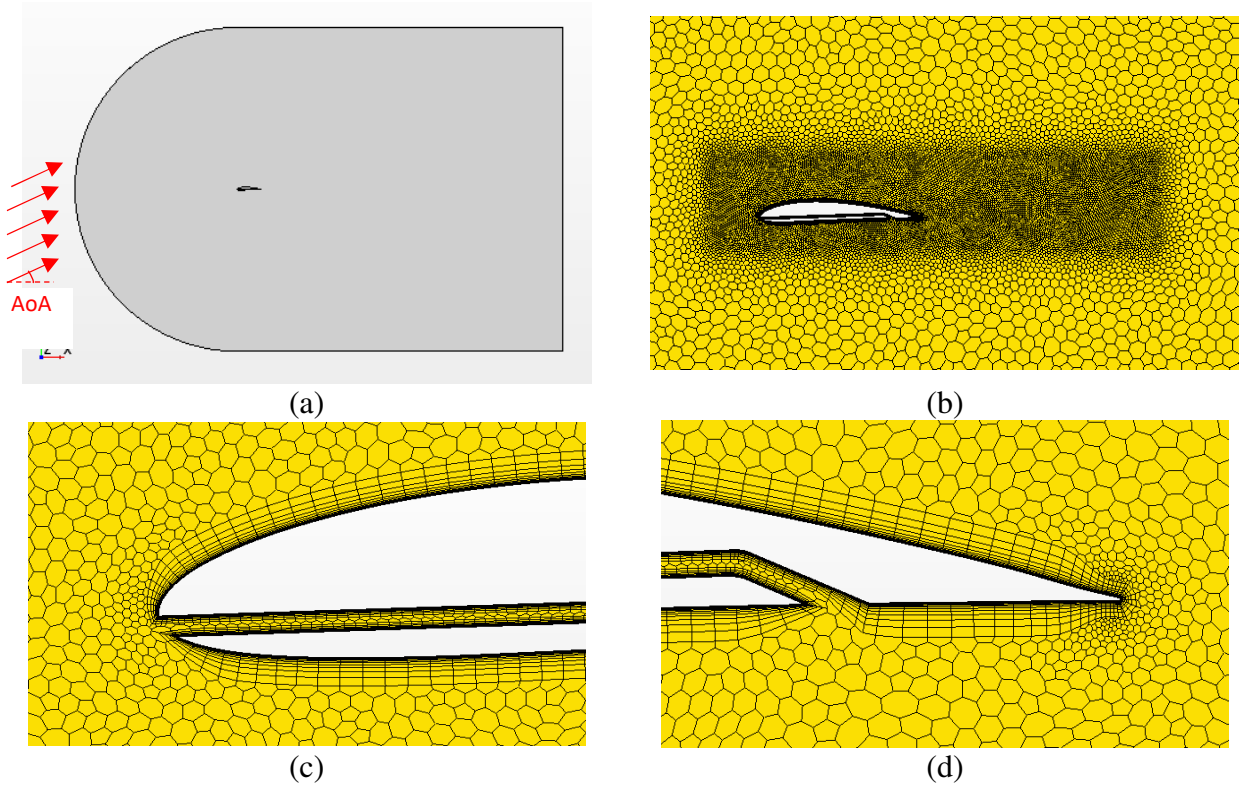


Figure 34 The computational domain and the mesh generated around a typical slotted airfoil: (a) geometry, (b) mesh around the airfoil, (c) mesh magnified near the leading edge and slot, (d) mesh near the trailing edge

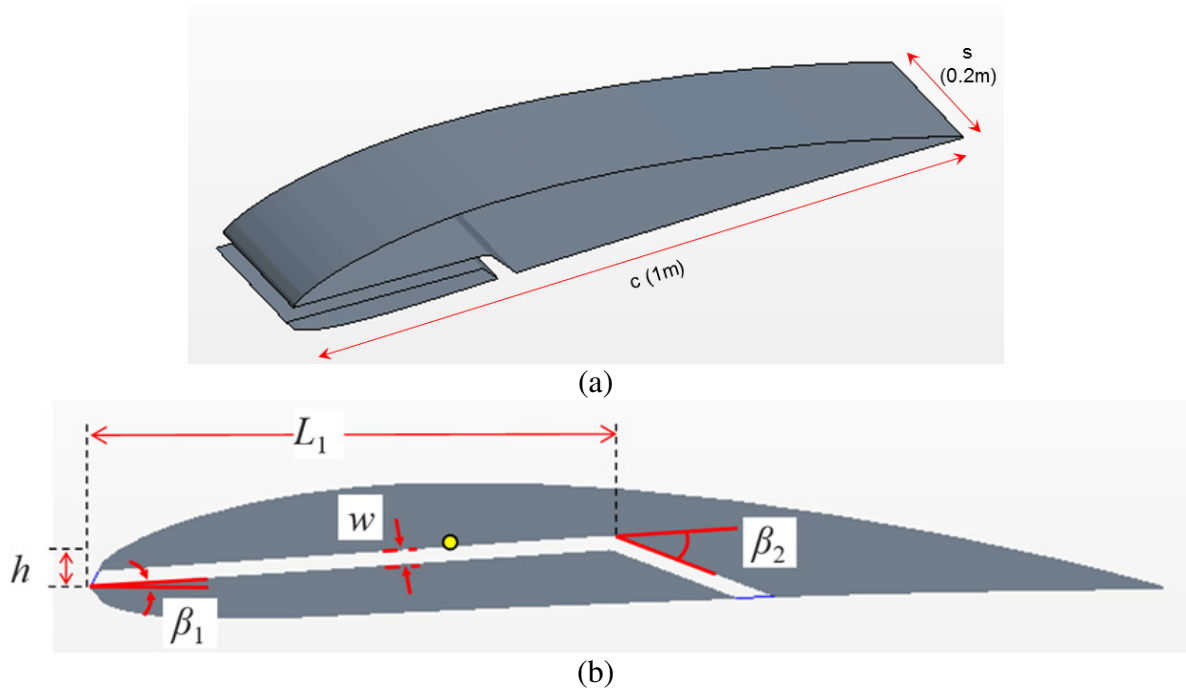


Figure 35 (a) a typical picture of a slotted airfoil considered for this study, (b) cross-section of a slotted airfoil with five main geometric parameters shown

5.4 Initial Validation

Results of the initial validation cases for both solid and slotted airfoils are presented in this section.

5.4.1 Literature Data – Solid Airfoil

Results of three published experiments are used for validation of the lift and drag coefficients obtained from CFD simulations of the solid airfoil (Figure 36). The agreement between the CFD results and Wadcock's data (Wadcock, 1978) – both with $Re=1.6E6$ - is very good at all the AoAs considered. For the sake of completeness, C_L and C_D values of the CFD simulation are also compared against the experimental data obtained from the references (Hastings and Williams, 1984) with $Re=4.1E6$, and (Abbott et al., 1945) with $Re=3.0E6$. One can note despite the small difference between the Reynolds numbers, there exists a very good agreement between different data sets at least up to $AoA=12$ deg. In the same figure, the drag coefficients determined from CFD are compared against those found from two of the three references mentioned above. Despite the small discrepancies at higher AoAs, it seems CFD predictions are between what found by the two independent experimental efforts. In addition to the force coefficients, the distribution of the pressure coefficient over the airfoil surface at mid-span is obtained for turbulent flow around a solid airfoil with $AoA=0^\circ$ using CFD, and the results are compared against the available experimental data (Wadcock, 1978) in Figure 36b. An excellent agreement is observed between the two data sets, and this confirms the validity of the CFD formulation and results.

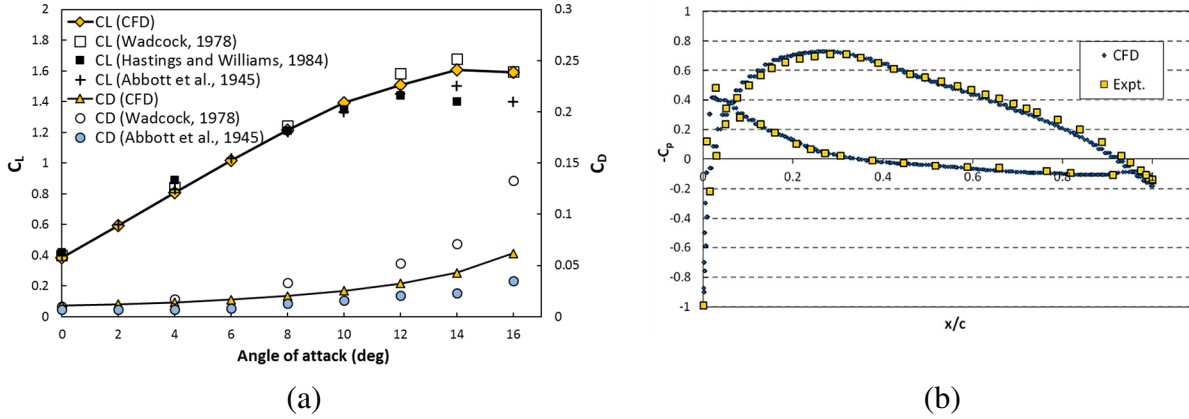


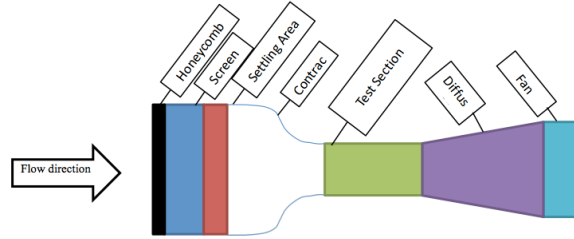
Figure 36 Results of the experimental validation study for flow over a solid airfoil: (a) lift and drag coefficients at various AoAs, and (b) pressure coefficient with a negative sign at AoA=0.

5.4.2 Wind Tunnel Experiments – Slotted Airfoil

To gain more confidence about the validity of the forthcoming simulations and methodology used for the slotted airfoils, it is decided to conduct a series of wind tunnel experiments and measure lift and drag forces directly for a slotted airfoil at various AoAs. All the laboratory experiments for this project are conducted in an open-loop, suction-type wind tunnel at UWM. The test section of this tunnel has the cross-section dimensions of 1.2 m x 1.2 m, and it is 2.4 m in length. The total length of the tunnel is approximately 12 m, and a 40 HP electric motor drives the eight-blade fan at the exit, and thereby draws the air through the tunnel. Moreover, five thin honeycomb mesh plates are installed at the entrance of the tunnel to deliver a more uniform and less turbulent flow to the test section. The wind tunnel can produce subsonic airflow as large as 20 m/s. This wind tunnel has been used in several experimental efforts in the past, e.g., for determination of velocity deficit downstream of one or two small rotating wind turbines (Jackson, 2016; Jackson and Amano, 2017). The overall view and a schematic diagram of the wind tunnel components are presented in Figure 37.



(a)



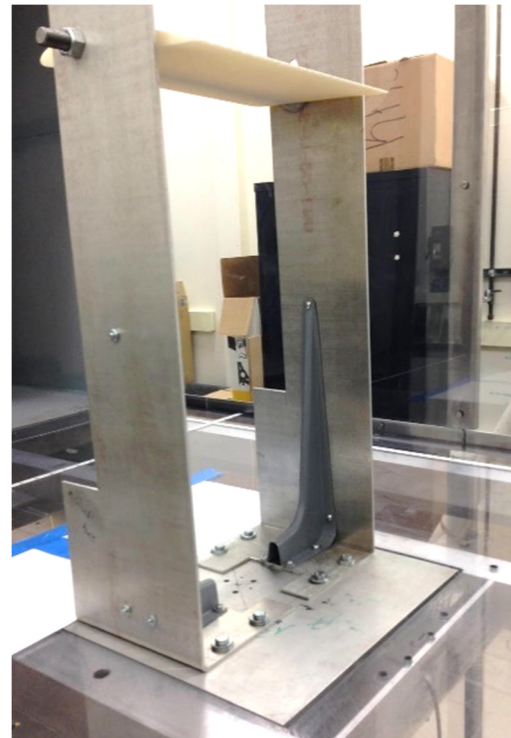
(b)

Figure 37 UWM Wind tunnel: (a) overall view, and (b) schematic diagram of different components (Alsultan, 2015)

The solid and slotted airfoils were designed in Pro-Engineer software package, with the chord length of 17.5 cm and span length of approximately 25 cm. They were then manufactured using the 3D-printing technique. The material used for 3D printing is Renshape SL 5220, due to the superior performance it has shown compared to another candidate material in an FEA study (Alsultan, 2015). Figure 38a shows the slotted airfoil fabricated for this study. The slot is quite short and wide, with the relative first-leg length L_1/c of 10% and the relative width w/c of 2%.



(a)



(b)

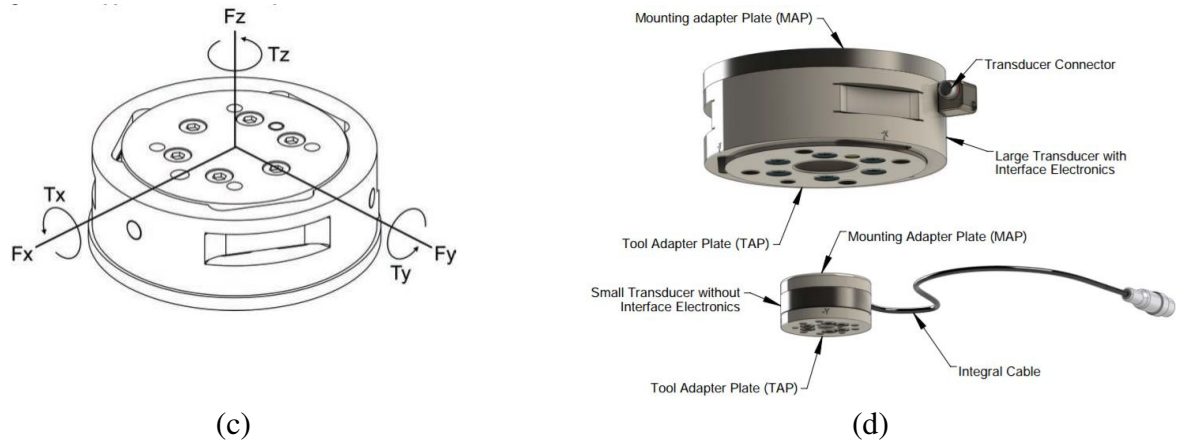


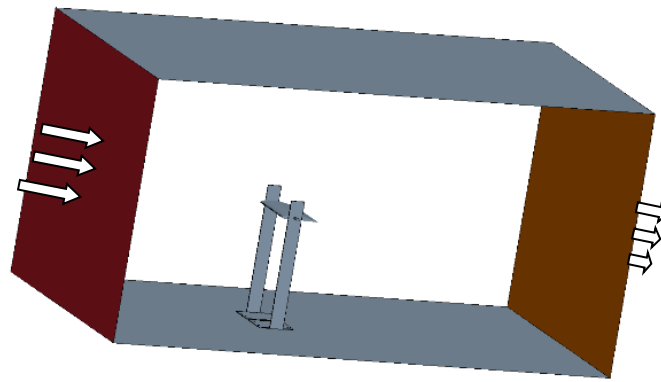
Figure 38 (a) the slotted NACA 4412 airfoil used for the experimental analysis, (b) the support structure made for holding the airfoil in the wind tunnel, (c) schematic diagram of the F/T transducer with the direction of the force and torque components shown, and (d) different physical components of the transducer

The airfoil to be tested is attached to the sides of an aluminum structure through bolted rods as shown in Figure 38b. Angle of attack is adjusted and then the screws are tightened. The entire structure sits over a 6-axis ATI Force-Torque (F/T) transducer, which can effectively measure lift and drag forces (ATI Industrial Automation, 2017). Two different views of the transducer are provided in parts c and d of the same figure. The steps needed to be taken for successful measurement of lift forces are outlined below. Note a similar procedure is followed for measurement of the drag force.

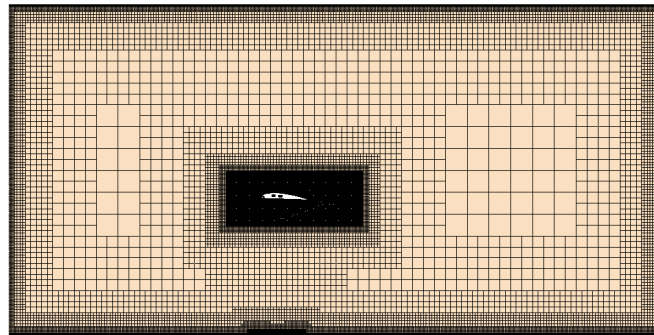
- 1) Calibrate the device for the lift force using known weights
- 2) Adjust AoA and set the fan speed to deliver the desired air velocity; a linear correlation between the fan speed and the mean velocity is obtained previously (Jackson, 2016).
- 3) Measure the lift force of the structure
- 4) Measure the lift force of the structure + airfoil
- 5) Subtract (3) from (4) to get the net lift generated due to the presence of the airfoil in the tunnel

For every AoA, force data were collected for 10 seconds with a samples rate of 1 kHz, and the average value were determined. A series of lift measurements was carried out and some discrepancies with the expected results (from literature) was observed. The root cause of the

discrepancy was deemed to be the presence of the structure which made the flow patterns different than what experienced in an open environment. To test this hypothesis, a new CFD setup was created and simulated at different angles of attack. Figure 39a shows the developed geometry of the airfoil and structure installed inside a wind tunnel. All dimensions match those of the actual wind tunnel where the wind tunnel tests were carried out. The computational setting of this new setup matches with those described earlier. The mesh generated on the vertical mid-plane of the tunnel is presented in Figure 39b. Velocity inlet and pressure-outlet boundary conditions were imposed on the inlet and outlet surfaces of the tunnel, respectively. Top, bottom, and the two side walls of the tunnel were assigned no-slip wall condition.



(a)



(b)

Figure 39 (a) the new geometry developed in Star-CCM+ for analysis of the flow around a slotted airfoil inside a wind tunnel (the side walls are hidden for higher clarity), (b) cross section of the grid structure on the vertical mid-plane

CFD simulations were performed for AoAs 0, 4 and 8 degrees, with the inlet velocity of 9 m/s (which was verified to be equal to the mean inlet velocity of the wind tunnel operating with the fan speed of 30 Hz). Figure 40 shows the comparison of the lift and drag coefficients between CFD and experiments. One can verify that there is a very good agreement between both lift and drag coefficients of the two sets of data. Small discrepancies can be attributed to the uncertainties in velocity magnitude and turbulence intensity of the tunnel, among other reasons. The level of agreement between the actual wind tunnel data and CFD results confirms the validity of the CFD settings, models and results. Therefore, in the remaining parts of this research, the analysis of the slotted airfoil is carried out mostly computationally, although some data from a wind-tunnel experiment on solid and slotted airfoils is presented as well.

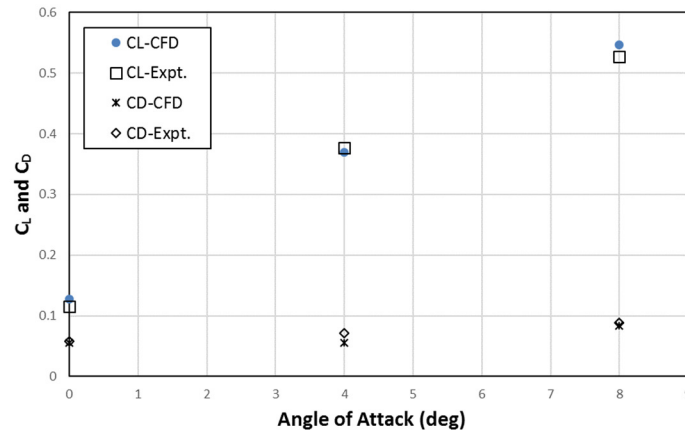


Figure 40 Lift and drag coefficients obtained from wind tunnel experiments and CFD simulation with a matching geometry at different AoAs

5.5 Preliminary Results

5.5.1 Performance at AoA=0

In an attempt to determine the optimum geometric configuration of the slot, a series of computational parametric studies were performed, in which three of the geometric properties were independently varied, and lift and drag coefficients were calculated. The variables of interest for these simulations were the first-leg relative length percentage (L_1/c), slot width w

(which was always kept identical between the first and second legs of the slot), and the deflection angle of the second leg with respect to the first leg, β_2 . The results of the 14 configurations examined are outlined in Figure 41. The values of the variables treated as constant in each series of simulations are indicated above the corresponding columns. Note in all of the cases in this section, the slot first-leg angle β_1 is set to zero and $h/c=4\%$. From Figure 41a, it is evident that all the simulation cases outperform the solid airfoil case regarding the lift coefficient. This improvement can be as high as 65% for the best case. At a fixed exit angle and slot width, it is shown that lift coefficient increases with L_1 .

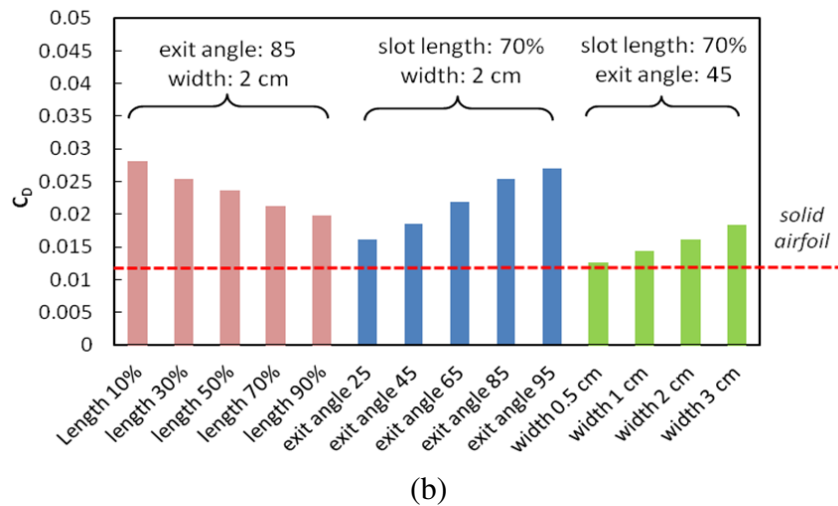
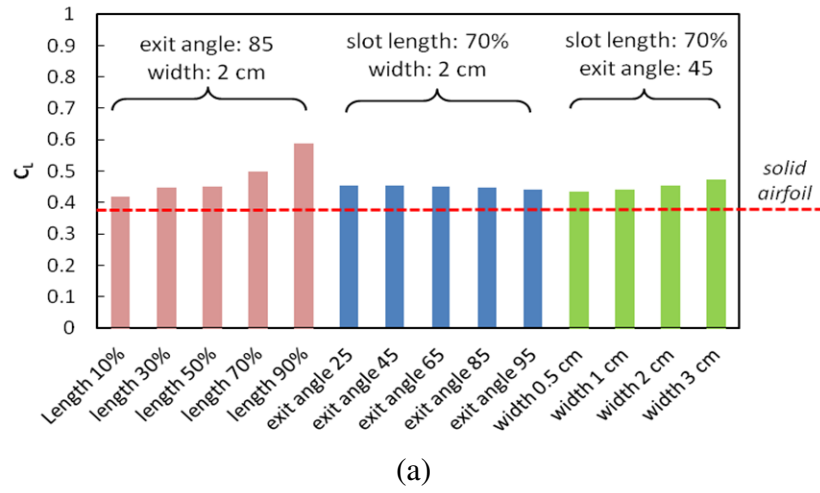


Figure 41 Results of a parametric study on (a) lift, and (b) drag coefficient, as a function of slot first-leg length, slot width, and the exit angle

Meanwhile, one can note the very large C_D values in part b of the same figure. From the second set of simulations in Figure 41a and b, it is found that unlike the slot length, the exit angle β_2 does not play a significant role in determination of the lift. However, slots with smaller β_2 result in lower drag forces. Therefore, this angle is recommended to remain small in future investigations. Finally, from the third set of simulations ($L_1/c=70\%$ and $\beta_2=45^\circ$), it is found that wider slots will result in slightly higher lift, but also much higher drag as compared to the narrower slots. Therefore, it is recommended to keep the slot width as small as practically possible.

In summary, even though all of the chosen cases result in an improved lift, there seems to be an inevitable drag penalty. If one's objective is only to maximize the lift, the fifth case ($\beta_2=85^\circ$, $w=2$ cm, $L_1/c=90\%$) seems to be the optimum solution. However, if the drag has to be taken into account (i.e., if lift-over-drag ratio is to be maximized), the 11th case ($\beta_2=45^\circ$, $w=0.5$ cm, $L_1/c=70\%$) seems more appropriate *among the cases studied*. Overall, one can conclude that it is better to keep L_1 as large as possible, while keep w and β_2 as small as possible.

5.5.2 Effect of Slot Width and First Leg Length

All three quantities explored in the previous section seem to be somewhat influential in the determination of lift and drag. While other geometric variables can potentially impact the performance, in this section the variation of lift and drag as a function of only two variables, i.e., w and L_1 is investigated. Especially, the former is important because it can directly determine the amount of air flowing through the slot and ejecting from the suction side, and therefore, it can alter the pressure distribution and flow dynamics around the airfoil. In Figure 42, the simulation results for turbulent air flow over a slotted airfoil with four different slot widths are presented. Lift and drag coefficients are obtained for slot widths of 0.5, 1, 2, and 3 cm at AoAs of 0, 2, 4, 6

and 8 degrees. Same is reported for a *solid baseline* airfoil without any slot drilled inside. As discussed earlier, all slot widths prove to be beneficial for improvement of lift at zero AoA, whereas, at AoA=2°, only the three smallest airfoil widths show higher lifts compared to the solid airfoil. As AoA increases, the solid airfoil seems to generate more lift and less drag as compared to any slotted airfoil. This means that using the slots with configurations above cannot improve the aerodynamic performance of NACA 4412 airfoils at Re=1.6E+6.

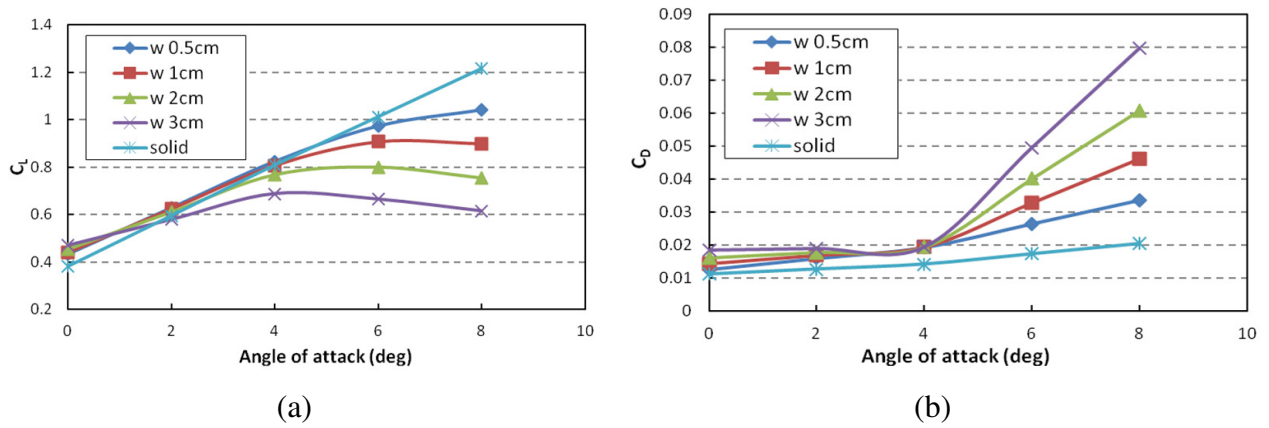


Figure 42 Performance of slotted airfoils (with $c = 1$ m) with different slot widths in terms of (a) lift coefficient, and (b) drag coefficient

Similarly, the effect of the slot first-leg length L_1 on lift and drag coefficients at Re=1.6E6 is demonstrated in Figure 43. For AoAs 0° and 2°, all of the slotted airfoils generate higher lift than the solid one, with the $L_1/c=90\%$ case showing the best performance. However, at higher AoAs, the solid airfoil shows a better performance, while all five slot lengths considered seem to have the same impact. A similar trend is observed for the drag coefficient, where the solid airfoil comes with the smallest drag, followed by $L_1/c=90\%$ slotted airfoil, and then the rest of the test cases. One can justify the inferior performance of the aforementioned slotted airfoils at higher AoAs by noting that based on the current vertical position of the slots, incoming air streams cannot enter the slots from the leading edge, and instead they tend to enter the slot from the bend.

The reverse flow through the slot could alter the pressure distribution over the slot surface and could generate an undesirable downward force that results in smaller lift coefficient.

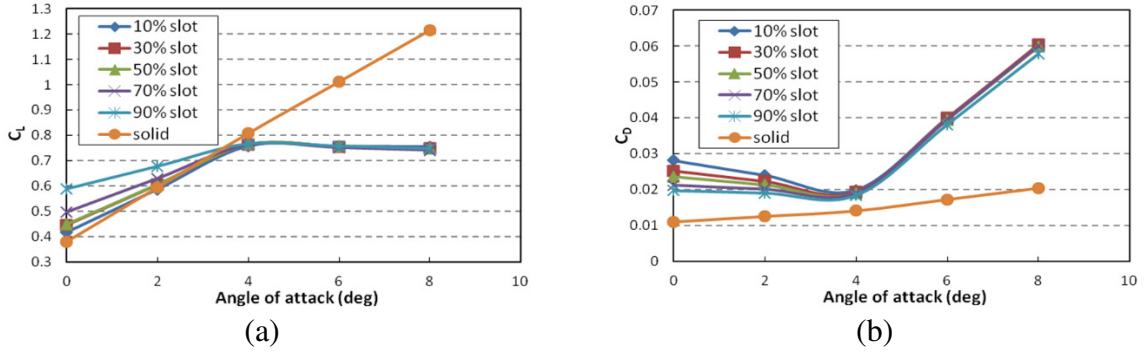


Figure 43 Performance of slotted airfoils with different first-leg lengths in terms of lift and drag coefficients

Figure 44 shows the local velocity vectors in the spanwise mid-plane near the airfoil for the two cases with AoAs of 0 and 8 degrees. The other slot parameters are as follows: $L_1/c=70\%$, $w/c=2\%$, $\beta_1=0^\circ$, $\beta_2=85^\circ$, and $h/c=4\%$. While the flow pattern in the AoA=0° case (part a) is as expected, there exists reverse flow in the AoA=8° case (part b). This happens because in the latter case, the stagnation point is located below the slot's inlet, and therefore the incoming streamlines cannot find their way through the slot. However, the condition for entering through the back end of the slot is quite plausible. This phenomenon explains degradation of the lift at higher AoAs for the cases with $h/c=4\%$.

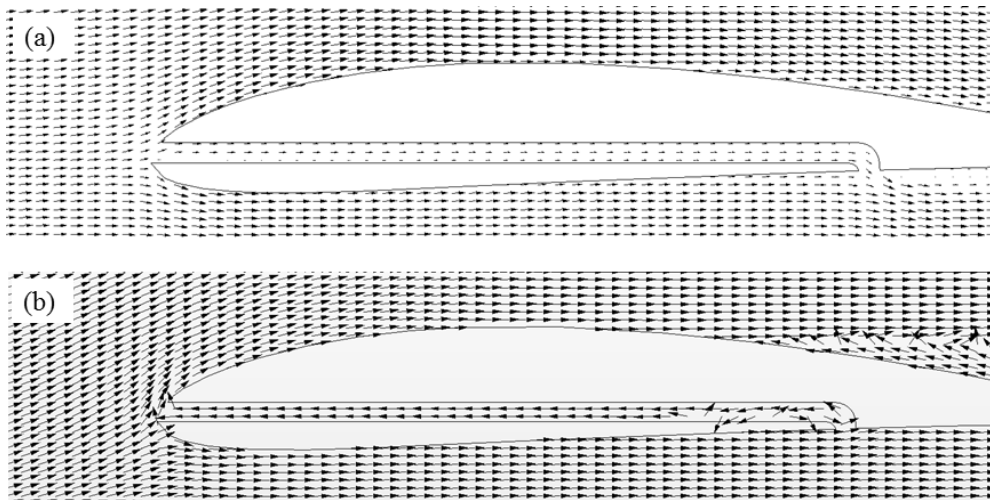


Figure 44 Velocity vectors near a slotted airfoil with $L_1/c=70\%$, $w/c=2\%$, $\beta_1=0^\circ$, $\beta_2=85^\circ$, and $h/c=4\%$ operating under (a) $AoA=0^\circ$, and (b) $AoA=8^\circ$

5.5.3 Effect of Slot Inlet Angle

To make slots more advantageous for AoAs greater than zero, it is now proposed to adjust the slot inlet angle β_1 according to the incoming flow AoA. In this section, flow around slotted airfoils with different β_1 values is simulated at $AoA=4^\circ$. The results for cases with $\beta_1=0, 4, 8$, and 16 deg are listed in Table 4. The $\beta_1=0$ case generates the least amount of lift, which is even less than that of the solid airfoil. As β_1 increases, C_L continually increases, and it exceeds that of the solid airfoil. The maximum lift improvement over the solid case is around 3% for the case with $\beta_1=16^\circ$. Also, all values of β_1 result in almost identical drag coefficients that are only slightly higher than that of the solid airfoil. Therefore, it is decided to use slots with small tilt angles in the remaining parts of this research.

slot inlet angle β_1 (deg)	Lift Coefficient	Drag Coefficient
0	0.799	0.0143
4	0.825	0.0144
8	0.827	0.0147
16	0.832	0.0149
solid airfoil	0.808	0.0141

Table 4 Lift and drag coefficients for slotted airfoils with different first-leg angles

5.6 Results and Discussions

In the previous section, results of several simulations were presented. Even though the lift coefficient seemed to show some improvement as compared to the solid airfoil in the low AoAs, all of the slotted cases had an inferior performance at higher AoAs. Moreover, there seems to be a significant drag penalty observed for all of the cases even at low AoAs. After investigation of the velocity vectors near the slot inlet, it was decided to slightly lower the slot in order to allow it

to capture more incoming air flow. The parameter h (see Figure 35b) was therefore changed from 4 cm (0.04c) to 5.5 cm (0.055c). Also, based on the findings of the previous section, a very mild inclination angle ($\beta_1=2^\circ$) was applied to slot's first-leg and it was maintained for all simulation cases, regardless of the value of other geometrical parameters and AoA. The intention was to help the slots with capturing more incoming air at higher AoAs. Similar to the previous section, the influence of the five main variables, i.e., slot first-leg length, width, inlet and exit angles, and vertical position were studied on lift and drag coefficients.

5.6.1 Effect of the First-Leg Length and Slot Width

Figure 45 shows how lift and drag coefficients change with AoA as the first leg length varies between 10%-80% of the chord length. For all three cases, the slot width and the exit angle of the second leg are maintained at $w/c=0.01$ and $\beta_2=25^\circ$, respectively. Note that all the cases show a superior performance as compared to the solid airfoil for AoAs as large as 10° . This performance is a testimony of definitely an improvement compared to the original slot design where the slot was drilled higher up (see Figure 42 and Figure 43, where the performance of all the slotted airfoils started degrading at AoA= 4° and above). While the three slot lengths considered in Figure 45 are showing similar behavior; it is decided to use the longest one ($L_1/c=80\%$) due to its slightly higher lift and lower drag especially at higher AoAs). The only drawback of the long slot would be the need for more ductwork and plumbing in order to implement the slot inside the airfoil. However, the overall weight and the installation cost are not considered as objective functions in the present work, and can be items of a future study.

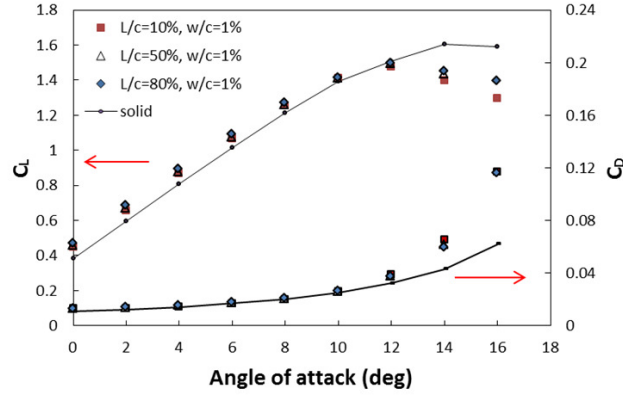


Figure 45 Lift and drag coefficients of slotted airfoils with different first-leg lengths, $w/c=1\%$, and $\beta_2=25^\circ$ at different AoAs

Despite the current findings, there is still room for improvements, so it is decided to explore the impact of slot width at different AoAs, while setting L_1/c to 80%. Slot width is varied in a reasonable range: $w/c=0.25\%$, 0.5% , 1% , and 2% . For practical reasons, widths beyond this range are not tested. For instance, for the slots narrower than 0.25% of the chord length in width, the air passage through the slot may become clogged up as a result of dust accumulation. Lift and Drag coefficients at different AoAs for various slot widths are presented in Figure 46.

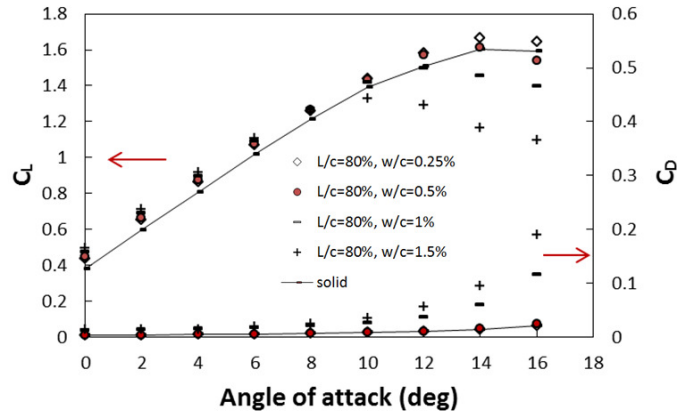


Figure 46 Lift and drag coefficients of slotted airfoils with different slot widths, $L_1/c=80\%$, and $\beta_2=25^\circ$ at different AoAs.

As shown above, the choice of slot width does not play a crucial role in low AoAs as long as the length is selected properly. For AoAs up to 8° , all the selected widths can result in lift coefficients that are anywhere between 5-30% higher than the solid counterpart. For higher

AoAs, however, there seems to be some disagreement between the lift predictions of slotted airfoils with different widths. For AoAs between $10\text{-}14^\circ$, while the two narrowest slots still provide some advantage compared to the solid airfoil, the two widest ones start degrading in performance. For the highest AoA considered (16° , which is the post-stall condition), only the narrowest one seem to be better than the solid airfoil.

A similar behavior is observed for the drag coefficient. Airfoils with slot widths of $w/c=1\%$ and 1.5% perform very poorly, while the other two maintain their acceptable performance even at the $\text{AoA}=16^\circ$. Neglecting the possible issue of clogging the slot, the slotted airfoil with $w/c=0.25\%$ seems to be the best option. This slot provides an average lift coefficient improvement of 7% (15% for $\text{AoA}=0^\circ$, and 3.25% for $\text{AoA}=16^\circ$) with respect to the solid airfoil in the *entire range* of AoA examined, while it yields almost no drag penalty. Comparing the above results with those from Figure 42 (similar study but with the slot drilled higher up inside the airfoil) reveals that the slot's vertical position can have a significant impact on the overall aerodynamic performance.

To provide more insights into the flow patterns around and through slotted airfoils, the contours of pressure and normalized velocity (U_i/U_∞) are presented in Figure 47. One can note in part a that the presence of the slot slightly below the stagnation point of the airfoil causes the high-pressure fluid particles (adjacent to the streamline hitting the airfoil nose) to find their way through the slot. The flow of the high-pressure air through the slot creates an upward force on the slot ceiling. Even though a similar force pushes down the bottom surface of the slot, due to the small difference between the areas of the two surfaces, the net force will remain upward. Also, the pressure on the top surface (ceiling) of the slot is slightly greater than that of the slot's floor. As a result, this contributes to few percent increase in lift. Another phenomenon contributing to

the lift increase is the effect of the upward thrust force created on the airfoil because of the jet of air existing downward from the slot.

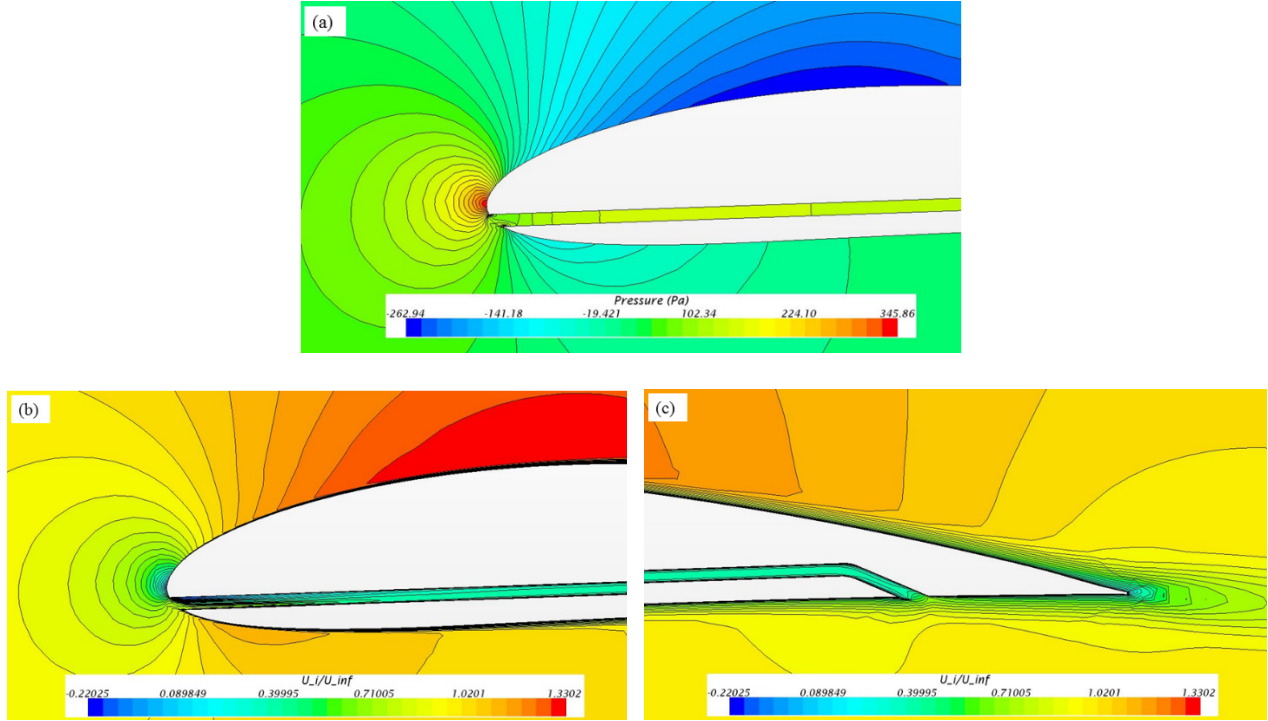


Figure 47 (a) Pressure contours near the leading edge, (b) normalized velocity contours near the leading edge, and (c) normalized velocity contours near the trailing edge, for a slotted airfoil with $L_1/c=80\%$, $w/c=1\%$, $\beta_1=0^\circ$, $\beta_2=80^\circ$, and $h/c=5.5\%$ at $AoA=0^\circ$

5.6.2 Effect of the Slot Exit Angle

For a slotted airfoil with $L_1/c=80\%$ and $w/c=0.5\%$, the influence of the *relative* exit angle of the second leg β_2 is studied. This angle can alter the pattern of mixing between the slot flow and the flow on the pressure side near the trailing edge, and therefore can contribute to the lift and drag coefficients. Three exit angles 10, 25, and 85 degrees are considered, and the force coefficients are compared against the data from the solid airfoil in Figure 48. For low to moderate AoAs, there is not a significant difference in the lift coefficients between the cases with different β_2 values. Only at near-stall AoAs (14 and 16 degrees), the larger exit angle seems to result in a slightly higher lift. The same statement can be made regarding the drag coefficient. However, since the overall difference between the performance of slotted airfoils with $\beta_2=25^\circ$

and $\beta_2=85^\circ$ is not significant, it is decided not to change the exit angle very much in this research.

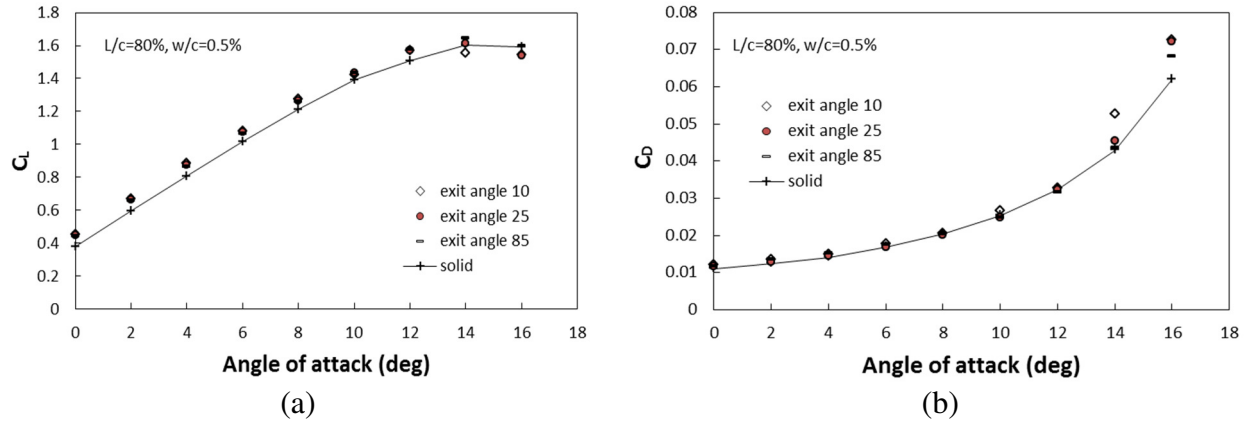


Figure 48 Performance of slotted airfoils with different relative exit angles β_2 , with $L/c=80\%$, and $w/c=0.5\%$ (a) lift coefficient, and (b) drag coefficient

5.6.3 Effect of the Slot Inlet Angle

Comparing the above results with those for the horizontal first-leg (cases with $\beta_1=0$) confirms the advantages of tilting up the first leg. In the present section, few more upward tilt angles are applied to a slotted airfoil, and results are presented for different AoAs in Figure 49. From AoA 0 to 4° , the horizontal slot and all the upward-tilted slots yield similar lift and drag coefficients, and they all outperform the solid airfoil. It is, however, beyond AoA= 4° where the horizontal slot design starts degrading in performance, but the airfoils with upward-tilted slots continue showing better performance compared to the solid one. In fact, for the horizontal slot design ($\beta_1=0$), the lift (drag) coefficient becomes even lower (higher) than the baseline solid airfoil.

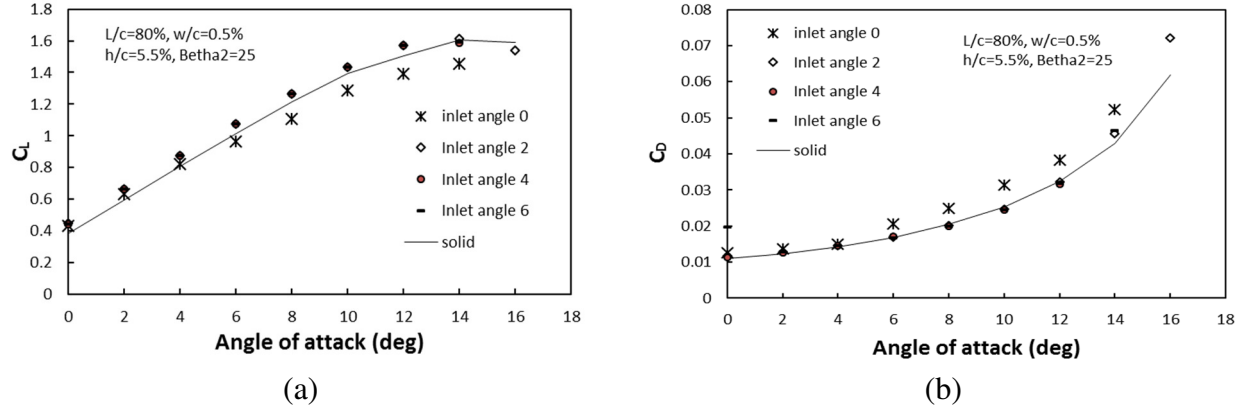


Figure 49 (a) Lift and (b) drag coefficients of slotted airfoils with different inlet upward-tilt angles β_1 , with $L/c=80\%$, $w/c=0.5\%$, and $\beta_2=25^\circ$ at different AoAs

In Figure 49, even though the difference between the results of the cases with $\beta_1=2, 4$, and 6 degrees may seem insignificant (mainly due to scale of the plots), a closer look at the lift-to-drag ratios of different cases reveals that the choice of the inlet angle indeed can be somewhat influential for airfoil design. Figure 50 summarizes the lift-to-drag ratio (L/D) values obtained from the cases with different β_1 and at various AoAs. At least for half of the AoAs considered, there seems to exist an optimum configuration in the middle of the range, i.e., $\beta_1=4$ seems to be the best one among the three values considered. For the rest of the AoAs, β_1 is not a crucial factor. In future, it is suggested to keep β_1 close to 4 degrees. However, it might be worth studying few more β_1 values such as 3 and 5 degrees, to see if better L/D values can be achieved.

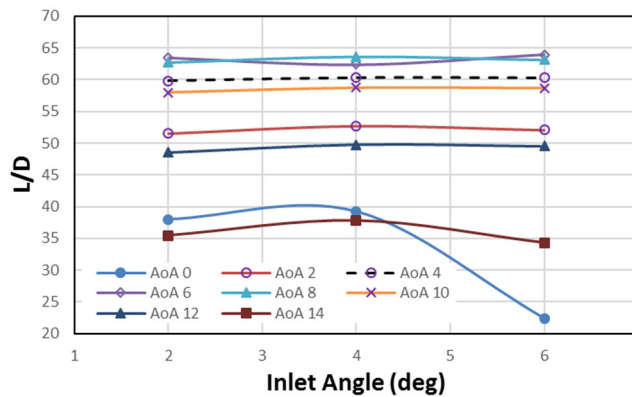


Figure 50 Lift-to-drag ratio versus slot inlet angle β_1 for different angles of attack, for slotted airfoils with $L/c=80\%$, $w/c=0.5\%$, $h/c=5.5\%$, and $\beta_2=25^\circ$

5.6.4 Effect of the Slot Vertical Position

As mentioned in previous sections, lowering the entire slot such that the slot's inlet plane is located slightly below the stagnation point can help with guiding flow through the slot, and ultimately improve lift and drag. In the present section, the effect of the vertical distance between slot's lower lip and a pre-defined point within the airfoil (h ; refer to Figure 35b) is studied for few h values at different AoAs. It is evident from Figure 51 that the original location of the slot ($h/c=4\%$) is suitable for AoAs less than or equal to 4° , but it results in the lower lift and much higher drag compared to the solid airfoil at greater AoAs. This undesirable behavior is due the fact that at higher AoAs, the stagnation point is slightly below the lower lip of the slot, and therefore the rate of the air flow through the slot is insignificant. The benefit of lowering slot is also demonstrated in Figure 51b, where it is again shown that all of the lowered-slot cases maintain a superior performance compared to the solid airfoil as the AoA increases.

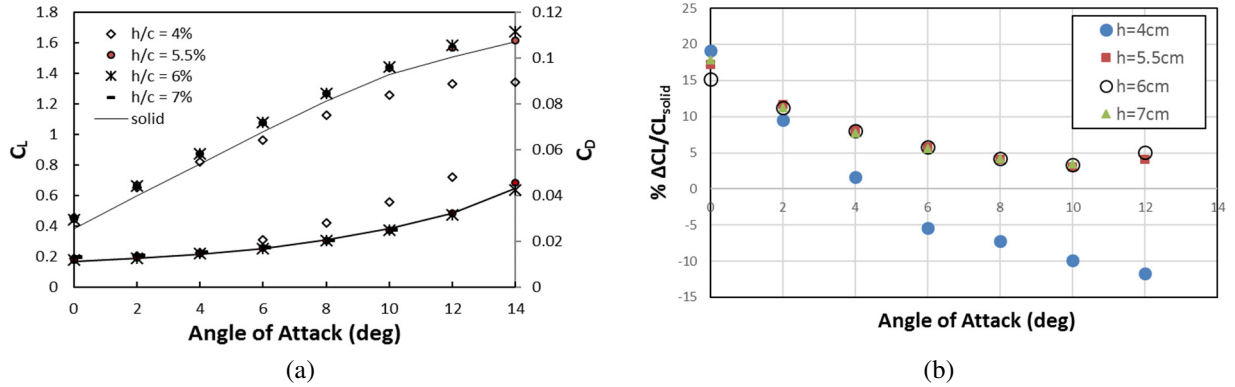


Figure 51 (a) Lift and drag coefficients, and (b) percentage of lift improvement with respect to the solid airfoil, for slotted airfoils with different inlet vertical positions h , and $L/c=80\%$, $w/c=0.5\%$, $\beta_1=2$, and $\beta_2=25^\circ$ at different AoAs

To seek an optimal vertical position, L/D is plotted versus the vertical position h in Figure 52. Despite the indistinguishable performance of $h/c=5.5\%$, 6% and 7% in Figure 51, it is now shown that there exists a pseudo-optimum h/c value somewhere between 5.5% and 6% depending on the AoA. Some insights into the reason behind having an optimal vertical location is presented as follows: For low values of h/c (such as 4%), the stagnation point is above the slot

inlet, and hence, less flow through the slot and a lower lift. On the other hand, at very high h/c values, the slot's mouth and the stagnation point are too far apart, and therefore, the pressure of the fluid particles entering the slot is not as large as the cases where the slot's inlet is closer to the stagnation point. Therefore, it is expected to have an optimal h value, somewhere between 5.5% and 6%. Note, however, that this optimum value is obtained for slots with certain values chosen for other geometrical parameters.

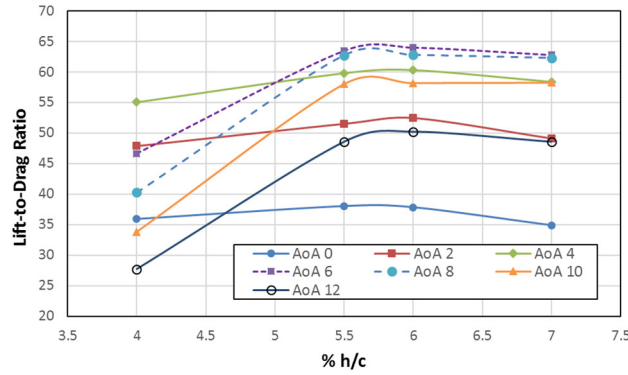


Figure 52 Lift-to-drag ratio for slotted airfoils with different inlet vertical positions h , and $L/c=80\%$, $w/c=0.5\%$, $\beta_1=2$, and $\beta_2=25^\circ$ at different AoAs

One can summarize the physical reasons behind the usefulness of the slots as follows: (1) As the high-pressure air (immediately below the stagnation point) enters the slot, it exerts a large upward force to the ceiling (top surface) of the slot. Even though a similar force is applied on the slot's floor, one should note that first, the former force is slightly larger than the latter (especially near the bend), and second, the overall length and the surface area of slot's ceiling is a bit greater than that of the slot's floor. The net force is therefore upward and elevates the lift (both above-mentioned points are graphically shown for a slotted airfoil in Figure 53); (2) The downward vertical component of the flow exiting the slot can generate a net upward reaction force on the airfoil, due to the conservation of the momentum. However, because of the small magnitude of the flow rate through the slot, this phenomenon may not be as influential as the first one.

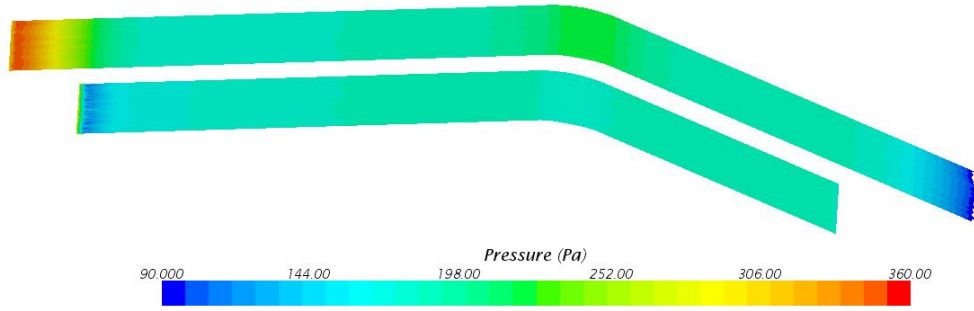
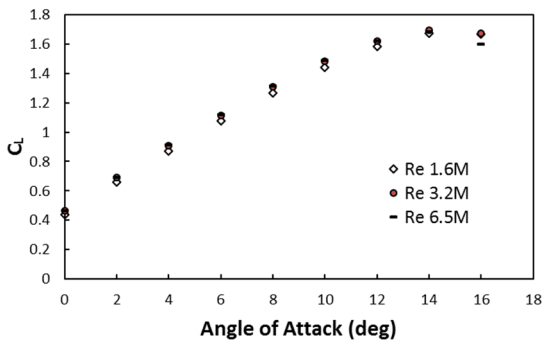


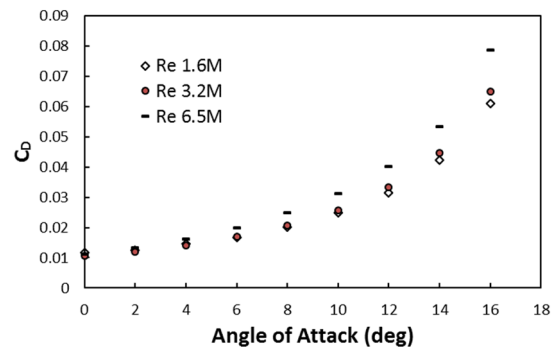
Figure 53 Pressure distribution on the top and bottom surfaces of a slot with $L_1/c=10\%$, $w/c=1\%$, $\beta_1=2^\circ$, $\beta_2=25^\circ$ and $h/c=5.5\%$ with $AoA=6^\circ$

5.6.5 Operation at Different Reynolds Numbers

To gain information about the scalability of the proposed methodology and the results presented so far, it is desired to study the effect of the Reynolds number on the aerodynamic performance of slotted airfoils. Based on what is determined so far, one of the most suitable slot configurations (with $L_1/c \sim 80\%$, $w/c=0.5\%$, $h/c=6\%$, $\beta_1=2^\circ$, and $\beta_2=25^\circ$) is chosen, and the force coefficients at different AoAs are obtained not only for the baseline Re , but at Reynolds numbers twice and four times as large. One can see in Figure 54 that the difference between the data for the two smaller Re values is not much significant. However, the performance of the slotted airfoil degrades at the highest Re value, especially at AoAs greater than 4° . Despite the differences observed, the trend of the data is the same between the three cases. The maximum lift value is located at $AoA=14^\circ$ and the maximum lift-to-drag ratio is seen at $AoA=6^\circ$ for all three Reynolds numbers considered.



(a)



(b)

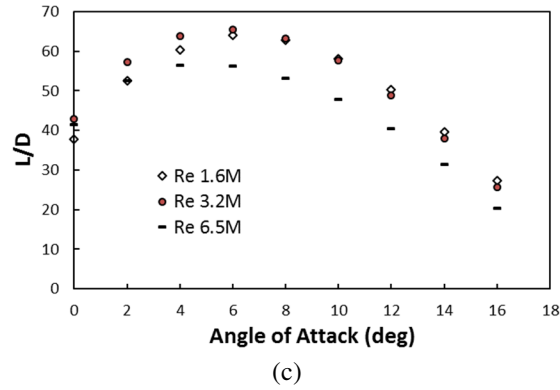


Figure 54 (a) Lift coefficient, (b) drag coefficient, and (c) lift-to-drag ratio for slotted airfoils with different Reynolds numbers, and $L/c=80\%$, $w/c=0.5\%$, $h/c=6\%$, $\beta_1=2$, and $\beta_2=25^\circ$ at different AoAs.

5.6.6 Experimental Results

To demonstrate that slots are not only beneficial in computational analysis, a series of experiments were conducted at UWM wind tunnel, and the lift coefficients were determined for a solid and a slotted airfoil. The wind tunnel mean velocity was around 9 m/s. As shown in Figure 55, for all of the AoAs where the measurements were taken, the slotted airfoil either matches or outperforms the solid airfoil. This again confirms the suitability of leading-edge slots for improving the aerodynamic performance of NACA 4412 airfoil at various AoAs.

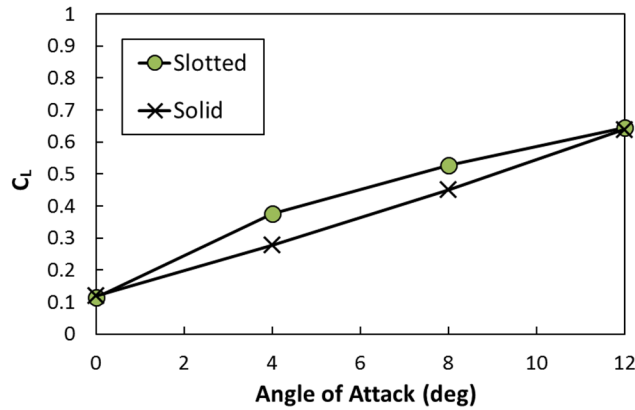


Figure 55 Lift coefficient determined experimentally for the solid and the slotted airfoils tested in wind tunnel at three different AoAs

5.7 Conclusion

The feasibility of using leading-edge slots for improvement of the aerodynamic performance of a cambered airfoil was investigated. After validation of the CFD results using both the

literature data and wind tunnel tests, it was observed that a properly designed slotted airfoil could improve lift under certain conditions. The influence of slot's first-leg length, slot's width, slot's upward tilt angle, slot's exit angle, and slot's vertical position were studied at different AoAs. Slot's width was varied in a reasonable range, and it was shown that in general, as the width decreases, the lift coefficient increases while drag does not change significantly. Therefore, a small width of $w/c=0.5\%$ was chosen and maintained for the majority of the remaining investigations in this chapter. Next, the impact of slot's first-leg upward tilt angle β_1 was studied and it was shown that even a small tilt angle can improve the lift and drag characteristics of a slotted airfoil for the entire range of AoA considered. Finally, the position of the slot was varied in the normal direction, and it was shown that lowering the slot from its original position (with $h/c=4\%$) improves the performance of the airfoil. Plots of L/D vs h/c revealed that the mid-range values of $h/c=5.5\%-6\%$ is better than the two end values.

In addition to the computational investigations, the usefulness of slots was also demonstrated by conducting a series of wind tunnel tests on two 3D-printed airfoils, one solid and one slotted. Lift coefficients were determined for each airfoil at several AoAs, and it was found that the lift coefficient of the slotted airfoil is in general greater than that of the solid one.

The main conclusion of the present work based on both CFD and experimental results is that by appropriately adjusting certain geometrical parameters of the airfoil, it is possible to reach a configuration that results in improved lift coefficient with respect to the baseline solid airfoil, *without sacrificing the drag*.

Now that the main influential design variables are identified, it is proposed to conduct a set of Design of Experiment and multi-variable optimization studies, in which those variables are defined in reasonable ranges to seek the best design point. The objective function will be either

lift coefficient or lift-to-drag ratio. More complex objective functions can be defined after considering variables such as the additional weight associated with the required duct work, and the cost of installation and maintenance. Note that the optimization will be carried out only at AoA of 6 degrees, which is the peak of the L/D vs. AoA curve, and therefore, the nominal AoA for wind turbine blades operating with NACA 4412 airfoil profile. However, once the framework of optimization is established, one can repeat the procedure for other AoAs if desired. Results of the design of experiment (DoE) and optimization studies on slotted airfoils is presented in the next chapter.

Chapter 6 Slotted Airfoil Multi-Variable Analysis

6.1 Introduction

In the previous section, results of several single-variable parametric studies on various geometrical properties of a slotted airfoil were investigated for operation at certain Reynolds numbers. Even though the preceding results can provide valuable insights into the performance of the slotted airfoils and sensitivity of lift and drag to different parameters, it is necessary to conduct another study in a multi-variable fashion to examine the interplay of different variables. To this end, a step-by-step approach is followed, where three sets of design-of-experiment (DoE) studies each with two independent variables are carried out, and a response surface (RS) best fitting the data points is obtained for each case. The information gathered after each DoE study is used in subsequent steps to decide (a) whether a geometrical parameter should be treated as constant or variable, and (b) what constant value or range of values it should take. Note the forthcoming methodology can develop a framework, which allows future investigators to optimize any objective function relevant to slotted airfoils (as well as airfoils with any other geometrical alterations) under various operating conditions, e.g., different AoAs or different Reynolds numbers. Depending on the application, the objective function can be lift, drag, or lift-over-drag (LoD), each with or without considering additional parameters such as weight, installation cost, etc.

6.2 Methodology

To find the simultaneous impact of different geometrical parameters, three DoE studies each with two independent variables are defined and executed. The reason behind choosing two variables was to help with visualizing the results using response surfaces. There are different types of DoE commonly used in optimization studies, and some of them are briefly outlined

below. Moreover, a brief description of the SHERPA optimization algorithm is presented in the subsequent subsection.

6.2.1 Two-level and Three-level Factorial Design

In the two- and three-level factorial designs, a valid range is first defined for each independent variable, and the minimum and maximum values that each variable can take are identified. For the three-level design, the midpoint values are identified as well. Throughout the study, each variable can only take those 2 (or 3) discrete values. Therefore, for a study with n independent variables, the total number of experiments conducted for a two-level factorial design will be 2^n , and for a three-level design will be 3^n . As an example, the 8 total experiments for a two-level design with three variables A, B, and C are outlined in Table 5, where + and – signs indicate the maximum and minimum value of each variable, respectively.

Experiment Number	A	B	C
1	–	–	–
2	–	–	+
3	–	+	–
4	–	+	+
5	+	–	–
6	+	–	+
7	+	+	–
8	+	+	+

Table 5 An example of a two-level factorial design for a study with three variables

6.2.2 Central Composite Design

Even though the three-level factorial designs provide a good set of data points in the design space, it is usually difficult to afford such designs even for small number of independent variables. For instance, for $n = 6$, there needs to be 3^6 (729) experiments defined. A common and well-accepted compromise that reduces the number of experiments to close to the two-level factorial design is the *central composite design* (CCD). A Central composite design is a factorial design with center points, augmented with a group of axial points (also called star points) that let

the user estimate the curvature of the fitted surface. Those axial points are positioned in the design space such that their distances to the central point is typically the same as the distance between any other design point and the central point. The CCD is composed of the 2^n points of the two-level full factorial design with all the variables at their extremes, plus the nominal design located at the center of the domain (the origin), plus the additional $2n$ points obtained by starting from the central point and then moving one design variable at a time by an amount α . Figure 56 show the central composite design for $n = 2$ and $n = 3$. The value of α chosen in this figure is such that all the points outside the origin are of the same distance from the origin, so that a *spherical* design space is formed. This placement of the points is at the higher end of the typical choice for α ; smaller values can be also used. CCD and another similar well-known DoE method Box-Behnken Design (BBD) are fully described in many references (Myers, 1971; NIST, 2017; etc.), and are not repeated here.

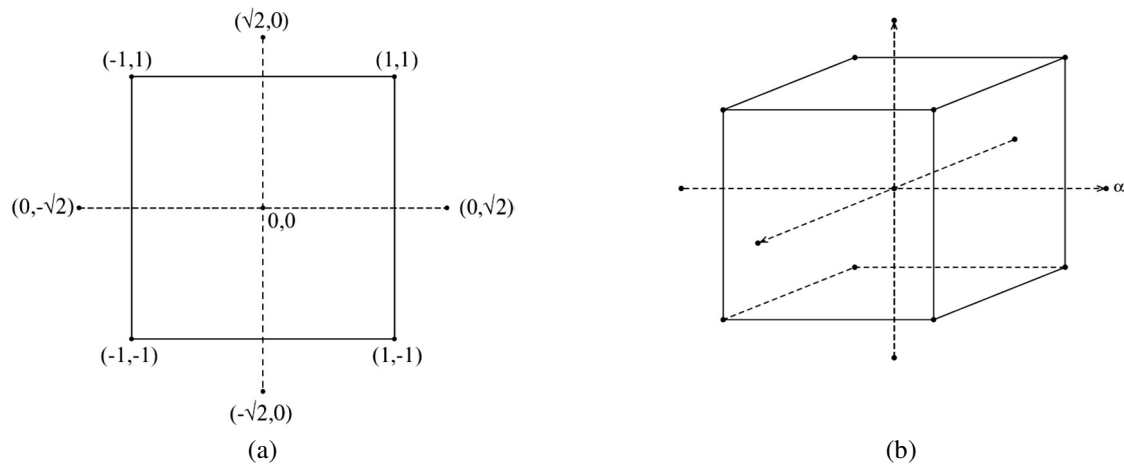


Figure 56 Schematic diagrams of central composite design for (a) $n=2$ and (b) $n=3$

6.2.3 Latin Hypercube Design

Latin hypercube sampling (LHS) is a statistical method for generating a near-random sample of parameter values from a multi-dimensional design space. The sampling method can be used to construct computer experiments for different disciplines of science, or even for use in Monte-

Carlo simulations. The LHS was first described in 1979 (McKay et al., 1979) and was further developed in the following decades (Iman et al., 1981; Tang, 1993; etc.).

In statistical sampling, a square domain containing sample positions is called a *Latin* square if there is only one sample in each row and each column. A Latin hypercube is the generalization of this concept to an arbitrary number of dimensions, where each sample is the only one in each axis-aligned hyperplane containing it. When sampling a function of n variables, the range of each variable is divided into m equally probable intervals. The number of m sample points are then placed to satisfy the Latin Hypercube requirements.

Note that within each hypercube (or: cell), there exists only one sample, and the exact value of each of its variables is determined randomly. Furthermore, within the family of LHS design, there are different methods. In a fully-random LHS, one cannot completely control the distribution of the data points within the design space. Therefore, there is a chance of seeing large ‘holes’ in the domain. To overcome this issue, LHS design is typically accompanied by a procedure that will optimize it to avoid large holes. Figure 57 compares two designs with 9 points. The left distribution is a fully random LHS, and the right one is an LHS optimized to maximize the minimum distance between points. Note the random LHS design has substantial empty regions near the top right and bottom left corners, while the optimized LHS design has a more uniform coverage. Different software packages use different techniques to optimize the configuration of the design space. For instance, in MATLABTM, the *lhsdesign* command that is used for generation of an LHS design space can be called with three different ‘criterion’ flags, i.e., *maximin* (which maximizes the minimum distance between points), *correlation* (which attempts to reduce the correlation between all the data points, so they are not following an obvious trend, such as a linear or quadratic curve), and *none* (Mathworks, 2017).

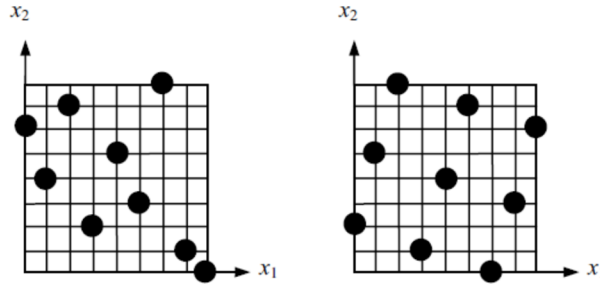


Figure 57 An LHS design with 9 total points

6.2.4 SHERPA Optimization Algorithm

SHERPA is a proprietary hybrid and adaptive optimization algorithm that is developed by *Red Cedar Technology*, and is available in their design optimization tool HEEDS. Since the acquisition of Red Cedar Technology by CD-adapco in 2013, HEEDS has been included within the Optimate+ module of Star-CCM+ package. SHERPA stands for “Simultaneous Hybrid Exploration that is Robust, Progressive and Adaptive”. Since it is a hybrid method, during a single search, SHERPA examines a variety of available search algorithms simultaneously, and decides on which specific method to use during that particular step of the search. This algorithm takes advantage of the best attributes of each method, and reduces a method’s participation in the search if and when it is determined to be ineffective. Some of the algorithms used within the SHERPA framework are genetic algorithm, simulated annealing, nonlinear sequential quadratic programming, and response surface method, which are all among the most commonly used optimization methods.

In SHERPA, a combination of global and local search methods is used, with the number of different methods used at any step being anywhere between two and ten. Each individual method contains tuning parameters that are modified *automatically* over the course of the search based on the information gained about the nature of the design space. This evolving knowledge about the design space also determines when and how much each method should be used. In other words, SHERPA efficiently learns about the nature of the problem and adapts to it. It is shown in

the developer's white paper (Red Cedar Technology, 2017) that this method can work more efficiently than several other non-hybrid optimization algorithms for the problem of optimizing the cross-section of an I-beam to deliver a minimum mass, while satisfy stress and deflection constraints. One benefit of this method is its very low user demand, i.e., the user does not need to have much knowledge about the design space, or know about any tuning parameters. The user only needs to provide the total number of evaluations for the optimization study.

There are several other studies reported in the literature that have utilized this methodology, including multi-objective optimization of a gas turbine combustor design (Maurya et al., 2014), optimization of natural convection heat suppression in a solar cavity receiver with plate fins (Ngo et al., 2015), and investigation of the global minima for five benchmark mathematical problems such as Goldstein-Price and Rosenbrock's Valley functions (Chase et al., 2015).

Note that due to proprietary nature of SHERPA, no further details regarding the exact criteria for switching between the individual optimization methods at each step are available online.

6.3 DoE Problem Description

As discussed previously, there are five main geometrical parameters that need to be examined in terms of their influence on lift or LoD. A step-by-step approach is followed, where three pairs of variables, i.e., L_1 & w , β_1 & β_2 , and L_1 & h are investigated one after another, and response surfaces best fitting the set of data are created for each study. The ranges chosen for each variable is presented in Table 6.

Variable	Min	Max
First-leg length, L_1/c	0.15	0.85
Width, w/c	0.0025	0.02

Inlet angle, β_1	90 deg	96 deg
Exit angle, β_2	15 deg	85 deg
Vertical position, h/c	0.04	0.07

Table 6 Ranges of the values taken by five geometrical variables in the DoE study

The procedure for setting up a DoE study in Optimate+ environment is briefly outlined below:

- Specify the type of study (Design Sweep, DoE, or Optimization)
- Define the independent variables with their respective ranges
- Define the objective function, the goal (maximize vs. minimize) and constraints (if applicable)
- Decide on the number of studies or evaluations, number of CPU cores, and number of simultaneous jobs running
- Perform individual CFD simulations, and post-process the data when all simulations are finished

For each study/evaluation, the main Star-CCM+ solver is called with the specified values for the independent variables (which are typically geometrical parameters, but other variables such as inlet velocity value, and AoA are allowed as well), a new mesh is generated, solution is initialized, and the governing equations are solved until the desired convergence level is achieved for all of the quantities of interest. Note in addition to the typical monitored quantities (continuity, x -momentum, y -momentum, z -momentum, and turbulent kinetic energy TKE) which all had the convergence criterion of 1E-6, two additional quantities (lift force and LoD) were monitored. Those two new quantities were assigned *asymptotic* stopping criterion, meaning that maintaining the amplitude of fluctuation of less than 0.05 (with the units of N for lift, and

dimensionless for LoD) over the past 200 iterations would mean a convergence. These two new criteria were conjoined bitwise (ANDed) with other existing stopping criteria.

For the current studies, the study type was set to Design of Experiment with Latin Hypercube method (the other available options were two-level and three-level factorial designs), the objective function was set to LoD, and the goal was set to *maximize*. Number of studies were either 10 or 12, number of CPU cores was set to 10 (for a desktop workstation with 12 Intel® Core™ i7-5930K cores, each with 3.50 GHz speed, and with 32.0 GB RAM), and the number of simultaneous jobs was set to 1. Note that the minimum number of evaluations for a valid DoE study with n variables in $(n+1)(n+2)/2$, which would be 6 for studies with two variables. Figure 58 shows two of the sample LHS designs in the 2D spaces created for the forthcoming DoEs. One can note the random distribution of the data points in both domains.

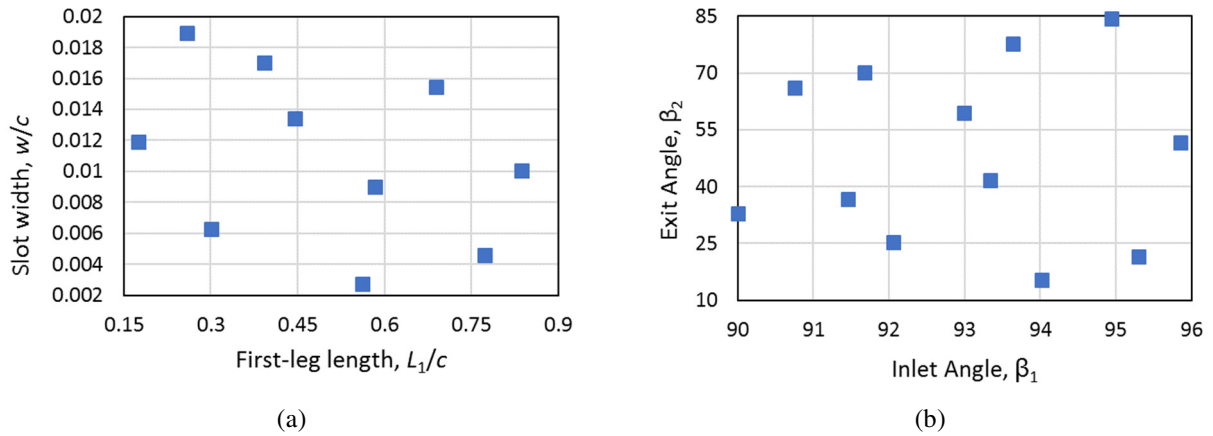


Figure 58 Distribution of the data points in the current DoE study for (a) 10 evaluations considered for L_1 & w study, and (b) 12 evaluations considered for β_1 & β_2 study

6.4 Results and Discussions

The results of the DoE studies on a NACA 4412 slotted airfoil with five main geometrical variables is presented in the following subsections. Operation at two AoAs and two Reynolds numbers are investigated.

6.4.1 DoE at $Re=1.6E6$ and $AoA=6$ deg

The AoA of 6° is chosen because it is where the peak of the LoD vs. AoA curve is located (Burton et al., 2011). Moreover, for wind turbines tested previously at UWM wind tunnel lab, the effective AoA has generally been in the $6^\circ \pm 2^\circ$ range.

6.4.1.1 Slot's width and the first-leg length

The first set of response surfaces (RS) belongs to lift force and LoD for dimensionless first-leg length (L_1/c) and width (w/c). Results are presented in Figure 59. As the first-leg length increases, the lift force increases. This is mainly because within the slot, the pressure of the top surface is slightly greater than that of the bottom surface, possibly due to the impingement effect of the entering air stream. As L_1 increases, so does the overall surface area, and that causes having a larger net upward force in longer slots compared to shorter ones. However, the trend of width is somewhat dependent on the length. For shorter slots, lift force increases with slot's width. But as the length increases, there seems to emerge a peak in the lift vs. width curve.

As shown in part (b) of the same figure, LoD surface has a very different trend compared to the lift force. The only firm conclusion that can be made is that LoD increases as the width decreases. Length, however, shows different behavior at different L_1 value. For large and medium widths (where the LoD values are not desirable), there seems to be a valley (local minimum) in LoD vs. L_1 curve. As width decreases and more suitable LoD values are achieved, LoD seems to be only weakly dependent on L_1 , and in some cases, there exist local maxima in $L_1/c=0.2\sim0.4$, depending on the width. If the objective function is LoD, it is hence recommended to keep the width small, and set the length based on the practical issues and other constraints.

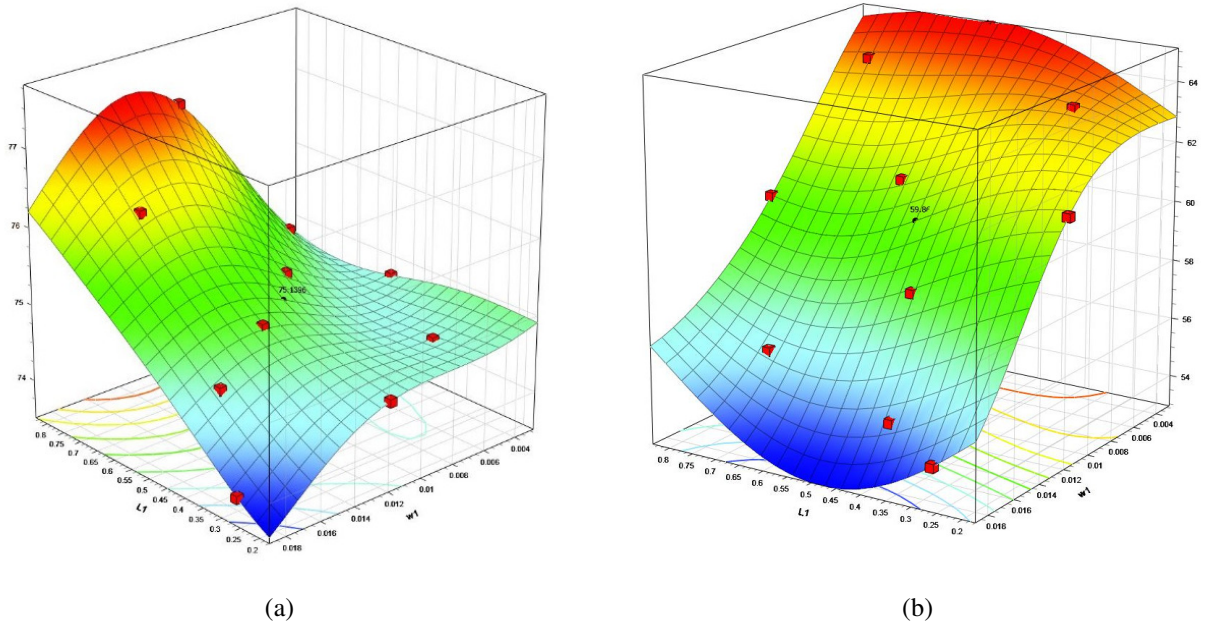


Figure 59 Response surfaces fitted to (a) lift and (b) LoD data points for a DoE study on L_1/c and w/c

6.4.1.2 Slot's inlet and exit angles

The RSs fitted to the lift and LoD data points of the DoE study on β_1 and β_2 are presented in Figure 60. The general trend is that as the exit angle (labeled as 'AngleL2' in the same figure) decreases (which means streams leaving slot become more aligned with the main stream flowing below the airfoil), both lift and LoD consistently increase. The inlet angle (AngleL1), however, does not seem to be very influential in determination of either lift or LoD. After a closer look, one might decide to keep the inlet angle closer to 90 (which means horizontal first-leg) or 92, as it provides slightly higher LoD.

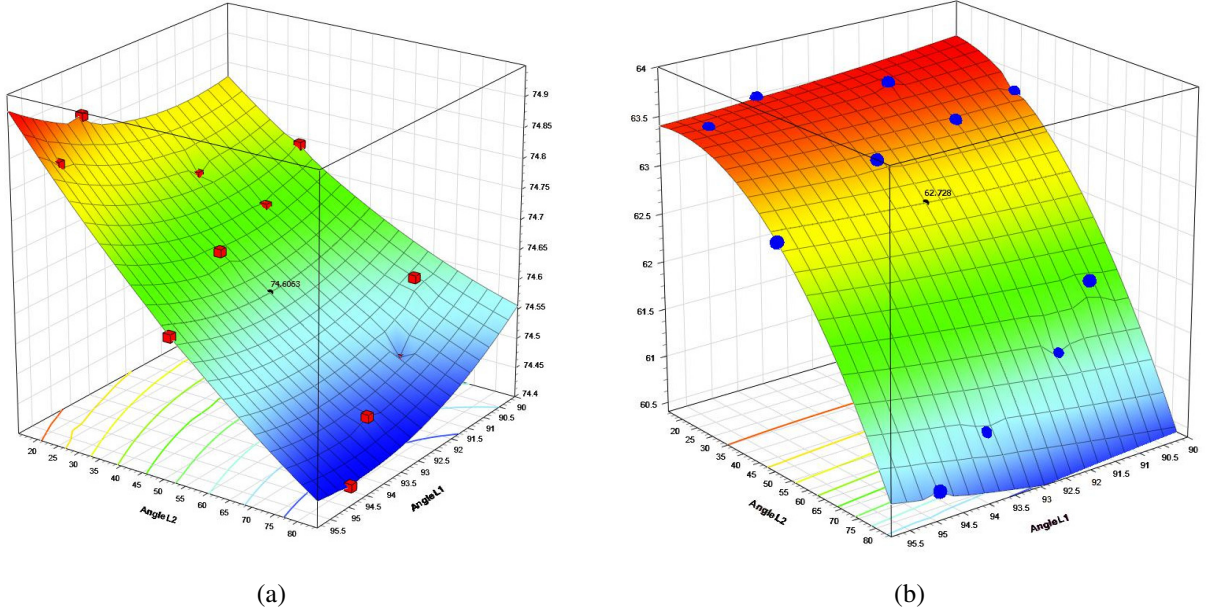


Figure 60 Response surfaces fitted to (a) lift and (b) LoD data points for a DoE study on β_1 and β_2

6.4.1.3 Slot's vertical position and the first-leg length

Out of the four variables investigated so far, it seems L_1 and β_2 can result in more pronounced changes in lift and LoD. In Figure 61, results of another DoE study on L_1 and the final variable of interest h is presented. As was determined previously in Figure 59, lift generally increases with the first leg length. Also, depending on the chosen length, the lift force either increases continuously with h , or reaches a maximum and flattens out afterwards. LoD, on the other hand, shows a different trend. The RS fitted indicates that for any length value considered, there exists a peak in the LoD vs. h curve, somewhere in the mid-range. This optimal value mildly decreases as L_1 increases. Therefore, the value of h/c around 5~6% as found previously seems to be an appropriate choice. As shown below, this RS has a local (not global) minimum, corresponding to medium to large L_1 values and medium to large h values.

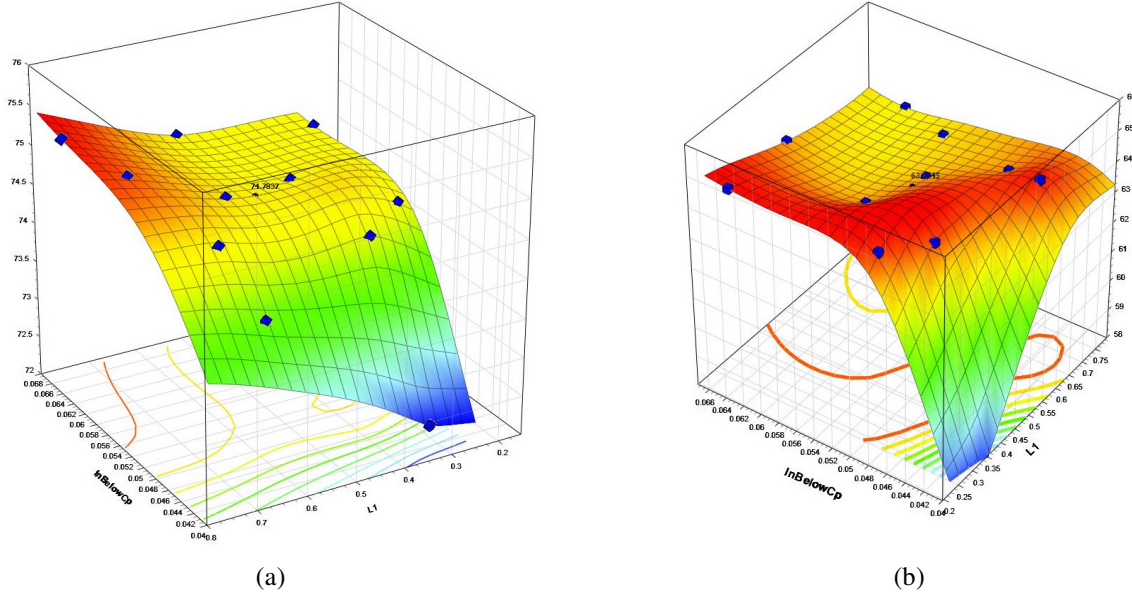


Figure 61 Response surfaces fitted to (a) lift and (b) LoD data points for a DoE study on L_1/c and h (labeled as $h_{BelowCp}$ in the figure)

6.4.1.4 Optimization using SHERPA

The main take-away of the three DoE studies reported above is that the three most influential geometrical variables are L_1 , h , and β_2 . Moreover, by properly choosing those variables, an LoD up to ~65 can be extrapolated from the fitted RSs for a slotted airfoil at $AoA=6$ deg. Note the LoD of the solid airfoil counterpart is only around 59, so there is at least 10% improvement in LoD, if the slot parameters are chosen properly. To seek a more optimal solution, SHERPA optimization algorithm is utilized as well. The ranges of the five variables of interest are determined after taking into account the following two issues:

- From the three DoE studies carried out earlier, the more appropriate and narrower ranges of the 5 variables resulting in the largest LoD values are identified. Those ranges are used as guidelines to determine the ranges to use for the optimization routine.
- Before specifying the lower and upper bounds of each variable, the actual geometry of the slot within the airfoil was generated in Star-CCM+ and reviewed carefully. In some

occasions, those ranges were further confined to ensure the slot “fits” properly in the airfoil, and no undesirable geometrical deformation can occur.

The final ranges of the 5 variables considered in this study are presented in Table 7. Also shown is the *Resolution* that indicates the number of discrete values of each variable uniformly spaced between the respective minimum and maximum values. Note the resolution for width is significantly less than the rest of the variables, as it was shown repeatedly in preliminary studies that the optimum width is near the lower bound considered. The total of 40 evaluations (each with a different design ID) were decided and the optimization routine was started.

The convergence criteria for individual CFD simulations were set to be the same as those used for the DoE studies. As shown in Figure 62, the algorithm starts with a relatively small LoD for the first few designs. However, after about 14 evaluations, it reaches the maximum LoD of 65.4, which is slightly better than what predicted by DoE. From that point on, the algorithm perturbs the independent variables one after another in an attempt to seek a better design. However, most of the following designs result in LoDs between 64 and 65.3, which can ensure us that the maximum LoD point is achieved. A closer look at the design IDs with highest LoDs reveals that they all have relatively small length, small width, small β_2 , and mid-range h and β_1 values. It is now recommended to repeat the optimization algorithm for a slotted airfoil under different operating condition.

Variable	Min	Max	Resolution
First-leg length, L_1/c	0.15	0.65	201
Width, w/c	0.005	0.009	33
Inlet angle, β_1	0 deg	6 deg	81
Exit angle, β_2	18 deg	80 deg	125

Vertical distance, h/c	0.046	0.07	201
--------------------------	-------	------	-----

Table 7 Range of the values taken by five geometrical variables in the SHERPA optimization study

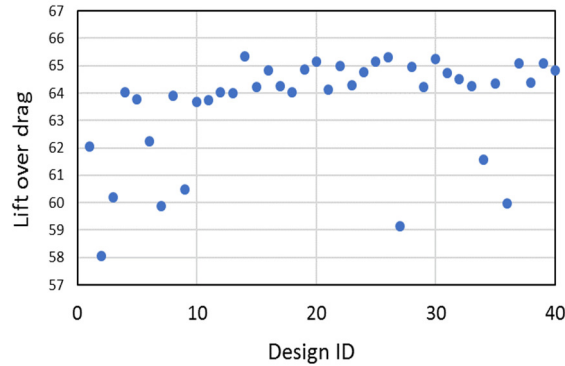


Figure 62 The objective function LoD monitored in the optimization study with a maximum of 40 evaluations

6.4.2 DoE at $Re=1.6E6$ and $AoA=8$ deg

To check the effect of AoA on the behavior of LoD as a function of the five main variables, the DoE studies of the previous section are repeated at $AoA=8$ deg. The statistical analysis software package, TableCurve 3D v4.0 is used for this purpose. CFD simulations with different geometrical configurations are executed one after another in Star-CCM+, and then the converged values of lift, drag, and LoD are imported in TableCurve to create the response surfaces. Figure 63 shows the RSs fitted to the three sets of data. Comparing the results with those obtained for $AoA=6$ deg reveals a similar behavior. For instance, smaller widths definitely result in higher LoD, while length does not seem to have much of an influence. Referring to part b of the same figure, again, the smaller exit angles are more suitable, while the inlet angle may or may not yield an optimum value. Finally, the LoD vs. h curve seems to be very steep in the smaller value, but then it shows a somewhat optimum value near the midpoint, roughly around $h/c=0.055$, which is consistent with the previous findings. These results confirm the scalability of $AoA=6$ results.

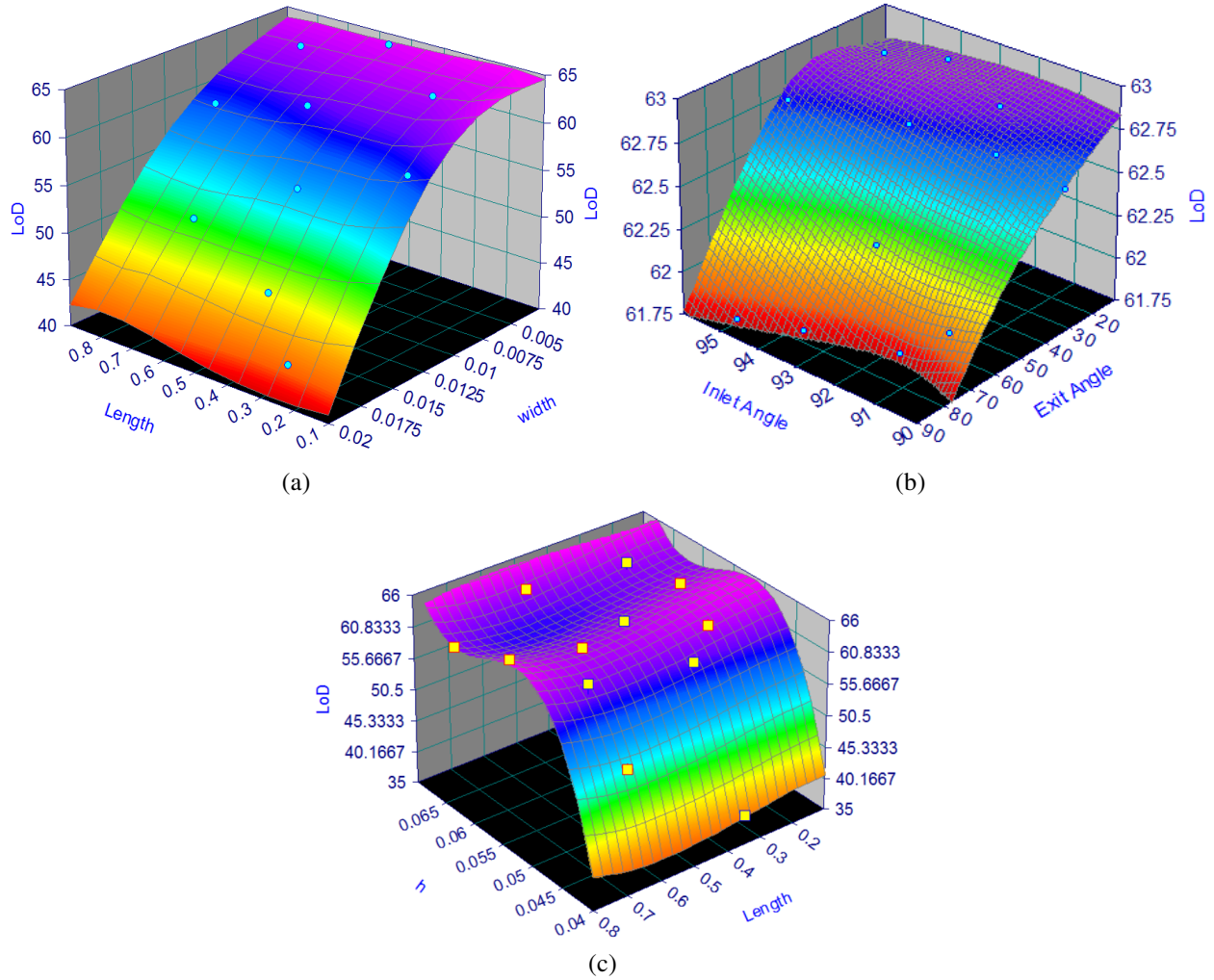


Figure 63 Response surfaces fitted to LoD data points for a DoE study with $Re=1.6E6$ and $AoA=8^\circ$ on (a) L_1/c and w/c , (b) β_1 and β_2 , and (c) L_1/c and h/c

6.4.3 DoE at $Re=3.2E6$ and $AoA=6^\circ$ deg

Effect of Reynolds number on the overall predictions is studied briefly here. The baseline AoA of 6° is considered along with a Reynolds number, twice as large as the baseline Re. In Figure 64, only the LoD surfaces are shown for the three DoE studies similar to the previous sections. As shown in part a of this figure, the dependence of LoD on L_1 and w is very similar to what observed in previous sections for $AoA=6^\circ$. That means LoD consistently increases as w increases, but it is not a very strong function of L_1 . Similarly, the inlet and exit angles seem to have similar effects to what they showed for $AoA=6^\circ$, e.g., in Figure 63b and Figure 60b. As for the dependence of LoD on L_1 and h (Figure 64c), there seems to be some disagreement with the

previous cases. Although h has an optimal value, it appears that the low values of L_1 are no longer very suitable. In other words, depending on the h/c chosen, perhaps L_1 values between 0.3~0.4 may be more appropriate. Nonetheless, there seems to be a general similarity between the findings of the high- Re case with the baseline case.

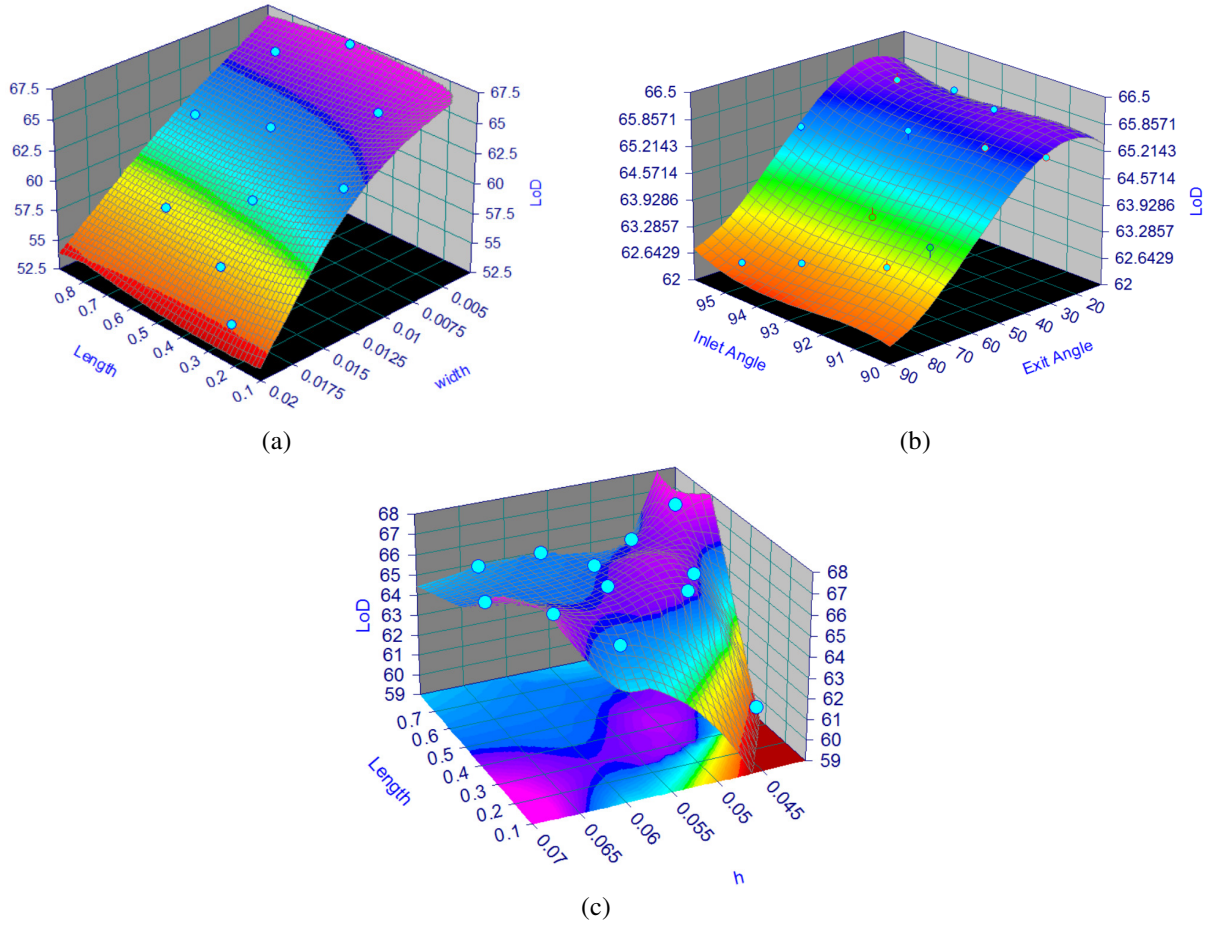


Figure 64 Response surfaces fitted to LoD data points for a DoE study with $Re=3.2E6$ and $AoA=6^\circ$ on (a) L_1/c and w/c , (b) β_1 and β_2 , and (c) L_1/c and h/c

6.5 Conclusion

In this chapter, the parametric study on the five main geometric parameters of the slot was taken to the next level by considering the simultaneous effect of two or more variables on lift force and the lift-over-drag ratio, LoD. Some of the common methods of DoE were briefly introduced and the method of Latin Hypercube Sampling was further described. Three DoE

studies each with two independent variables were defined, and the random data points in the design space were identified. Simulations were carried out for $Re=1.6E6$ and $AoA=6$ deg. For those DoE studies, it was concluded that while slot width and inlet angle are not very influential, the proper selection of the three remaining variables, i.e., L_1 , β_1 and h can have a significant impact on both lift and LoD. The DoE studies were followed by a full-blown optimization routine on all 5 variables, with slightly modified ranges. It was determined that a similar maximum LoD can be achieved by using an optimization algorithm.

The DoE study was repeated for the case of $AoA=8^\circ$ and $Re=1.6E6$, and another case with $AoA=6^\circ$ but with $Re=3.2E6$. In general, the results from the three cases were similar, which shows the scalability of the findings. Gaining confidence about the robustness of the DoE and optimization studies conducted, it is recommended to repeat this procedure if the operation of different airfoils or different add-on features are to be studied.

Chapter 7 Slotted Wind Turbine Blade Analysis

7.1 Introduction

In the previous sections, flow around and through a limited-span slotted airfoil was studied. The influence of different geometrical parameters on lift and LoD was investigated. To study the feasibility of using slots on wind turbine blades, in the present chapter, a set of CFD studies are carried out on a laboratory-scale HAWT whose blades are equipped with a multi-segment slot that covers a large portion of the blade span. Operation of the wind turbine under two different operating conditions (with different rotation rates and incoming air velocities) is investigated. Results are compared against those obtained from a study on a similar HAWT with solid airfoils (without any slot). Moreover, the estimated mechanical power for each case is compared with the data collected from a wind tunnel test on the same wind turbine.

7.2 Problem Description

Figure 65 shows the computational domain and the blade used for the analysis of turbulent air flow around a three-blade slotted HAWT. To save on the computational cost, only one-third of the long cylindrical domain (a 120-deg sector) is modeled, where a single slotted blade attached to one-third of the hub is mounted on the centerline. Air with a uniform axial velocity enters the domain from the left boundary, it passes around and through the blade, and leaves the domain from the right surface. Same analysis is done for a baseline *solid* blade.

The velocity of the entering air is set to either 5.3 or 7.7 m/s, and the rotational speed of the blade is 80 or 167 rad/s. These combinations of the input values were chosen due to three main reasons: (a) to deliver a reasonable and common TSR, (b) to result in the effective AoA of around 6 degrees, corresponding to the peak of the LoD vs. AoA curve, and (c) to match with the

operating conditions used in a previous experimental study (Alsultan, 2015), so as to compare the results.

As explained in section 2.2 of the dissertation, the effective AoA of a rotating blade at every spanwise location is dependent on several independent variables, and is determined by using an iterative procedure. Table 8 shows the converged values of AoA, and the two induction factors a , a' for the case of $U_{in}=7.7$ m/s and $\omega=167$ rad/s for three spanwise locations along the blade. Note the input values were chosen such that TSR is at a near-optimal value of 6.7. As shown below, the final values of AoA are centered around 6 degrees, which is the desired value. Moreover, the final values of a are very close to 1/3, which is the ideal theoretical value, per Betz' calculations (Burton et al., 2011). For each case, there were approximately 10 iterations needed before the final values were achieved.

Inputs						Converged Outputs		
U (m/s)	Twist Angle (°)	ω (rad/s)	TSR	r/R	chord (m)	a	a'	Effective AoA (°)
7.7	15.0	166.42	6.7	0.25	0.048	0.352	0.082	5.06
7.7	5.1	166.42	6.7	0.5	0.023	0.316	0.016	6.25
7.7	1.5	166.42	6.7	0.75	0.016	0.315	0.007	6.46

Table 8 The converged calculated effective AoA and induction factors at three spanwise locations along a rotating blade ($R=31$ cm)

As before, the airfoil profile chosen for the blade is NACA 4412 throughout the span, and the blade is equipped with four equal-length slots drilled along the span. A close view of the slotted blade CAD model is provided in Figure 65, while the laboratory-scale wind turbine made with 3D-printed slotted blades is depicted in Figure 33. The total length of the blade R is 31 cm, with the maximum chord length of 5.1 cm near the hub, and with the maximum twist angle of 43.74° at the hub, and 0.56° at the tip.

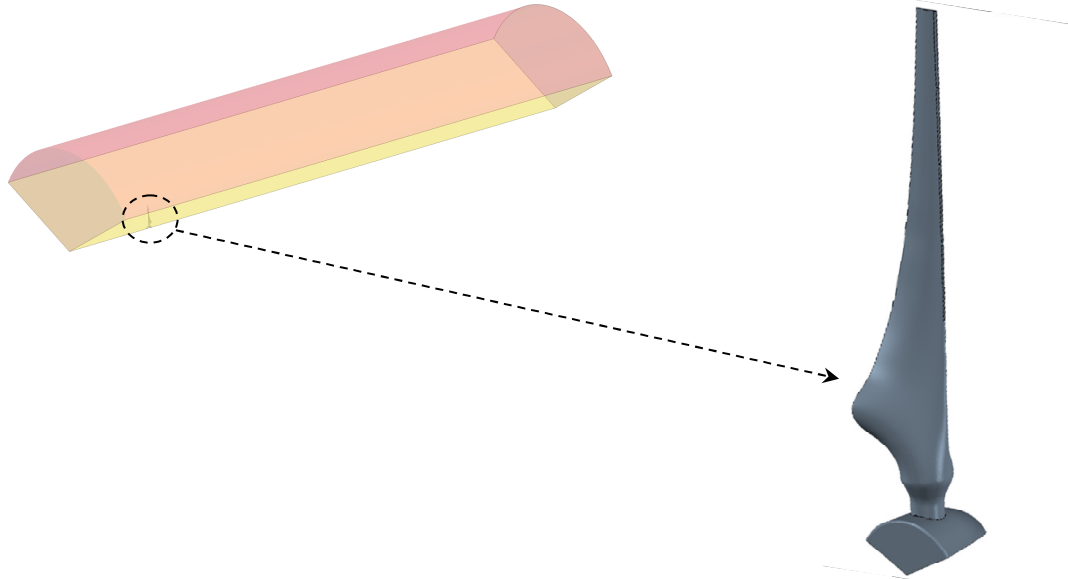


Figure 65 Computational domain chosen for study of the slotted wind turbine blade: (left) the one-third cylindrical domain, and (right) the CAD model of the slotted HAWT blade

7.3 Model and Mesh Setup

As shown in Figure 66, the *velocity inlet* boundary condition was imposed at the inlet boundary as well as the ‘top’ boundary (with the direction being normal to the inlet boundary), and the turbulent intensity of 1%. *Pressure outlet* boundary condition was assigned to the outlet surface, where the gauge pressure was set to 0. The two side surfaces of the 120-degree domain were given periodic BCs. Moreover, for steady-state RANS-based $k-\omega$ simulations, a moving reference frame function in Star-CCM+ was considered in the calculations, so as to implement the rotation of the domain, and to avoid using more complicated strategies such as the sliding mesh. In other words, the blade was considered stationary, and the entire fluid region was given a rotational velocity component. Note for unsteady simulations, Rigid Body Motion was considered.

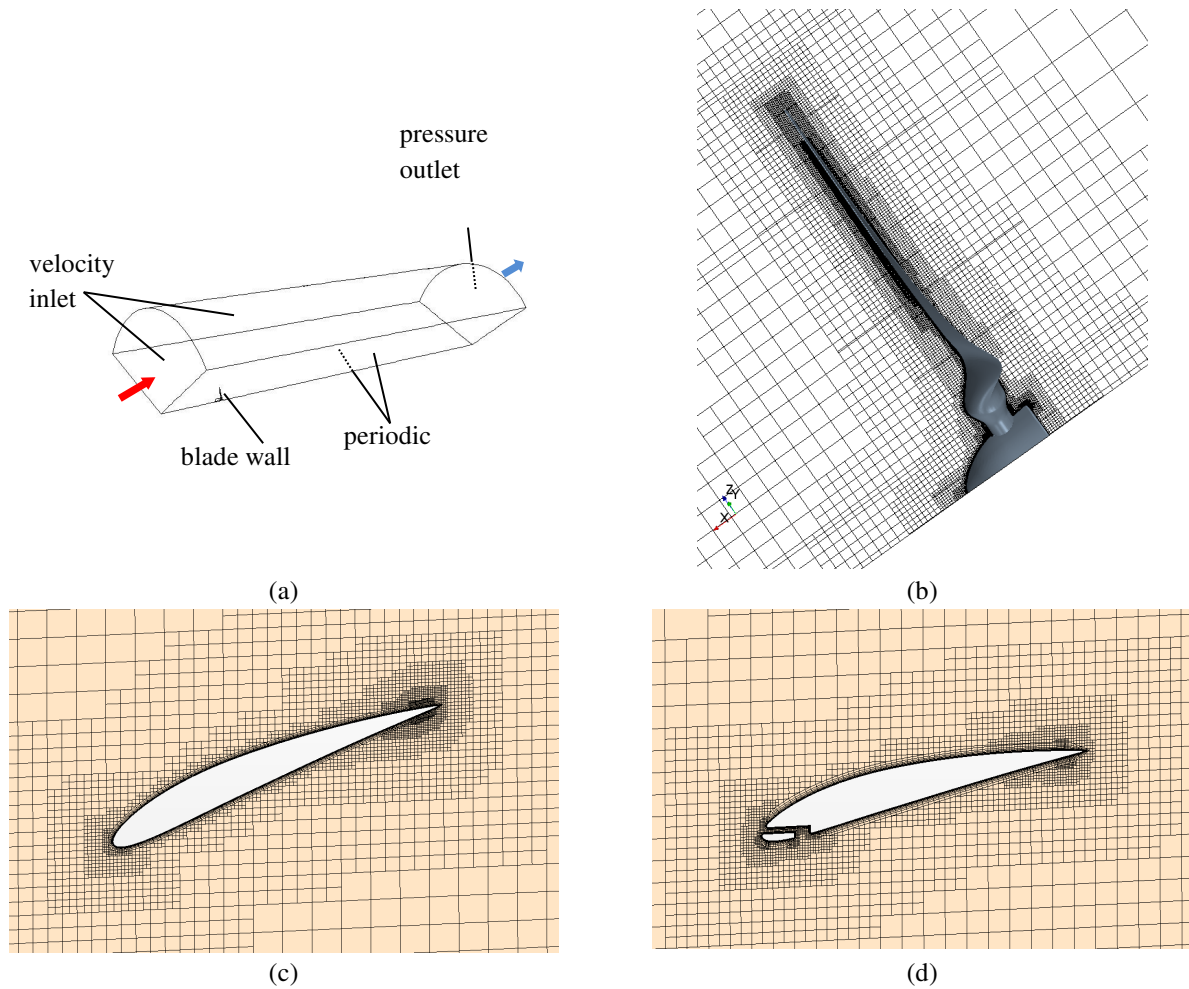


Figure 66 (a) Schematic diagram of the computational domain and the BCs, (b) near-blade grid structure at a cross-section covering the entire blade span, (c) near-blade grid structure at a cross section located at one-third of the blade height, and (d) near-blade grid structure at a cross-section located at two-third of the blade height

Grid generation was accomplished in Star-CCM+. A Structured Mesh strategy (called *Trimmer*) with hexahedral element type was employed throughout the domain, and the near-wall surfaces were given additional 10 prism layers (with the growth ratio of 1.3) to properly refine the mesh. The thickness of the first layer of the cells off the solid surfaces was selected such that the average y^+ of ~ 0.36 is observed near the blade and hub surfaces. The total number of elements was $\sim 7.97\text{M}$. Three different views of the mesh generated near the blade surface are provided in parts b, c, and d of Figure 66. Furthermore, distribution of the converged y^+ on the blade surface after a LES study is displayed in Figure 67.

For steady simulations, the $k-\omega$ SST turbulence model was employed for resolving the turbulent terms in the momentum equation. A coupled solver with Bounded-Central discretization in space was used for both steady and unsteady simulations. For unsteady simulations, LES with WALE (Wall-Adapting Local Eddy-viscosity) sub-grid scale model (Nicoud and Ducros, 1999) was used. The time-step size was set to $2 \mu s$, and a second-order temporal discretization was employed.

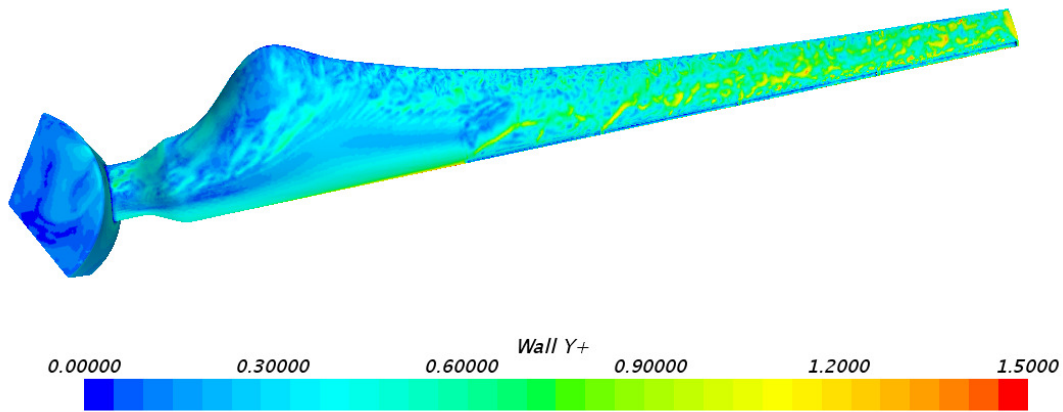


Figure 67 Distribution of y^+ on the surface of the blade and the hub

7.4 Results and Discussions

7.4.1 Velocity and Pressure Distribution

The following figures show the distribution of velocity and pressure contours at different cross-sections of the domain. In Figure 68, distribution of pressure at a cross-section of the blade located at approximately one half of the blade length is investigated. Due to the slot configuration, there seems to be two distinct stagnation points, one at the expected location (airfoil *nose*), and the other one inside the slot. The overall distribution of pressure around the blade is reasonable, with higher values observed on the bottom surface, and lower values seen on the top surface.

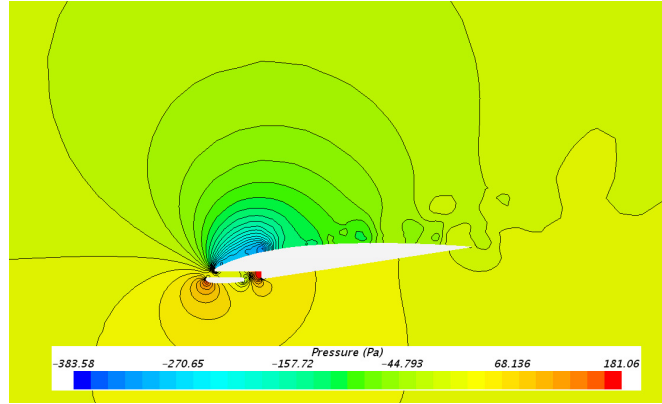
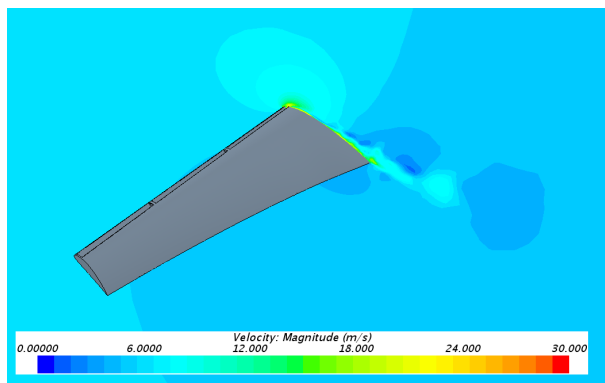
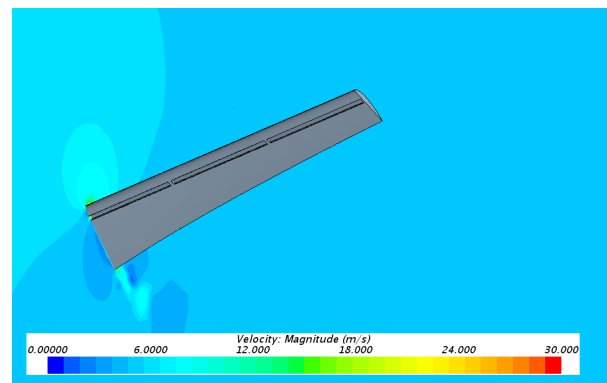


Figure 68 pressure distribution at a radial cross-section of the blade at about one half of the blade length after 3.0s of the operation

Similarly, the contours of velocity magnitude at two different sections of the domain is shown in Figure 69. Parts a, b, and c of the figure show distribution of velocity in the near blade region, at a radial cross-section located at approximately one-half of the blade length. The separation region on the suction-side can be easily detected. Also, note the large velocity values for fluid flow through the slot. In Figure 69d, the velocity contours on a vertical mid plane are shown (note the instantaneous position of the blade, which is out of the plane). As expected, the velocity deficit is clearly observed downstream of the blade. After a certain distance downstream of the blade, flow velocity recovers.



(a)



(b)

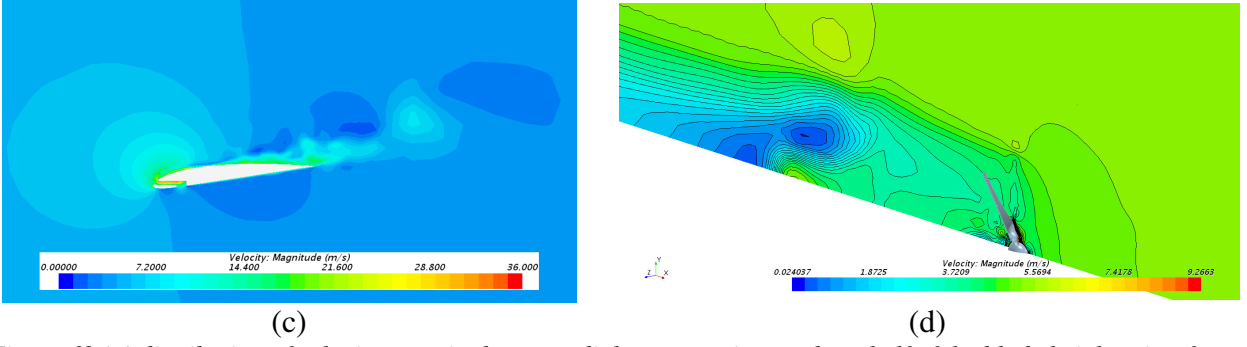


Figure 69 (a) distribution of velocity magnitude at a radial cross-section at about half of the blade height; view from the top of the blade, (b) same as part a, but view from the bottom of the blade, (c) same, showing the entire near-blade region, and (d) velocity contours at a vertical mid-plane of the domain

7.4.2 Torque and Power

The mechanical torque (or moment) generated by the wind turbine blade is calculated by the solver and the steady-state value is obtained. For operation with the inlet velocity U of 5.3 m/s and the rotational velocity ω of 80 rad/s, as well as for the case with $U=7.7$ m/s and $\omega=167$ rad/s, the torque and the corresponding mechanical power - as defined in Eq. (3.22)- are calculated for both solid and slotted blades, and the results are presented in Table 9. Also presented are the electrical power generation measured in a wind tunnel study at UWM with a matching-size wind turbine and very similar operating conditions (Alsultan, 2015; Appendix Tables therein). Those electrical power values are obtained for several different values of the resistive load applied in the electrical circuit. The resistances between 0.2Ω - 2Ω were tested. As shown in Table 9, there is a good agreement between the CFD predictions and the experimental data for both solid and slotted blades. The CFD values are slightly larger, which can be attributed to different sources of power loss in the experimental setup, such as the mechanical losses due to the blade surface roughness, and losses in the generator, wiring, and connections. It is confirmed from *both* CFD and experimental studies that the slotted blade consistently generates more torque and power as compared to the solid blade.

	Case	Torque (CFD) [N.m]	Power (CFD) [W]	Power (Expt.) [W] Avg. (min , max)
U=5.3 m/s & $\omega=80$ rad/s	Solid blade	0.0258	6.19	4.12 (1.69 , 8.13)
	Slotted blade	0.0281	6.72	5.07 (2.07 , 10.37)
U=7.7 m/s & $\omega=167$ rad/s	Solid blade	0.067	33.56	17.86 (6.88 , 31.90)
	Slotted blade	0.075	37.57	18.80 (6.21 , 33.93)

Table 9 Torque and the power generated from both CFD and wind tunnel experiment

7.5 Conclusion

In the present chapter, leading-edge slots were drilled in the blades of a laboratory-scale HAWT. CFD simulations were carried out for a solid and a slotted blade. The pressure and velocity contours at certain locations in the near-blade region for the slotted case were presented. The torque generated by the blade as a results of the pressure and shear forces on the blade surface were calculated and reported for each case. It was determined that for an operating condition typical for a small wind turbine rotating inside the UWM wind tunnel, the slotted blade generated approximately 10% higher torque and power. The results were also compared against the experimental measurements made during wind tunnel studies on solid and slotted HAWTs running under the same operating conditions. There is an acceptable agreement between the trends of the two sets of results. While other operating conditions and other slot configurations can be studied in future, the current findings prove the concept of using leading-edge slots for application on wind turbines.

Chapter 8 Overall Conclusions and Recommendations

In the present dissertation, the feasibility of using a novel hybrid turbulence model along with application of a geometrical alteration on airfoils was studied comprehensively. As the first part of this study, the possibility of improving near-wall predictions of CFD simulation in the near-solid-surface region of a flow domain by using a modified turbulence model was examined. Algebraic Stress Model (ASM) was introduced as a modification of RSM. It was first shown that the proposed model replicates the results of fully-converged RSM for the problems of 2D flow over a flat plate, and 3D flow around a rotating wind turbine blade. Then, this model was carefully combined with a hybrid LES-RANS scheme (i.e., DES) within the framework of Star-CCM+ software package by developing an additional MATLAB code. For the problem of turbulent flow around a limited-span airfoil, it was shown that the proposed model could show a slightly better performance as compared to the baseline DES for prediction of near-wall velocities and surface pressure. More details on this model are provided elsewhere (Beyhaghi and Amano, 2017c).

In the second part of the dissertation, one special type of geometrical modification for wind turbines and airfoils, i.e., leading-edge slot was investigated through numerical simulation and laboratory experiments. Although similar slots were designed and employed for aircrafts, a special slot with a reversed flow direction was drilled in the leading edge of a sample wind turbine airfoil to study its influence on the aerodynamic performance. The slot configuration was determined by its five main design parameters, i.e., the first-leg length, slot's width (which was considered constant throughout the slot), inlet angle, relative exit angle, and the vertical location. Note there may be few other design configurations that one can investigate (such as applying

expansions at slot's inlet and exit planes, and single-leg slots), but they can be subject of future studies. The objective here was to vary the five main geometrical parameters of slot and characterize the performance improvement of the hybrid design under different operating conditions. First the lift and drag coefficients of the slotted airfoil with different combinations of length, width and the exit angle were studied at $AoA=0$. Despite the improvement in lift, all cases suffered from drag penalty. A similar (or even worse) behavior was observed at higher $AoAs$. As a result, slot was lowered in its entirety, and was assigned a mild upward tilt angle. The following numerical investigations revealed an improved performance over the entire range of AoA considered, mainly between 0-14 deg.

Later, the influence of all five parameters were examined in a series of single-variable parametric studies, and the corresponding pseudo-optimal values were obtained. The main conclusion was that by properly adjusting certain geometrical parameters of the airfoil, it is possible to reach a configuration that results in improved lift coefficient with respect to the baseline solid airfoil, *without sacrificing the drag*.

Next, a set of Design of Experiment studies and a multi-variable optimization were carried out, in which the geometrical variables were defined in reasonable ranges to seek the best design point. The objective function chosen was the aerodynamic efficiency of the airfoil, or lift-over-drag ratio. In future efforts, more complex objective functions can be defined after considering variables such as the additional weight associated with the required duct work, and the cost of installation and maintenance. These multi-variable parametric studies were only conducted at $Re=1.6E6$ and $3.2E6$, and only two $AoAs$ (6 and 8 deg), which are located at the peak of the L/D vs. AoA curve for NACA 4412 airfoil. The optimum values of different design variables were determined. Now that the optimization framework is implemented, one can repeat the procedure

for other combinations of Reynolds numbers and AoAs. Different optimization algorithms can also be investigated to find the sensitivity of the results to the method chosen. Moreover, the same procedure can be applied for the analysis of slots drilled in airfoils with different profiles.

As the final part of the dissertation, the leading-edge slot was drilled through a laboratory-scale horizontal-axis wind turbine blade (with span length of around 31 cm) made entirely with NACA 4412 airfoil profile. For structural reasons, four equal-length slots (as opposed to one long slot) each with the approximate length of 4.5 cm were drilled along the span, and the slotted blade was then analyzed. For the operating condition considered, around 8-12% improvement in the mechanical torque and power generation (compared to the baseline solid blade) was achieved. The calculated powers were also compared with the electrical power generated for a very similar 3D-printed wind turbine that was previously tested at UWM wind tunnel laboratory. A good agreement between the two data sets was observed, which again confirmed the validity of the CFD model and the results. Investigation of blades with different slot configurations and placement, or operation of the wind turbines with different air velocity and rotation speeds could be subject of future studies.

To summarize, the main conclusions and novel findings of the present dissertation are listed as follows:

- (1) The turbulence model of full implicit ASM can properly replicate the near-wall Reynolds stress predictions made by the more computationally intensive model of RSM. This point is exemplified for the problems of flow over a flat plate, and flow around a rotating HAWT.
- (2) The method of DES is combined and augmented with the anisotropic RANS-based ASM model for the first time, and this new simulation method is applied to the problem of turbulent flow over a cambered airfoil at two distinct angles of attack. It is shown that the

proposed model can slightly improve the surface pressure coefficient and the near-trailing-edge velocity distributions on most of the locations investigated.

- (3) Application of slots near the leading edge of a NACA 4412 airfoil and properly varying the design parameters results in a consistent improvement in lift and lift-over-ratio under a wide range of angle of attack. For one of the best cases studied during the single-variable parametric study, a C_L improvement up to 15% is observed for AoAs between 0° – 16° , while the drag penalty is insignificant. There are other design configurations with maximum lift improvement of up to 60%, however those designs are accompanied with as much as 100% increase in drag. Note the optimum h/c is found to be around 5.5%–6% for several cases. The DoE and optimization studies for operation with $\text{AoA}=6^\circ$ and $\text{Re}=1.6\text{E}6$ reveal that an optimal slot (for maximization of LoD) needs to have its width, length, and exit angle to be set as small as practically possible, while the vertical position and the inlet angle have mid-range optimum values. Very similar behaviors are observed for operation under $\text{AoA}=8^\circ$ and $\text{Re}=1.6\text{E}6$, and $\text{AoA}=6^\circ$ and $\text{Re}=3.2\text{E}6$, and that shows the scalability of the results presented. The decision to make about the optimum design parameters highly depends on the objective function.
- (4) Application of four leading-edge slots along the blades of a HAWT reveals that an improvement in torque and mechanical power generation of 8–12% can be achieved for two different operating conditions.

REFERENCES

- Abe, K., 2005, "A Hybrid LES/RANS Approach using an Anisotropy-resolving Algebraic Turbulence Model," *International Journal of Heat and Fluid Flow*, 26, pp. 204–222.
- Abbott, I. H., von Doenhoff, A. E., and Stivers Jr., L. S., 1945, "Summary of Airfoil Data," Technical Report No. NACA-824, Langley Memorial Aeronautical Laboratory, Langley Field, VA.
- Alfonsi, G., 2009, "Reynolds-averaged Navier–Stokes Equations for Turbulence Modelling," *Appl. Mech. Rev.*, 62(4), pp. 1–20.
- Alsultan, A., 2015, "Computational and Experimental Study on Innovative Horizontal-Axis Wind Turbine Blade Designs," Master's thesis, University of Wisconsin Milwaukee, Milwaukee, WI.
- Amano, R. S., Avdeev, I., Malloy, R. J., and Shams, M. Z., 2013, "Power, Structural, and Noise Performance Tests on a Different Wind Turbine Rotor Blade Design," *Int. J. Sustain. Energy*, 32(2), pp. 78-95.
- Amano, R. S., and Beyhaghi, S., 2015, "Use of Algebraic-Stress Model for determination of near-wall Reynolds-Stresses in turbulent flow over a flat plate," *AIAA Paper No. 2015-1890*.
- ANSYS, 2011, "ANSYS Fluent 14.5 User Manual," available at www.ansys.com.
- Antonello, M., and Masi, M., 2007, "A Simplified Explicit Algebraic Model for the Reynolds Stresses," *International Journal of Heat and Fluid Flow*, 28(5), pp. 1092–1097.
- Arce, C., Ragni, D., Probsting, S., and Scarano, F., 2015, "Flow Field Around a Serrated Trailing Edge at Incidence," *AIAA Paper No. 2015-0991*.
- Argyropoulosa, C.D., and Markatos, N. C., 2015, "Recent Advances on the Numerical Modelling of Turbulent Flows," *Applied Mathematical Modelling*, 39(2), pp. 693–732.
- ATI Industrial Automation, 2017, "ATI Force/Torque Sensors: F/T Models," available at http://www.ati-ia.com/products/ft/ft_ModelListing.aspx , retrieved 3/13/2017.
- AvStop (Aviation Online Magazine), 2015, "Forces on An Airfoil," available at <http://avstop.com/ac/flighttraininghandbook/forcesonanairfoil.html>, retrieved 6/15/2015.
- Belamadi, R., Djemili, A., Ilinca, A., and Mdouki, R., 2016, "Aerodynamic Performance Analysis of Slotted Airfoils for Application to Wind Turbine Blades," *Journal of Wind Engineering and Industrial Aerodynamics*, 151, pp. 79-99.
- Beyhaghi, S., and Amano, R. S., 2015, "Analysis of Turbulent Flow Around Horizontal Axis Wind Turbines Using Algebraic Stress Model," *ASME Paper No. IMECE2015-50686*.

Beyhaghi, S., and Amano, R. S., 2017a, “Improvement of Aerodynamic Performance of Cambered Airfoils using Leading-Edge Slots,” *Journal of Energy Resources Technology*, 139(5), pp. 051204-051204-8.

Beyhaghi, S., and Amano, R. S., 2017b, “Slotted Airfoils for Increasing the Aerodynamic Efficiency,” *AIAA Paper No. 2017-1839*.

Beyhaghi, S., and Amano, R. S., 2017c “Investigation of Flow Over an Airfoil Using a Hybrid Detached Eddy Simulation–Algebraic Stress Turbulence Model,” *Journal of Energy Resources Technology*, 139(5), pp. 051206-051206-9.

Bixler, G. D., and Bhushan, B., 2013, “Fluid Drag Reduction with Shark-Skin Riblet Inspired Microstructured Surfaces,” *Advanced Functional Materials*, 23(36), pp. 4507–4528.

Börner, T., and Alam, M-R., 2015, “Real Time Hybrid Modeling for Ocean Wave Energy Converters,” *Renewable and Sustainable Energy Reviews*, 43, pp. 784-795.

Bose, S. T., 2012, “Explicitly Filtered Large-Eddy Simulation: With Application to Grid Adaptation and Wall Modeling,” Ph.D. thesis, Stanford University, Stanford, CA.

Broeren, A. P., Addy, Jr. H. E., Bragg, M. B., Busch, G. T., Guffond, D., and Montreuil, E., 2011, “Aerodynamic Simulation of Ice Accretion on Airfoils,” *Technical Report No. NASA/TP—2011-216929*, Glenn Research Center, Cleveland, Ohio.

Burton, T., Jenkins, N., Sharpe, D., and Bossanyi, E., 2011, *Wind Energy Handbook*, Wiley, Chichester, West Sussex, United Kingdom.

CD-adapco, “Star-CCM+® Version 9.06 User Guide,” available at <http://www.cd-adapco.com/>

Chamorro, L. P., Tobin, N., Arndt, R. E. A., and Sotiropoulos, F., 2014, “Variable-sized Wind Turbines Are a Possibility for Wind Farm Optimization,” *Wind Energy*, 17(10), pp. 1483–1494.

Chase, N., Rademacher, M., Goodman, E., Averill, R., and Sidhu, R., 2015, “A Benchmark Study of Optimization Search Algorithms,” *Red Cedar Technology white paper BMK-3022*, East Lansing, MI.

Chen, C-J., and Jaw, S-Y., 1998, *Fundamentals of Turbulence Modeling*, Taylor & Francis, Washington, D.C.

Deardorff, J., 1970, “A Numerical Study of Three-dimensional Turbulent Channel Flow at Large Reynolds Numbers,” *Journal of Fluid Mechanics*, 41(2), pp. 453–480.

Divone, L. V., 1994, “Evolution of Modern Wind Turbines Part A: 1940 to 1994” *Wind Turbine technology, fundamental concepts of wind turbine engineering*, D. A. Spera, ed., ASME press, New York, Chap. 3.

National Institute of Science and Technology (NIST), 2017, “Engineering Statistics Handbook,” available at <http://www.itl.nist.gov/div898/handbook/pri/section3/pri3361.htm>

Ferrand, M., and Violeau, D., 2012, “A Family of Explicit Algebraic Models for Reynolds Stresses and Passive Scalar Fluxes,” *Journal of Hydraulic Research*, 50(5), pp. 494-505.

Franke, M., Wallin, S., and Thiele, F., 2005, “Assessment of Algebraic Reynolds-stress Turbulence Models in Aerodynamic Computations,” *Aerosp. Sci. Tech.*, 9(7), pp. 573-581.

Fuglsang, P., Antoniou, I., Dahl, K. S., and Madsen, H. A., 1998, “Wind Tunnel Tests of the FFA-W3-241, FFA-W3-301 and NACA 63–430 Airfoils,” Technical Report No. Risø-R-1041(EN), Risø National Laboratory, Roskilde, Denmark.

Gao, L., Zhang, H., Liu, Y., and Han, S., 2015, “Effects of Vortex Generators on a Blunt Trailing-edge Airfoil for Wind Turbines,” *Renewable Energy* 76, pp. 303 – 311.

Gatski, T. B., and Rumsey, C. L., 2002, “Linear and Nonlinear Eddy Viscosity Models,” *Closure Strategies for Turbulent and Transitional Flows*, B. E. Launder and N. Sandham, eds., Cambridge University Press, Cambridge, UK, 2002, pp. 9-46.

Gatski, T. B., and Speziale, C. G., 1993, “On explicit algebraic stress models for complex turbulent flows,” *Journal of Fluid Mechanics*, 254, pp 59-75.

Gomez-Elvira, R., Crespo, A., Migoya, E., Manuel, F., and Hernandez, J., 2005, “Anisotropy of Turbulence in Wind Turbine Wakes,” *Journal of Wind Engineering and Industrial Aerodynamics*, 93(10), pp. 797–814.

Gomez, C. A., Girimaji, S. S., 2014, “Explicit Algebraic Reynolds Stress Model (EARSM) for Compressible Shear Flows,” *Theoretical and Computational Fluid Dynamics*, 28(2), pp. 171–196.

Gupta, A., and Amano, R. S., 2012, “CFD Analysis of Wind Turbine Blade With Winglets,” ASME Paper No. DETC2012-70679.

Hanjalic, K., and Launder, B. E., 2011, *Modelling Turbulence in Engineering and the Environment: Second-Moment Routes to Closure*, Cambridge University Press, Cambridge, UK.

Hansen M. O. L., 2008, *Aerodynamics of Wind Turbines*, Earthscan, New York, NY.

Hastings, R. C., and Williams, B. R., 1984, “Studies of The Flow Field Near a NACA 4412 Aerofoil at Nearly Maximum Lift,” Technical Report No. ADA157750, Royal Aircraft Establishment, Farnborough, England.

Hellsten, A., Wallin, S., 2009, “Explicit Algebraic Reynolds Stress and Non-linear Eddy-Viscosity Models,” *International Journal of Computational Fluid Dynamics*, 23(4), pp. 349–361.

Hussein, M. S., Burra, K. G., Amano, R. S., and Gupta, A. K., 2017, "Effect of Oxygen Addition in Steam Gasification of Chicken Manure," *Fuel*, 189, pp. 428-435.

Ibrahim, M. S., Alsultan, A., Shen, S., and Amano, R. S., 2015, "Advances in Horizontal Axis Wind Turbine Blade Designs: Introduction of Slots and Tubercle," *Journal of Energy Resources Technology*, 137(5), pp. 051205-051205-6.

Iman, R. L., Helton, J.C., Campbell, J. E., 1981, "An Approach to Sensitivity Analysis of Computer Models, Part 1. Introduction, Input Variable Selection and Preliminary Variable Assessment," *Journal of Quality Technology*, 13 (3), pp. 174–183.

Jackson, R. S., 2016, "Application of Reynolds Stress Model Using Direct Modeling and Actuator Disk Approaches for a Small-Scale Wind Turbine," Ph.D. Dissertation, Mechanical Engineering Department, University of Wisconsin-Milwaukee, Milwaukee, WI.

Jackson, R. S., and Amano, R. S., 2017, "Experimental Study and Simulation of a Small-scale Horizontal-Axis Wind Turbine," *Journal of Energy Resources Technology*, 139(5), pp. 051207-051207-19.

Jaffrézic, B., Breuer, M., 2008, "Application of an Explicit Algebraic Reynolds Stress Model within a Hybrid LES–RANS Method," *Flow, Turbulence and Combustion*, 81(3), pp. 415–448.

Johansen, J., and Sørensen, N. N., 2006, "Aerodynamic Investigation of Winglets on Wind Turbine Blades using CFD," Technical Report No. Risø-R-1543(EN), Risø National Laboratory, Roskilde, Denmark.

Johnson, S. J., van Dam, C. P., and Berg, D. E., 2008, "Active Load Control Techniques for Wind Turbines," Sandia Report No. SAND2008-4809, Sandia National Laboratories, Albuquerque, NM.

Klebanoff, P. S., 1955, "Characterization of Turbulence in a Boundary Layer with Zero Pressure Gradient," Technical report NACA TN-1247, National Bureau of Standards, Washington, DC.

Launder, B. E., Reece, G.J., and Rodi, W., 1975, "Progress in the Development of a Reynolds-stress Turbulence Closure," *J. Fluid Mech.*, 68(3), pp. 537-566.

Leung D. Y. C., Yang Y., 2012, "Wind Energy Development and its Environmental Impact: A review," *Renewable and Sustainable Energy Reviews*, 16(1), pp. 1031–1039.

Lin, J. C., 2002, "Review of Research on Low-profile Vortex Generators to Control Boundary-Layer Separation," *Progress in Aerospace Sciences* 38(4-5), pp. 389–420.

Liu, Y., Waldman, R., and Hu, H., 2015, "An Experimental Investigation on the Unsteady Heat Transfer Process over an Ice Accreting NACA 0012 Airfoil," AIAA Paper No. 2015-0035.

Lynch, F. T., and Khodadoust, A., 2001, "Effects of Ice Accretions on Aircraft Aerodynamics," *Progress in Aerospace Sciences*, 37(8), pp. 669–767.

Malloy, R., 2009, "Aerodynamic Comparison of a Swept Edge and Straight Edge Wind Turbine Blade Through Numerical Simulation," M.Sc. thesis, University of Wisconsin Milwaukee, Milwaukee, WI.

Martin, S., and Bhushan, B., 2014, "Fluid Flow Analysis of a Shark-Inspired Microstructure," *J. Fluid Mech.*, 756, pp. 5-29.

Mathworks, 2017, "MATLAB User Guide," available at <https://www.mathworks.com/help/stats/lhsdesign.html>

Maurya, S. K., Tourani, C., Prabhakar, A., and Kannan, V. K., 2014, "Gas Turbine Combustor Design Optimization for Emission Reduction Using STAR-CCM+," 16th Annual CFD Symposium, Bangalore, India.

McKay, M. D., Beckman, R. J., Conover, W. J., 1979, "A Comparison of Three Methods for Selecting Values of Input Variables in the Analysis of Output from a Computer code," *American Statistical Association*, 21(2), pp. 239–245.

Menter, F. R., 1994, "Two-Equation Eddy-Viscosity Turbulence Models for Engineering Applications," *AIAA Journal*, 32(8), pp. 1598-1605.

Menter, F. R., and Kuntz, M., 2004, "Adaptation of Eddy-Viscosity Turbulence Models to Unsteady Separated Flows Behind Vehicles," *The Aerodynamics of Heavy Vehicles: Trucks, Buses and Trains*, R. McCallen et al., eds., Springer-Verlag, Berlin Heidelberg, pp. 339-352.

Mueller-Vahl, H., Pechlivanoglou, G., Nayeri, C. N., and Paschereit, C. O., 2012, "Vortex Generators for Wind Turbine Blades: A Combined Wind Tunnel and Wind Turbine Parametric Study," ASME paper No. GT2012-69197.

Myers, R. H., 1971, *Response Surface Methodology*, Allyn and Bacon, Inc., Boston, MA.

Nelson, V., 2000, *Wind Energy: Renewable Energy and the Environment*, CRC Press, Boca Raton, FL.

Ngo, L., C., Bello-Ochende, T., and Meyer, J., P., 2015, "Numerical Modelling and Optimisation of Natural Convection Heat Loss Suppression in a Solar Cavity Receiver with Plate Fins," *Renewable Energy* 74, pp. 95 – 105.

Nicoud, F., and Ducros, F., 1999, "Subgrid-scale Modelling Based on the Square of the Velocity Gradient Tensor," *Flow, Turbulence and Combustion*, 62, pp. 183-200.

Noorazyze, S. N., 2014, "Performance Evaluation Of Slotted And Continuous Types Wind Turbine Blade," M.Sc thesis, Universiti Tun Hussein Onn Malaysia.

Osborne, R., 1895, “On the Dynamical Theory of Incompressible Viscous Fluids and the Determination of the Criterion,” *Philosophical Transactions of the Royal Society of London. A*, 186, pp. 123-164.

Øye, S., 1995, “The Effect of Vortex Generators on the Performance of the ELKRAFT 1000 kW Turbine,” *Aerodynamics of Wind Turbines: IEA Joint Action - 9th Symposium*, Stockholm, Sweden.

Pitsch, H., 2006, “Large-Eddy Simulation of Turbulent Combustion,” *Annual Review of Fluid Mechanics*, 38, pp. 453–482.

Pope, S. B., 1975, “A More General Effective Viscosity Hypothesis,” *Journal of Fluid Mechanics*, 72(2), pp. 331-340.

Pope, S. B., 2000, *Turbulent Flows*, Cambridge University Press, Cambridge, UK.

Prince, S. A., Badalamenti, C., and Regas, C., 2017, “The Application of Passive Air Jet Vortex-Generators to Stall Suppression on Wind Turbine Blades,” *Wind Energy*, 20, pp. 109-123.

Red Cedar Technology, 2017, “SHERPA – An Efficient and Robust Optimization/Search Algorithm,” White Paper WP-1023, Rev. 05.08, retrieved 3/1/2017.

Rodi, W., 1976, “A new algebraic relation for calculating the Reynolds stresses,” *Zeitschrift fuer angewandte Mathematik und Mechanik*, 56, pp. T219-T221.

Rodi, W., 1972, “The Prediction of Free Turbulent Boundary Layers by Use of A Two-equation Model for Turbulence,” Ph.D. Dissertation, University of London, London.

Rong, R., Cui, K., Li, Z., and Wu, Z., 2015, “Numerical study of centrifugal fan with slots in blade surface,” *Procedia Engineering*, 126, pp. 588-591.

Rumsey, 2014, “2DN44: 2D NACA 4412 Airfoil Trailing Edge Separation,” last modified March 22, 2016, http://turbmodels.larc.nasa.gov/naca4412sep_val.html.

Rung, T., Lubcke, H., Franke, M., Xue, L., Thiele, F., and Fu, S., 1999, “Assessment of Explicit Algebraic Stress Models in Transonic Flow,” *Engineering Turbulence modeling and Experiments*, W. Rodi, and D. Laurence, eds., Elsevier, Amsterdam, Netherlands, 4, pp. 659-668.

Sarlak Chivae, H., 2014, “Large Eddy Simulation of Turbulent Flows in Wind Energy,” PhD Dissertation, Technical University of Denmark, Lyngby, Denmark.

Schito, P., 2011, “Large Eddy Simulation of Wind Turbines: Interaction with Turbulent Flow,” PhD Thesis, Department of Mechanical Engineering, Politecnico Di Milano, Milan, Italy.

Schramm, M., Stoevesandt, B., and Peinke, J., 2016. "Simulation and Optimization of an Airfoil with Leading Edge Slat" *Journal of Physics: Conference Series*, 753, pp. 022052.

Shepherd, D. G., 1994, "Historical Development of the Windmill," *Wind Turbine technology, fundamental concepts of wind turbine engineering*, D. A. Spera, ed., ASME press, New York, NY.

Shur, M. L., Spalart, P. R., Strelets, M. K., and Travin, A. K., 2008, "A hybrid RANS-LES Approach with Delayed-DES and Wall-modelled LES Capabilities," *International Journal of Heat and Fluid Flow*, 29(6), pp. 1638-1649.

Smagorinsky, J., 1963, "General Circulation Experiments with the Primitive Equations," *Monthly Weather Review*, 91(3), pp. 99–164

Subash, B., Nithyapathi, C., Manikandan, D., and Murali, K. K., 2014, "Aerodynamic Optimization of Wind Turbine Blade by Employment of Slot to Counteract the Effect of Drag," *International Journal of Emerging Technology and Advanced Engineering*, 4(3), pp. 249-253.

Tang, B., 1993, "Orthogonal Array-Based Latin Hypercubes," *Journal of the American Statistical Association*, 88(424), pp. 1392-1397.

Taulbee, D. B., 1992, "An Improved Algebraic Reynolds Stress Model and Corresponding Nonlinear Stress Model," *Physics of Fluids A: Fluid Dynamics*, 4(11), pp. 2555–2561.

Travin, A., Shur, M. L., Strelets, M. K., and Spalart, P. R., 2002, "Physical and Numerical Upgrades in the Detached-Eddy Simulation of Complex Turbulent Flows," *Advances in LES of Complex Flows*, R. Friedrich and W. Rodi, eds., Kluwer Academic Press, pp. 239-254.

Troldborg, N., Zahle, F., and Sørensen, N. N., 2015, "Simulation of a MW Rotor Equipped with Vortex Generators using CFD and an Actuator Shape Model," *AIAA paper No. 2015-1035*.

UpWind Solutions., Inc., 2010, "Case Study: Impact of Vortex Generators on Wind Turbine Performance," available upon request at www.upwindsolutions.com, San Diego, CA.

Uswitch, 2010, "Renewable energy facts- Need-to-know information about renewable energy.," available at <http://www.uswitch.com/solar-panels/guides/renewable-energy-facts/#step3>, retrieved 6/1/2015.

van Dam, C. P., Yen, D.T., and Vijgen, P. M. H. W., 1999, "Gurney Flap Experiments on Airfoil and Wings," *Journal of Aircraft*, 36(2), pp. 484-486.

Velte, C. M., 2009, "Characterization of Vortex Generator Induced Flow," PhD thesis, Department of Mechanical Engineering, Technical University of Denmark, Lyngby, Denmark.

Wadcock, A. J., 1978, "Flying-Hot-Wire Study of Two-Dimensional Turbulent Separation on an NACA 4412 Airfoil at Maximum Lift," Ph.D. thesis, California Institute of Technology, Pasadena, CA.

Wagner, C., Hüttl, T., and Sagaut, P., 2007, Large-Eddy Simulation for Acoustics, Cambridge University Press, Cambridge, UK.

Wallin, S., and Johansson, A. V., 2000, "An Explicit Algebraic Reynolds Stress Model for Incompressible and Compressible Turbulent Flows," J. Fluid Mech., 403(1), pp 89-132.

Wang C., and Sun, M., 2000, "Separation Control on a Thick Airfoil with Multiple Slots Blowing at Small Speeds," Acta Mechanica, 143(3-4), pp. 215-227.

Weber, J. M., 2012, "Passive Flow Control Method for Mitigation of Unsteady Load Excursions on a Wind Turbine Blade," Master's thesis, Texas A&M University, College Station, TX.

Weinmann, M., Sandberg, R. D., Doolan, C., 2014, "Tandem Cylinder Flow and Noise Predictions using a Hybrid RANS/LES Approach," Int. J. Heat Fluid Flow, 50, pp. 263-278.

White, F. M., 2011, Fluid Mechanics, 7th ed., McGraw-Hill, New York.

Whitman, N., Sparks, R., Ali, S., and Ashworth, J., 2006, "Experimental Investigation of Slotted Airfoil Performance with Modified Slot Configurations," Collection of Technical Papers - AIAA Applied Aerodynamics Conference, 3, pp. 1834-1842.

Wikipedia, 2017, "Mandatory Renewable Energy Target," available at http://en.wikipedia.org/wiki/Mandatory_renewable_energy_target, retrieved 4/2/2017.

WindPower Monthly, 2015, "The 10 Biggest Turbines in the World," available at <http://www.windpowermonthly.com/10-biggest-turbines>, retrieved 4/27/2015.

Xie, Z., 2012, "CFD Tutorial of Flow Around an Airfoil," available at http://www.personal.soton.ac.uk/zxie/CFD-SURG/Summer2012_tut/naca0012/Summer2012_tut.pdf retrieved 6/6/2015.

Xie, Y., Chen, J., Qu, H., Xie, G., Zhang, D., and Moshfeghi, M., 2013, "Numerical and Experimental Investigation on the Flow Separation Control of S809 Airfoil with Slot," Mathematical Problems in Engineering, 2013, <http://dx.doi.org/10.1155/2013/301748>.

CURRICULUM VITAE

Saman Beyhaghi

Place of Birth: Tehran, IRAN

EDUCATION

University of Wisconsin-Milwaukee, Milwaukee, WI

Doctor of Philosophy in Mechanical Engineering, May 2017

University of Wisconsin-Milwaukee, Milwaukee, WI

Master of Science in Mechanical Engineering, Aug. 2010

Sharif University of Technology, Tehran, IRAN

Bachelors of Science in Mechanical Engineering, Feb. 2005

EMPLOYMENT HISTORY

University of Wisconsin-Milwaukee, Milwaukee, WI

Instructor / Research Assistant (Sept. 2013 – present)

Teaching Assistant / Research Assistant (Jan. 2008 – May 2011)

Department of Mechanical Engineering

- Developed an experimental setup and a computational model for analysis of flow and heat transfer in a rotating two-pass channel, mimicking internal cooling of gas turbine blades
- Investigated aerodynamic performance of slotted NACA 4412 airfoils and wind turbine blades using wind tunnel experiments and computationally using different turbulence models
- Taught several undergraduate courses, including Thermodynamics, Heat Transfer, Computational Tools for Engineers (MATLAB), and Fluid Mechanics Laboratory
- Studied the evaporation of liquid mixtures from porous wicks by CFD and experiments

Johnson Controls Inc., Milwaukee, WI

HVAC Engineer (July 2011 – Jan. 2015)

- Developed thermodynamic models for thermal analysis and power consumption of chillers, cooling towers, heat exchangers, and pumps used in a central plant optimization project
- Implemented a new method for increasing chiller capacity under reduced lift condition for a central plant optimization project
- Designed various modules along with specification documents for control of commercial Rooftop unit packages using the in-house controller configuration tool
- Successfully led and managed a team of engineers and interns for comprehensive automated testing of control applications in PC simulation and hardware emulation environments

JOURNAL PUBLICATIONS

S. Beyhaghi and R.S. Amano, “Investigation of Flow Over an Airfoil Using a Hybrid Detached Eddy Simulation–Algebraic Stress Turbulence Model”, *Journal of Energy Resources Technology*, 139(5), pp. 051206-051206-9 (2017).

S. Beyhaghi and R.S. Amano, “Improvement of aerodynamic performance of cambered airfoils using leading edge slots”, *Journal of Energy Resources Technology*, 139(5), pp. 051204-051204-8 (2017).

A.K.K. Matt, **S. Beyhaghi**, R.S. Amano, and J. Guo, “Self-Healing of Wind Turbine Blades Using Microscale Vascular Vessels”, *Journal of Energy Resources Technology*, 139(5), pp. 051208-051208-7 (2017).

S. Beyhaghi, Z. Xu, and K.M. Pillai, “Achieving the Inside–Outside Coupling During Network Simulation of Isothermal Drying of a Porous Medium in a Turbulent Flow”, *Transport in Porous Media*, 114(3), pp. 823-842 (2016).

S. Beyhaghi, S. Geoffroy, M. Prat, and K.M. Pillai, “Wicking and evaporation of liquids in porous wicks: A simple analytical approach to optimization of wick design”, *AIChE Journal*, 60(5), pp. 1930-1940 (2014).

M.R. Shaeri, **S. Beyhaghi**, and K.M. Pillai, “On Applying an External-Flow Driven Mass Transfer Boundary Condition to Simulate Drying from a Pore-Network Model”, *International Journal of Heat and Mass Transfer*, 57(1), pp. 331-344 (2013).

M.R. Shaeri, **S. Beyhaghi**, and K.M. Pillai, “Drying of a porous medium with multiple open sides using a pore-network model simulation”, *International Communications in Heat and Mass Transfer*, 39(9), pp. 1320-1324 (2012).

T.G. Hurd, **S. Beyhaghi**, and M. Nosonovsky, “Ecological Aspects of Water Desalination Improving Surface Properties of Reverse Osmosis Membranes”, in: *Green Tribology: Biomimetics, Energy Conservation and Sustainability* (Book editors: M. Nosonovsky & B. Bhushan), pp. 531-564 (2012). (Book chapter)

S. Beyhaghi and K.M. Pillai, “Estimation of Tortuosity and Effective Diffusivity Tensors Using Closure Formulation in a Sintered Polymer Wick During Transport of a Nondilute, Multicomponent Liquid Mixture”, *Special Topics & Reviews in Porous Media: An International Journal*, 2(4), pp. 267-282 (2011).

S. Beyhaghi, K.M. Pillai, D.T. Qadah, and M.L. Dietz, “Evaporation and transport of non-dilute, multi-component liquid mixtures in porous wicks: Simulation and experimental validation”, *International Journal of Heat and Mass Transfer*, 54, pp. 5216-5230 (2011).

CONFERENCE PROCEEDINGS

S. Beyhaghi, P. Dong, M.S. Saravani, M. Morrison, and R.S. Amano, “Computational and Experimental Investigation of Heat Transfer in Stationary and Rotating Internal Cooling Ducts with High Rotation Numbers”, *AIAA P&E Forum*, Atlanta, GA, accepted (2017).

S. Beyhaghi and R.S. Amano, “Leading-edge slots for Improving the aerodynamic performance of cambered airfoils in horizontal axis wind turbine blades”, *ASME Turbo Expo 2017*, Charlotte, NC, accepted (2017).

S. Beyhaghi and R.S. Amano, “Slotted airfoils for increasing the aerodynamic efficiency”, *AIAA Conference Proceedings*, 55th AIAA Aerospace Science Meeting, Grapevine, TX, January 9-13 (2017).

R.S. Amano and **S. Beyhaghi**, “Heat Transfer in a Rotating Two-pass Square Channel Representing Internal Cooling of Gas Turbine Blades”, *AIAA Conference Proceedings*, 54th AIAA Aerospace Science Meeting, San Diego, California, January 4-8 (2016).

S. Beyhaghi and R.S. Amano, “Analysis of Turbulent Flow Around Horizontal Axis Wind Turbines Using Algebraic Stress Model”, *ASME IMECE 2015*, Houston, TX, November 13-19 (2015).

S. Beyhaghi and R.S. Amano, “Use of Algebraic-Stress Model for determination of near-wall Reynolds-Stresses in turbulent flow over a flat plate”, *AIAA Conference Proceedings*, 53rd AIAA Aerospace Science Meeting, Orlando, FL, January 5-9 (2015).

PATENTS

S. Beyhaghi, M. Asmus, and J. Kauffman, “Systems and methods for adaptive capacity constraint management”, Johnson Controls, Inc., published 7/ 2016, Publication number: 20160209852.

H. Noboa, A. Boettcher, and **S. Beyhaghi**, “Fault detection and diagnostic system for a refrigeration circuit”, Johnson Controls, Inc., published 6/ 2016, Publication number: 20160169572.

J.C. Walser, **S. Beyhaghi**, and M. Asmus, “Systems and Methods for Auto-Commissioning and Self Diagnostics”, Johnson Controls, Inc., published 8/ 2015, Publication number: 20150241856.

HONORS AND AWARDS

- UWM Distinguished Dissertation Fellowship Award (2015-2016)
- President of the UWM AIAA (American Institute of Aeronautics and Astronautics) Student Organization (2015-2017)
- UWM Graduate School Travel Award (2012, 2015-2016)
- UWM Chancellor's Graduate Student Award (2010-2011)
- Ranked 148th in Iran's annual nationwide university entrance exam among more than 350,000 participants (2000)